Lithium manganese oxide ($LiMn_2O_4$) spinel surfaces and their interaction with the electrolyte content

by

Brian Ramogayana

DISSERTATION

Submitted in fulfillment of the requirements for the degree of

Master of science

in

Physics

In the

FACULTY OF SCIENCE AND AGRICULTURE

(School of Physical and Mineral Sciences)

at the

UNIVERSITY OF LIMPOPO

Supervisor: Prof. P.E. Ngoepe

Co-Supervisor: Dr. K.P. Maenetja

2021

DECLARATION

I declare that the Lithium manganese oxide ($LiMn_2O_4$) spinel surfaces and their interaction with the electrolyte content hereby submitted to the University of Limpopo, for the degree of Masters of science in Chemistry has not previously submitted by me for a degree at this or any other University; that it is my work in design and in execution, and that all material contained herein has been duly acknowledged.

_____ _____

Ramogayana, B **Date**

DEDICATION

To my mother

Mamareme Julia Ramogayana

ACKNOWLEDGEMENTS

Special thanks go to my supervisor, Prof P.E. Ngoepe, who initiated the project and guided me throughout the project with his great experience and research insight. I would also like to express my gratitude to my mentor and co-supervisor, Dr K.P. Maenetja, who shared her experience and gave me advice on being a researcher.

I wish to appreciate the contributions made by Dr D. Santos-Carballal, Dr P.A. Aparicio, and Dr M.G. Quesne especially on ethylene carbonate adsorption on the major surfaces of lithium manganese oxide $Li_{1-x}Mn_2O_4$ spinel ($0.000 < x < 0.375$) and their continues support even after the visit. Many thanks go to Prof N.H. de Leeuw for hosting me during my visit to Cardiff University in the United Kingdom, Wales, and Dr Q. Parker for endless support during the visit. Great appreciation to the computational facilities of the Advanced Research Computing @ Cardiff (ARCCA) Division, Cardiff University, and Prof N.H. de Leeuw research group for support and motivation. Part of this work was undertaken using the Supercomputing Facilities at Cardiff University operated by ARCCA on behalf of the HPC Wales and Supercomputing Wales (SCW) projects. I also wish to acknowledge the Engineering & Physical Sciences Research Council (EPSRC Grant No. EP/K009567/2 and No. EP/K016288/1), the Economic and Social Research Council (ESRC Grant ES/N013867/1) and National Research Foundation, South Africa, for financial assistance.

I would also like to acknowledge the use of the Centre for High-Performance Computing (CHPC) facility of South Africa in the completion of this work. I also want to appreciate the computational facilities of the Materials Modelling Centre (MMC) and the endless contribution and support of the members of the MMC. Most of all, I acknowledge my supportive family, the Ramogayana and Nkadimeng families. My siblings, Isaac and Kgopotso Manamelane Ramogayana.

ABSTRACT

This dissertation presents the results of the *ab-initio* based computational studies of spinel lithium manganese oxide ($LiMn_2O_4$) bulk, surfaces, and the adsorption of an organic electrolyte, ethylene carbonate. The spinel $LiMn_2O_4$ is one of the most promising cathode materials for Lithium-ion batteries because of its affordability, nontoxicity, and improved safety compared to commercially used $LiCoO_2$. However, it also suffers from the irreversible capacity due to the electrolyte-cathode interactions which lead to manganese (Mn) dissolution. Using the spin-polarized density functional theory calculations with on-site Coulomb interactions and long-range dispersion corrections [DFT+U−D3−(BJ)], we investigated the bulk properties, surface stability and surface reactivity towards the ethylene carbonate (EC) during charge/discharge processes. Firstly, we explored the structural, electronic, and vibrational bulk properties of the spinel $LiMn_2O_4$. It was found that the bulk structure is a stable face-centred cubic structure with a bandgap of 0.041 eV and pseudo-gap at the Fermi level indicating electronic stability. Calculated elastic constants show that the structure is mechanically stable since they obey the mechanical stability criteria. The plotted phonon curves show no imaginary vibrations, indicating vibrational stability. To study the charge/discharge surfaces, we modelled the fully lithiated and the partially delithiated slabs and studied their stability. For the fully lithiated slabs, Li-terminated (001) surface was found to be the most stable facet, which agrees with the reported experimental and theoretical data. However, upon surface delithiation, the surface energies increase, and eventually (111) surface becomes the most stable slab as shown by the reduction of the plane in the particle morphologies. Finally, we explored the surface reactivity towards the ethylene carbonate during charge/discharge processes. The ethylene carbonate adsorption on the fully lithiated and partly delithiated facets turn to enhance the stability of (111) surface. Besides the strong interaction with the (111) surfaces, a negligible charge transfer was calculated, and it was attributed by a large charge rearrangement that takes place within the surfactant upon adsorption. The wavenumbers of the C=O stretching showed a red shifting concerning the isolated EC molecule.

TABLE OF CONTENT

LIST OF FIGURES

LIST OF TABLES

CHAPTER ONE

INTRODUCTION

1.1. BACKGROUND

Over the last few decades, renewable energy storage has become of significant interest in the development of electric vehicles, which could facilitate a lesser reliance on fossil fuels and thus lower the impact on global warming. Although many studies have aimed at discovering or developing sustainable, earth-abundant, and/or low-cost alternative materials [1, 2, 3, 4], there is still no viable replacement for the current lithium-based batteries. However, the development of more efficient and stable cathode materials would offer a major step forwards in the performance of lithium-ion batteries.

Many cathode materials have been studied, including $LiCoO_2$ [5, 6], $Li_3V_2(PO_4)_3$ [7], $LiMn_2O_4$ [8, 9], $Li_4Mn_5O_{12}$ [10], $LiFePO_4$ [11, 12, 13], NCA [14, 15, 16] and NMCs [17] in order to improve the electrochemical performance of lithium-ion batteries. Among these materials, lithium manganese oxide ($LiMn_2O_4$) spinel has attracted the most attention as a potential cathode material because of its three-dimensional crystal structure that allows a reversible diffusion of Li^+ ions [18, 19]. Moreover, $LiMn_2O_4$ is considered a safer substitute for the currently commercialized $LiCoO_2$ owing to its low environmental impact, the abundance of manganese, and its high energy density [20].

However, the use of $LiMn_2O_4$ spinel as a cathode material is limited by the irreversible facing of the capacity, which is attributed to the dissolution of manganese, electrolyte oxidation at high voltages, and the Jahn-Teller distortion of the octahedral Mn^{3+} atoms [21, 22]. While the formation of distorted $Li_2Mn_2O_4$ and electrolyte oxidation can be reduced by cycling in a restricted voltage window, other effective solutions for solutions are still needed to mitigate the Mn dissolution [23].

Several methods have attempted to mitigate the manganese dissolution, including (i) cation doping [24, 25]; (ii) the replacement of commercially used $LiPF_6$ as the electrolyte ionic conductor to limit the production of the scavenging hydrofluoric acid produced by its

degradation [26, 27, 28]; and (iii) surface coating to create an artificial barrier that limits the direct electrode-electrolyte contact [29, 30, 31, 32]. However, there is currently no substitute ionic conductor for the electrolyte which has better conductivity, thermal stability, and affordability than $LiPF_6$, whereas the alternative route of introducing dopant ions might change the spinel crystal structure, thereby affecting the Li^+ transport in the battery [33].

Another solution implemented is the addition of solvent to the electrolyte content to improve the mobility of Li^+ ions. An effective electrolyte solvent will not only be a good solvent for the ionic conductor but will also improve the lifetime of $LiMn_2O_4$-based lithium-ion batteries. Guyomard *et al.* [34] demonstrated that alkyl carbonates, such as propylene carbonate (PC) [35], vinylene carbonate (VC) [36, 37], allyl ethyl carbonate (AEC) [38] and ethylene carbonate (EC), are some of the most stable solvents for the lithium-ion battery electrolytes. Numerous subsequent studies [39, 40, 41] have shown that ethylene carbonate (EC) is the most stable electrolyte solvent and shows improved electrochemical performance. Compared to other commercially used electrolyte solvents, EC has the largest dielectric constant ($\varepsilon \approx 90.5$) [42, 43] and melting point owing to its high molecular symmetry.

In this work, we report on calculations based on the density functional theory to study the bulk, surface stability, and the adsorption of the ethylene carbonate onto the clean non-polar surfaces of the fully lithiated and partially delithiated spinel $Li_{1-x}Mn_2O_4$ material ($0.000 < x < 0.375$).

1.1.1. Structural aspect

The spinel crystal structure is named after the mineral $MgAl_2O_4$. The structure is identified by the chemical formula AB_2O_4, where *A* and *B* are the metallic cations. The spinel $LiMn_2O_4$ has a face-centered cubic crystal structure with a space group $Fd\bar{3}m$ (No. 227) [44] and a lattice constant of $a = 8.247$ Å [45, 46]. As shown in Figure 1, the structure consists of a cubic close-packed array of oxygen atoms occupying the 32*e* sites, where lithium and manganese atoms occupy one-eighth of the tetrahedral (8*a*) sites and one-half of the octahedral (16*d*) sites, respectively, [47]. The 8*a* and 16*d* form a three-

dimensional pathway for lithium-ions diffusion. When Li-ions diffuse into the structure, first moves from 8*a* site to the neighbouring 16*d* site, and then to the next 8*a* site in a way that it enables three-dimensional lithium diffusion. The Mn ions have octahedral coordination to the oxygen's, and the MnO_6 octahedra share edges in a three-dimensional host for the Li guest ions.

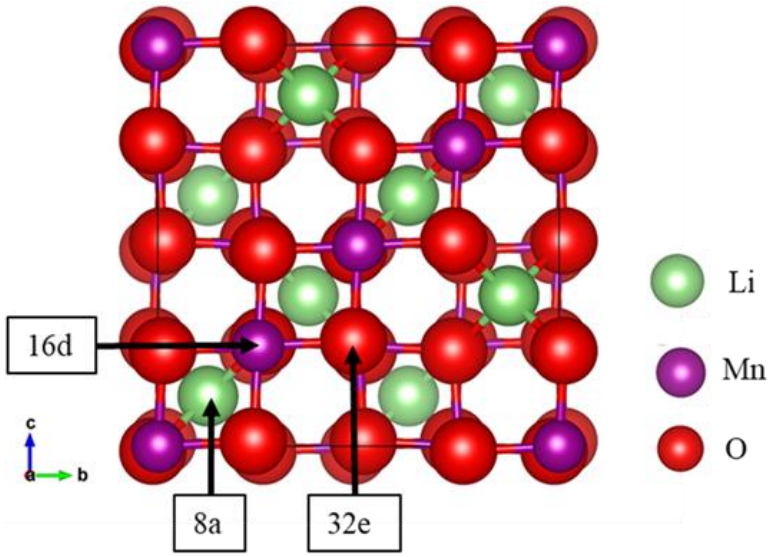

Figure 1: Schematic diagram of the conventional unit cell of $LiMn_2O_4$, showing the 8*a* tetrahedral, 16*d* octahedral, and 32*e* sites.

Upon delithiation, the Li^+ ions move out of the cathode material to the anode through the electrolyte. A full delithiation of the $LiMn_2O_4$ leads to a transformation to the MnO_2 cubic structure, while full lithiation leads to a $Li_2Mn_2O_4$ tetragonal structure. Table 1 below indicates the atoms found in the spinel $LiMn_2O_4$ conventional unit cell. The positions indicated in column 2, specify the number of atoms of the same type contained in the unit cell at their respective positions (Wyckoff sites).

Table I. Fractional coordination of spinel $LiMn_2O_4$

Elements	Sites	X	Y	Z
Li	8*a*	0.125	0.125	0.125
Mn	16*d*	0.500	0.500	0.500
O	32*e*	0.259	0.259	0.259

1.1.2. Brief description of Lithium-ion batteries

Batteries are well known as devices that convert their chemical potential contained in their active materials into electric energy through an electrochemical redox reaction. In their daily application, batteries are made up of two or more cells connected in parallel or series depending on the output voltage desired. However, all cells have three major components, namely, a negative electrode (anode), a positive electrode (cathode), and the separating ionic conductor (electrolyte) for the transfer of charge. Lithium-ion batteries are one of the most used storage devices due to their high voltage, high energy density, and durable cycle charge. Like other rechargeable batteries, lithium-ion batteries use a positive electrode (cathode) and a negative electrode (anode), separated by a medium called an electrolyte (see Figure 2). The positive electrode is usually made of lithium cobalt oxide ($LiCoO_2$), but in our work, we focus on the positive electrode being lithium manganese oxide ($LiMn_2O_4$). The negative electrode is usually made of carbon (graphite), in other studies, several effective alternative anode materials are used [48, 49]. During the charging process, the lithium ions move from the positive to the negative electrode, also referred to as the delithiation process. While during the discharged process, lithium ions travel from the negative to the positive electrode, and the process is also referred to as the lithiation process.

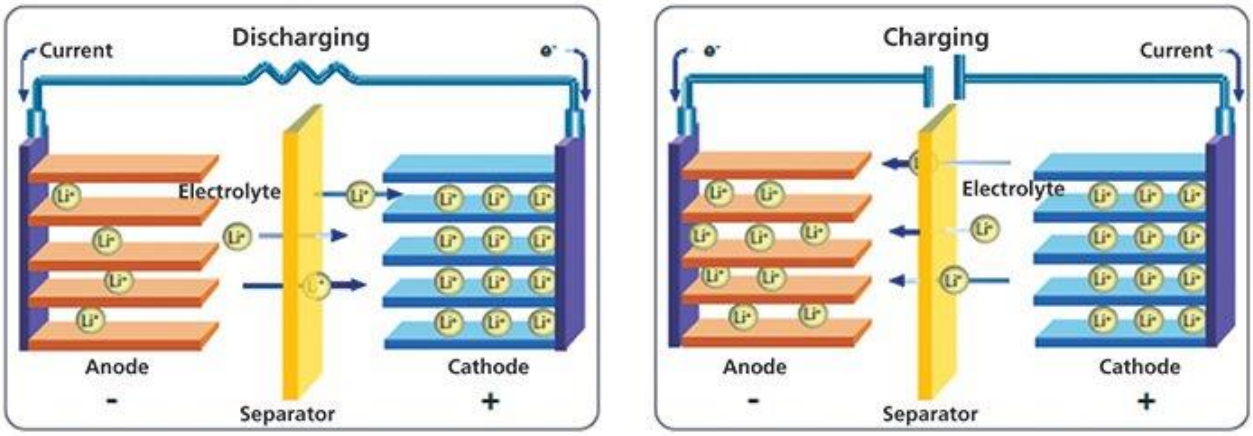

Figure 2: Movement of Li ions during charge and discharge process in the lithium-ion battery *[50]*.

1.1.3. Applications

Lithium-ion batteries are widely used in cell phones, laptops, electric cigarettes, and other portable devices (see Figure 3). Due to recent modifications, lithium-ion batteries can power the hybrid electric vehicles (HEV) and can be applied in energy storage systems.

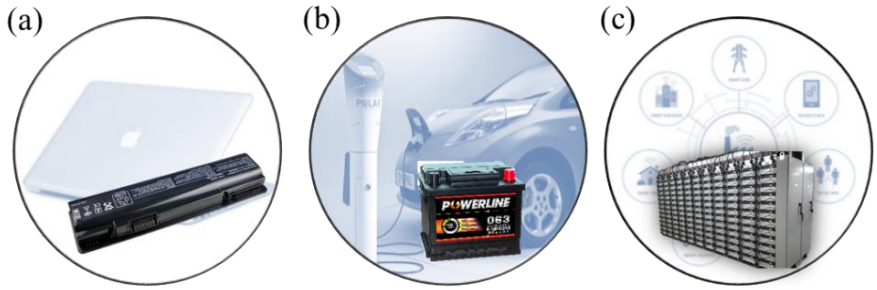

Figure 3: Examples of Lithium-ion batteries applications, which (a) electric vehicles, (b) portable devices, and (c) storage facilities (smart grids).

Since the discovery of lithium-cobalt-oxide battery by J.B Goodenough (1922), lithium-ion batteries became efficient energy storage devices due to their high energy density, self-discharge ability, long life cycle, and their environmental friendliness. Recently, various types of materials were used as electrodes to better the intercalation processes of the battery (see Figure 4) [51]. Among all the material used and researched, the $LiMn_2O_4$ spinel is the most effective practical based cathode electrode. $LiMn_2O_4$ also reveal features such as low cost, wide abundance of manganese, environmental friendliness, high working potential, and excellent safety characteristics.

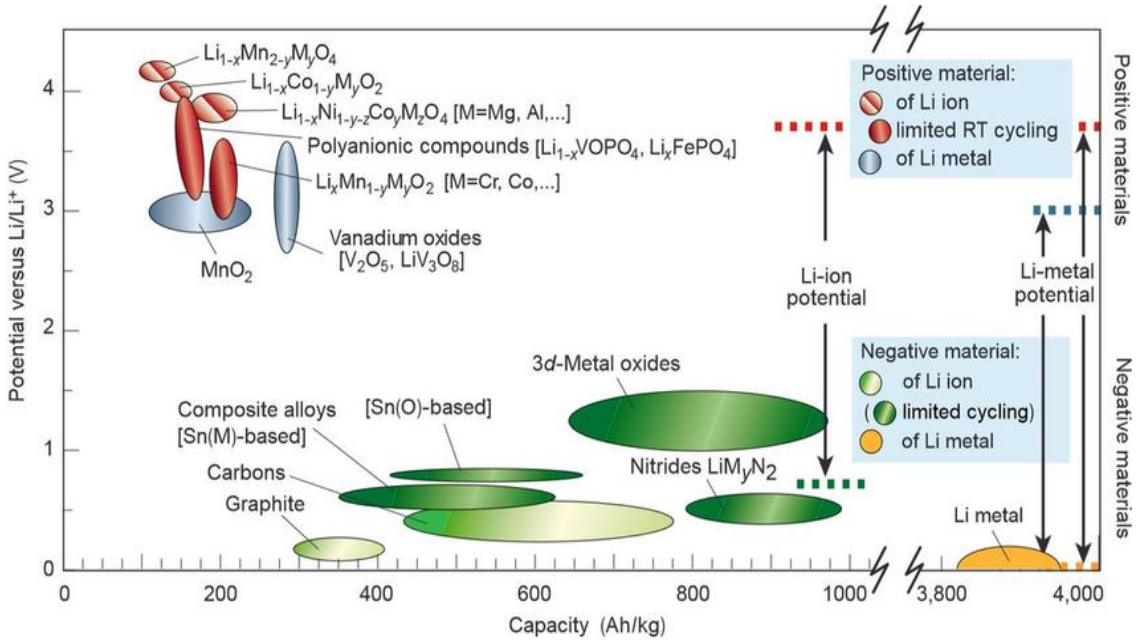

Figure 4: Different electrode materials used in a lithium-ion battery and their capacities *[51]*.

1.2. LITERATURE REVIEW

The first attempt of lithium-ion batteries was in the 1970s, when an English scientist, Stanley Whittingham, working for the Exxon mobile started exploring the idea of developing a new battery. He tried using titanium disulfide and lithium metal as electrodes, but this combination posed some serious complication, such as safety (the battery experienced a short-circuit and caught fire). Later in the 1980s, John B. Goodenough, who is an engineering professor at the University of Texas started working on his new idea. He experimented using titanium disulfide and lithium cobalt oxide, and the battery paid off. In 1983, Thackeray *et al.* [52] identified manganese spinel as a cathode material. This Mn spinel primary cells are produced for use in day-to-day consumer applications and their were also cosidered for secondary applications such as stationary storage systems and electric vehicles. These cells are noted for their high specific energy (260 Wh/kg), flat discharge curves, wide operating temperature range (-40°C to +60°C) and long shelf life (up to 10 years) [53].

In the spinel $LiMn_2O_4$, the edge-shared octahedral Mn_2O_4 host structure is highly stable and possesses a series of intersecting tunnels formed by the face-sharing of tetrahedral lithium (8a) sites and empty octahedral (16c) sites. This tunnels allows the three-dimensional lithium diffusion. The lithium diffusion into/from the tetrahedral 8a sites occur at about 4V while the cubic structural symmentry is maintained. Moreover, lithium intercalation into this spinel structure can reach maximum composition of $Li_2Mn_2O_4$, occuring at about 3V. However, upon reaching this $Li_2Mn_2O_4$ composition, the structure undergo phase transition from cubic to tetragonal phase [54]. An intense study was undertaken and established temperature intervals of T=780 - 915 ºC (called elevated temperatures) which result in surface reations, leading to the spinel disproportionation and the formation of a tetragonal spinel phase and Li_2MnO_3 [55].

At this elevated temperature, various studies reported that the electrolyte salt $LiPF_6$ undergoes oxidative decomposition [56]. It degrades to form LiF and PF_5 through the reaction:

$$LiPF_6 \longrightarrow LiF + PF_5 \qquad (1.1)$$

Furthermore, the PF_5 react with water molecules present in the battery to form the scavenging hydrofluoric acid (HF) and POF_3, and its reaction can be represented as:

$$PF_5 + H_2O \rightarrow 2HF + POF_3 \quad (1.2)$$

The Mn^{4+} on the surface gains electrons produced by the oxidative decomposition of $LiPF_6$–based electrolyte and undergo a reduction to form Mn^{3+}. The resulting Mn^{3+} ions undergo a disproportionation reaction. Hunter *et al.* [57] outlined Mn^{3+} dispropotionation reaction as:

$$2Mn^{3+}_{(solid)} \rightarrow Mn^{4+}_{(solid)} + Mn^{2+}_{(solution)} \quad (1.3)$$

The resulting Mn^{2+} ions dissolve into the electrolyte, and the dissolved Mn^{2+} is then transported to the anode. This further causes a considerable capacity fading since the dissolved manganese will interact with the lithium content in the anode by oxidizing the Li from the anode. This results in manganese dissolution, the formation of Jahn-Teller distorted $Li_2Mn_2O_4$, and electrolyte oxidation.

1.2.1. Strategies implemented to reduce Mn dissolution

In the study of improving the electrochemical performance and controlling Jahn-Teller distortion, electrolyte oxidation, and Mn dissolution, studies indicated that the formation of distorted $Li_2Mn_2O_4$ and electrolyte oxidation can be reduced by cycling in a restricted voltage window, however, effective solutions are still needed to mitigate the Mn dissolution [58, 59, 60]. Several strategies used to reduce this Mn^{2+} dissolution into the electrolyte, which includes cation doping [24, 25], the replacement of commercially used $LiPF_6$ [26, 27, 28], and surface coating to create an artificial barrier that limits the direct electrode-electrolyte contact [29, 30, 31, 61].

1.2.1.1. Surface coating

Surface coating is the deposition of an additional layer of material that will improve the material's critical properties and create a protective barrier against deterioration of the surface due to external reactions with the surrounding environment. On the spinel $LiMn_2O_4$, it limits the cathode-electrolyte interaction and reduces the manganese

dissolution. Many studies focused on different coating materials which include fluorides (such as AlF_3 [62], SrF_2 [63] and LaF_3 [64]), phosphates [65, 66, 67], and other oxides such as ZnO [68, 69, 70], ZrO_2 [71], MgO [72, 73].

Although various coating materials showed improved electrochemical performance and reasonably better capacity retention, oxides and fluorides attracted the most attention because of their reactivity toward the electrolyte components and their ability to form an additional coating layer [74, 75]. The chemisorption taking place on metal oxides surfaces is of great relevance since they provide the strongest connection between the heterogeneous and homogeneous catalysis [76, 77]. Different oxides were explored which include the Al_2O_3 [78, 79, 80, 29], ZrO_2 [73, 71, 81], MgO [82, 83], ZnO [68, 69, 84, 85], *etc*. Among all the oxides, aluminium oxide (α-Al_2O_3) attracted the most attention as a potential cathode material for Li-ion batteries because of its electric behaviour and catalytic activity. It is also considered for use in catalysis, corrosion sciences, ceramic processing, and electrochemistry [86, 87, 88, 89].

The electronic and surface termination of the α-Al_2O_3 (0001) facet attracted the most interest in both theoretical and experimental studies [90, 91, 92, 93]. Toofan and Watson [94] studied the surface termination of the (0001) facet using the LEED crystallographic determination and reported that the Al- and O-terminated domains are in agreement with the reported experimental work. Anh and Rabalais [92] studied the composition and structure of the Al_2O_3 {0001}-(1x1) surface using time-of-scattering, atomic force spectroscopy (AFM) and ion trajectory simulations, and reported that the Al-terminated surface is the most stable. Several computational studies [95, 96] also confirmed that the Al-terminated (0001) surface is the most stable facet.

Many studies focused on the surface adsorption of various molecules which includes, H_2O [97, 98], HCl [99, 100, 101], CO_2 [102] and methanol [103] for different applications. However, α-Al_2O_3 has the ability to scavenge the highly corrosive hydrofluoric acid (HF) continuously produced by the degradation of the commonly used $LiPF_6$-based electrolyte [104], influenced its applications as a coating material for Li-ion batteries. Kannan *et al.* [105] and Eftekhari [106], initially reported that the Al_2O_3 as a coating material can

significantly improve the electrochemical performance of uncoated $LiMn_2O_4$ spinel at elevated temperatures.

Numerous subsequent studies indicated that the use of Al_2O_3 as a coating material improve the electrochemical performance of the Li-ion batteries since it limits the formation of Jahn-Teller distorted $Li_2Mn_2O_4$ in $LiMn_2O_4$-based lithium-ion batteries [107, 108], and the transition metal dissolution [57]. Myung *et al.* [74] demonstrated that the HF reacts with the Al_2O_3 surface and produce AlF_3 which intern acts as an additional coating material, though reaction:

$$Al_2O_3 + 6HF \rightarrow 2AlF_3 + 3H_2O \quad (1.4)$$

Quan *et al.* [75] studied the HF adsorption on α-Al_2O_3 (0001) surface and indicated that upon adsorption, the HF dissociates to for an Al-F bond which is due to the strong electronegativity of F. Meanwhile, the hydrogen covalently bond with the neighbouring oxygen atom to form H-O bond. A similar reaction was observed by Kondati *et al.* [109] on the θ-Al_2O_3 surface.

1.2.1.2. Commercially used electrolyte and the addition of organic solvents.

The main cause of manganese dissolution is the highly corrosive hydrofluoric acid (HF) continuous produced by the degradation of common $LiPF_6$-based electrolytes (as shown in equation 1.1 and 1.2). One approach to limit the production of HF would be the replacement of $LiPF_6$-based electrolytes [110, 111, 112, 113]. However, there is currently no replacement which can provide better conductivity, thermal stability, toxicity, corrosiveness, and less costly compared to the commonly used $LiPF_6$ [114]. Therefore, a great effort has been paid to optimize the commonly used electrolyte component by developing functional additive that will stabilize the $LiPF_6$ salt [115, 116, 117], elimination of HF and H_2O [118, 119, 120] and modification of solid electrolyte interface (SEI) layer [121, 122, 123].

About 27 years ago, Guyomard *et al.* [124] demonstrated that alkyl carbonates are the most stable solvents for use in Li-ion batteries. Numerous subsequent studies [125, 126, 41] have shown that among all the alkyl carbonates, ethylene carbonate (EC) is the most

stable electrolyte solvent and shows improved electrochemical performance. Many other electrolyte solvents such a propylene carbonate (PC) [127], vinylene carbonate (VC) [128, 129], allyl ethyl carbonate (AEC) [130], *etc*. were also investigated. Compared to other commercially used electrolyte solvents, EC has a higher dielectric constant ($\boldsymbol{\varepsilon} \approx 90.5$) [131, 132] and also has a high melting point which arises due to its molecular symmetry [133]. Fong *et al.* [134] reported that the EC containing electrolyte tend to form a protective film, solid electrolyte interface (SEI), on the electrodes that prevented further electrolyte decomposition on the anode.

Most of the work on the EC focused on the decomposition of EC on to the $Li_xMn_2O_4$ spinel surfaces [133, 135, 136]. The first step of EC decomposition mechanisms was found to be a two-step process. The first step is the rate-determining step, wherein a proton is abstracted from the EC molecule, then transferred to the surface. The second step involves the EC ring opening. Østergaard *et al.* [137] further studied the electrolyte oxidation of EC on Li_xMnO_2, Li_xCoO_2, and Li_xNiO_2, and they found that the oxidation of the $LixMO_2$ $(10\bar{1}4)$ surface follow the same trend, while the reactivity of the metal does not. Leggesse *et al.* [138] studied the ethylene carbonate (EC) adsorption and decomposition reaction mechanism onto the (100) discharged $LiMn_2O_4$ and 40% charged $Li_{0.6}Mn_2O_4$. They found that the bidentate binding is more favoured on the charged $Li_{0.6}Mn_2O_4$ while monodentate binding of carbonyl oxygen is more preferred on the discharged $LiMn_2O_4$. EC surface interactions on the other low Miller index surfaces still need to be addressed.

1.2.2. Magnetic properties of spinel $LiMn_2O_4$.

Various studies [139, 140, 141, 142, 79, 143] focused on the magnetic properties of the $LiMn_2O_4$ spinel, which offered insight on different arrangements of the magnetic moments of the Mn atom. Even though the magnetic moments of the spinel originates from the unpaired electrons of the manganese atom, the total magnetism is given by the ground state configuration of the atoms under specific conditions. Many experimental and computational studies described the short and long-range magnetic ordering and suggested that the ferromagnetic ordering is lower in energy compared to the antiferromagnetic ordering with 24 meV $f.u.^{-1}$ [144]. similar calculations were performed and reported that the antiferromagnetic configuration of Mn chains along the [011]

direction is more stable than the antiferromagnetic ordering of Mn atoms along the [001] direction with alternating magnetic moments with the cations from the neighboring planes [145]. A subsequent first principle studies [146, 79] focused on the ferromagnetic cubic cell and the antiferromagnetic orthorhombic cell, they correctly predicted the number of features low Miller index surfaces without considering their different magnetic ordering.

1.2.3. Low Miller index surface

Understanding the surface chemistry of the $LiMn_2O_4$ spinel is more important for improving the electrochemical performance of the battery. The low Miller index surfaces, mainly the (001), (011), and (111) were intensively studied in both experimental and computational studies [147, 148, 146, 149, 150]. Most study focused on discussing the low Miller index surfaces. Surfaces were constructed using the Tasker [151] dipole method, which stated that surfaces of any ionic or partly ionic crystal can be classed into one of the three classes, type 1 (T1), the neutral surface with the stoichiometric proportion of anions and cations in each plane, type 2 (T2), the charged surface that has no dipole moment in the repeating unit perpendicular to the surface, and type 3 (T3), the charged surface that has a dipole moment in the repeating unit perpendicular to the surface. Type 1 and 2 surfaces may resemble the sample termination of the bulk, but type 2 plane is determined by stacking sequence, while type 3 must undergo reconstruction. However, with $LiMn_2O_4$ spinel surfaces, the (001), (011) and (111) slabs undergoes reconstruction to eliminate the dipole perpendicular to the surface.

The stacking sequence of the (001), (011), and (111) facet of the $LiMn_2O_4$ spinel surfaces have been widely studied in the literature. The (001) surface terminations were cleaved from atomic planes perpendicular to the [001] direction and consist of two alternating planes. The alternating planes are Li and Mn/O terminations, and its sequence was summarised as:

$$½ (Mn_4O_8); Li_2; Mn_4O_8; \ldots; ½ (Mn_4O_8) \quad (1.5)$$

The (011) surface can be cleaved along the Li/Mn/O and Mn/O planes, and its stacking sequence is summarised as:

$$½ (MnO_2); LiMnO_2; \ldots; ½ (MnO_2) \quad (1.6)$$

The (111) facets were created from atomic planes consisting of six possible bulk-like surface terminations (O_1, Mn_1, O_2, Li_1, Mn_2, and Li_2) which are dipolar.

$$\text{½ Mn; Li; } O_4\text{; } Mn_3\text{; } O_4\text{; Li; Mn, Li; …; } O_4\text{; } Mn_3\text{; } O_4\text{; Li; ½ Mn} \quad (1.7)$$

However, upon reconstruction, only two non-dipolar terminations were possible for the (111), i.e. Li, and Li/Mn/O terminations. Benedek *et al*. [152] reported that the facet with the lowest energy is the Li-terminated (001) surface. The lowest surface energy of the Li-terminated (001) agrees with the low energy Mg-terminated (001) of the $MgAl_2O_4$ spinel [153]. Subsequent studies [149, 79, 148] confirmed that the Li-terminated (001) surface is the most stable facet with energy ranging between the 0.26 and 0.96 J/m^2. Despite all the computational calculations carried out with DFT using different GGA+U functional, the surface energies remain in the same range. Karim *et al.* [148] also investigated the equilibrium particle shape for the $LiMn_2O_4$ spinel through the Wulff construction using the calculated surface energies for GGA and GGA + U calculations. The (111) facet was the most stable, followed by the (100) surface resulting in Cubo octahedral particle shape. The results were in agreement with the reported experimental studies [154, 155], where the spinel particle was found to exhibit the same Cubo octahedral morphology with predominant (111) surface. The surface energies of (111) and (001) facets were very close and their difference is mainly due to experimental conditions [149]. However, the proposition has been made that nanoparticles dominated by (111) surface are more resistant to Mn^{3+} disproportionation [156]; this suggests that the (111) LMO surface is more resistant to Mn dissolution.

1.2.4. Other studies on $LiMn_2O_4$

Most recently, Nkosi *et al.* [157] reported the use microwave irradiation at pre- and post-annealing steps of $LiMn_2O_4$ synthesis. They indicated that the microwave irradiation can be used to shrink the spinel particles and lattice parameters for improved structural crystallinity and tune the Mn^{3+}/Mn^{4+} ratio to obtain $n_{Mn} \approx 3.5+$ for enhanced electrochemical performance. Similar work was performed using the microwave-assisted solid-state reaction for the synthesis of nickel doped $LiMn_2O_4$ [158]. It was demonstrated

that microwave irradiation could enhance the exposure of the (111) facets and tune the Mn^{3+} concentrations thereby promoting structural stability and cycling performance.

Santos-Caballal et al [143] recently studied the simulated the bulk of $LiMn_2O_4$ using the primitive rhombohedral unit cell containing 14 atoms. Given the size of their supercell, they could model three inversion degrees, i.e. the normal, half-inverse and fully inverse spinels. The authors compared the predicted configurational energy using the 1x1x1 primitive unit cell with the ensemble average calculated for the 25% inversion degree in the 2x1x1 supercell and found them to be in good agreement.

Many experimental studies have revealed that the intercalation voltage of the spinel $LiMn_2O_4$ can be increased through substituting the other transition metal ion for Mn sites [159, 160, 161]. Shi et al. [162] studied the effect of cation doping on the electronic spinel $LiM_yMn_{2-y}O_4$ (M=Cr, Mn, Fe, Co and Ni) using first principle calculations. A new O-2*p* band was observed in the lower energy position with the appearance of M-3*d* due to the interaction between M-3d and O-2*p*, which will bring about a higher intercalation voltage, since more energy will be needed to remove electrons from the lower O-2*p* level. Various subsequent studies explored the effect of cation doping with Al [163, 164, 165], Co [166, 167, 168], Nb [169, 170], Ni [171, 172, 173], etc.

In the need for high energy density and improvement of $LiMn_2O_4$ cathode, cation doping did not only shown an improvement of spinel material, it paved a way to the discovery of Li-Mn-Ni-Co-O (NMCs) based high energy density batteries. Various studies explored the energy density, stability, and their electrochemoical performance [174, 175, 176]. Recently, sumsang discovered a 50% improved all solid-state Li-ion battery interms of energy density, while achieving 200% battery lifecycle [177]. The battery is composed of layers of Nikel-Cobalt-Manganese-Oxide as a cathode material and also stainless steel, silver-carbon layer, and aluminium collector to also reduce the Li dendrites and low coulomb efficiency. This new development of solid-state Li-ion battery with imbedded Ni-Mn-Co cathode material is impacable, but the manufacturing of this battery is still expansive due to the cost and hich demand of Ni and Co materials.

1.3. INTENTIONS OF THE STUDY

The use of portable devices such as cell phones, laptops, e-cigarettes, etc. for entertainment, communication, data processing, etc. is rapidly increasing. Currently, the use of electrically powered vehicles is becoming more and more realistic. To nurture this increasing energy demand, several studies worked on developing efficient, environmentally friendly, low cost, and rechargeable energy storage devices [1, 2, 3, 4]. Rechargeable lithium-ion batteries appeared as one of the most successful solutions in the development of alternative energy devices. The spinel $LiMn_2O_4$ is one of the most promising cathode materials for Lithium-ion batteries because of its affordability, nontoxicity, and improved safety compared to commercially used $LiCoO_2$. However, it suffers from capacity fading due to the cathode-electrolyte interactions.

Hence in this dissertation, we study the bulk, surface stability, and the adsorption of the ethylene carbonate onto the clean non-polar surfaces of the fully lithiated and partially delithiated spinel $Li_{1-x}Mn_2O_4$ material ($0.000 < x < 0.375$). We employ the spin-polarized density functional theory calculations with on-site Coulomb interactions and long-range dispersion corrections [DFT+U−D3−(BJ)] as implemented in the VASP code. The main purpose of the work is to investigate the stability of the bulk structure, the effect of delithiation on surface stability and the reactivity of commercially used organic electrolyte, ethylene carbonate (EC) during charge/discharge processes of the battery.

Four properties will be determined to investigate the stability of spinel bulk structure, namely, structural, electronic, mechanical, and vibrational properties. In the structural properties, the equilibrium lattice parameters and the heats of formation will be calculated. For electronic properties, the density of states (DOS) and band structures were calculated and plotted to describe the electronic stability and the electronic arrangement. The mechanical stability was discussed by calculating the elastic constants, moduli, anisotropy, and Pugh's ratio at the strain of 0.005. Furthermore, the vibrational properties were discussed by calculating and plotting the phonon dispersion and the partial phonon density of states (PPDOS).

From the fully optimized $LiMn_2O_4$ spinel bulk structure, we will construct the three low Miller index surfaces which are the (001), (011), (111) surfaces using METADISE code. The stability of the three low Miller index surfaces will be obtained by calculating their unrelaxed and relaxed surface energies. To mimic the charge/discharge surfaces, we will model the partially delithiated surfaces from the fully relaxed low Miller index surfaces by removing Li atoms from the uppermost atomic layers of the surfaces, and their stabilities will be studied by calculating their respective surface free energies.

To study the reactivity of the organic electrolyte component, ethylene carbonate (EC), we will allow the molecule to interact with the surfaces when placed parallel and perpendicular through the Mn, Li, and both. The morphologies will be constructed for clean fully lithiated, adsorbed fully lithiated, clean partially delithiated, and the adsorbed partially delithiated surfaces. The reactivity of the EC molecule was further discussed by the Bader charge analysis and the vibrational frequencies. For validation, the vibrational frequencies will be compared with available experimental data at the National Institute of Advanced Industrial Science and Technology (AIST) [178].

1.4. OBJECTIVES

The objectives of the study are to:

- investigate the stability of the $LiMn_2O_4$ spinel bulk structure by determining the structural properties and the mechanical properties,
- generate the $LiMn_2O_4$ spinel surfaces using METADISE program and calculate their surface energies,
- evaluate the effect of delithiation on the surface stability by calculating the surface free energies and constructing particle morphologies,
- evaluate the surface adsorption sites and the binding energies with the electrolyte content ethylene carbonate (EC),
- investigate the effect of adsorption during charge/discharge processes by calculated the surface free energies and particle morphology.

- furthermore, we investigate the surface reactivity towards the EC-based electrolyte by calculating the Bader charges and vibrational frequencies and compare them with available experimental data.

1.5. OUTLINE OF THE DISSERTATION

This dissertation reports on the spinel bulk structure, stability of the charge/discharged surfaces, and their interactions with the organic electrolyte component, ethylene carbonate (EC).

The dissertation is partitioned into five chapters:

Chapter one discusses the background, historical overview, and the problems encountered when using the $LiMn_2O_4$ spinel as a cathode material. We review the literature and the spinel crystal structure. Finally, indicate the objectives and intentions of the study.

Chapter two describe the method used in the current study. We discuss the DFT, plane-wave pseudopotential method, and Vienna *ab-initio* Simulation Package (VASP) code. We firstly introduce the DFT and indicate the background, other first principle studies. Secondly, we discuss the approximation methods such as local density approximation (LDA), general gradient approximation (GGA). Then discuss the pseudopotential methods and VASP. Lastly the discussion of the properties studies such as heats of formation, the density of states, phonon dispersions, elasticity, surface energies, adsorption energies, vibrational frequencies, Bader charges, and Wulff crystal morphologies.

Chapter three discusses the stability of the $LiMn_2O_4$ spinel bulk structure. Firstly, we discuss the cut-off and *k*-points of the bulk structure. Secondly, discuss the lattice parameters, heats of formation, band structures, the density of states, elasticity, and the phonon dispersions.

Chapter four investigates the surface chemistry and reactivity of EC onto the facets. We focus on the surface construction and stacking sequence of the three low Miller index

surfaces, which are (001), (011), and (111) surfaces. We discuss the surface energies of the fully lithiated and the surface free energies for the partially delithiated surfaces and the adsorbed surfaces. We then discuss the most preferred adsorption sites, positions, and adsorption energies. Furthermore, we discuss the effect of adsorption on the fully lithiated, and partially delithiated surfaces. Lastly, we study the EC-surface interactions based on the Wulff crystal morphologies before and after adsorption, charge transfers, work functions, and vibrational frequencies.

Chapter five fully conclude and give a few recommendations. We summarise our findings of this study and give some recommendations.

CHAPTER 2

2.1. METHODOLOGY

Density functional theory (DFT) methods are widely used to compute the ground state of condensed matter systems. It has become one of the most accurate and successful methods mainly because of the functionals, such as LDA and GGA, which gives reasonably accurate results. In this chapter, we present an overview of the *ab-initio* methods and models used for this computational study. A full description of the fundamental concept of the first principle quantum chemistry methods and the analysis of the properties investigated are also covered. The theory has many applications in solid states physics, chemistry, biology, geology, material science, and many more fields.

2.1.1. The ab-initio method

Ab-initio methods are first principle computational techniques which are based on quantum chemistry. The models in *ab-initio* are mathematically modelled based on the Schrödinger's equation. These methods do not use any experimental data or any other parameters in obtaining the results about the molecular systems. They are widely considered as the most accurate, efficient, as well as the most difficult techniques used in the field of molecular modelling [179]. *Ab-initio* is more effective mainly because it starts from scratch. Starting from only the molecular structure and some constants, one can investigate numerous chemical properties, the reactivity of the molecule under external conditions, and observe the electronic arrangements of the molecular orbitals. This generally means that the integral in the Schrödinger's equation for the system is explicitly solved without the use of empirical parameters.

The initial point of the *ab-initio* method optimized nuclear configuration, could be obtained using the molecular mechanics method. However, there are some limitations encountered in this method, which include the limited size of the molecule. When coming to molecules with thousands of atoms, such as proteins and other biological molecules, this method can't be considered. The easiest type of *ab-initio* electronic calculation is the Hartree-Fork (HF) scheme, wherein the instantaneous Coulombic electron-electron repulsion is not

considered. Only the average effect (mean-field) is included in the calculation. The first assumption is the Born-Oppenheimer approximation, which reduces the Schrödinger equation for a molecular system to a single electronic motion for a nuclear configuration. The Hamiltonian with the Born-Oppenheimer approximation for a molecule is given by:

$$\widehat{H} = -\frac{1}{2}\sum_{a}^{electrons} \nabla^2{}_a - \sum_{A}^{nuclei}\sum_{a}^{electrons}\frac{Z_A}{r_{Aa}} + \sum_{A>B}^{nuclei}\sum_{B}^{nuclei}\frac{Z_A Z_B}{R_{AB}} + \sum_{a>b}^{electrons}\sum_{b}^{electrons}\frac{1}{r_{ab}} \quad (2.1)$$

where $\widehat{H}$ the Hamiltonian and the interatomic distances are R_{AB} are the constants for a particular nuclear configuration, due to Born-Oppenheimer approximation [180]. Hence the Born-Oppenheimer Hamiltonian as only the operator parts in the terms of the electrons is expressed as:

$$\widehat{H}^{electrons}\psi^{electrons} = E^{electrons}\psi^{electrons} \quad (2.2)$$

Where ψ is the wavefunction and *E* is the energy of the molecule expressed as $E = E^{electrons} + \sum_{A>B}^{nuclei}\sum_{B}^{nuclei}\frac{Z_A Z_B}{R_{AB}}$. There exist some DFT methods which are based on the basic introduction of the first principle quantum chemistry methods [181, 182, 183], which include the density functional theory (DFT), Hartree-Fock, *etc*.

2.1.2. Density functional theory

Compared to other *ab-initio* methods that compute the multi-electron and multi-dimensional wavefunctions, the density functional theory (DFT) computes only the electron density $\rho(r)$ for the condensed matter systems. Density functional theory (DFT) is the quantum mechanical theory used in chemistry and physics to simulate electronic structures and ground-state properties of many-body systems especially molecules, atoms, and condensed phases. Even though the DFT is based on the concept of Thomas–Fermi [184], it was developed by Kohn and Hohenberg [185], using the two Kohn-Hohenberg theorems.

The first Hohenberg and Kohn theorem states that for any system of interacting particles in an external potential $V_{ext}(r)$, the potential $V_{ext}(r)$, is determined uniquely by the ground

state particle density $n_o(r)$. This theorem lay a background work of reducing the many-body problem by using the function of the electron density. The second theorem states that the universal functional for the energy *E* [$n(r)$] in terms of the density $n(r)$ can be defined for any external potential $V_{ext}(r)$, and any particular $V_{ext}(r)$, the ground state of the system is the global minimum value of this functional, and the density $n(r)$ that minimizes the functional is the exact ground state density $n_o(r)$. The second theorem clearly defines the energy functional for the system and proves that the correct ground-state electron density minimizes this energy functionals.

The density functional theory determines the properties of many-body systems as a functional (function of a function), which depends on the electron density. Over the past decade, DFT became one of the most popular methods for calculations in solid-state physics and quantum mechanical simulations. This method was first recognized as an accurate method for quantum chemistry calculations until the 90s when the approximations involved in the method were improved to model the exchange and correlation interactions [186]. Despite these improvements, DFT still can't model the intermolecular interactions, especially the Van der Waals forces, charge transfer excitations, transition states, global potential energy surface, and some other strongly correlated systems. The great improvement was done by Kohn and sham in the calculation of the energy of electrons. They proved that the properties of the total ground state of interacting electron gas may be described by introducing certain functional of electron density $\rho(r)$, which depends on the positions of atoms [187].

$$E[\rho] = \int dr\rho(r)v_{ext} + \iint drdr' \frac{\rho(r)\rho(r')}{|r-r'|} + G[\rho] \tag{2.3}$$

where v_{ext} is the external field integrating the nuclei field, $G[\rho]$ comprises of the kinetic and the exchange-correlation energy of the interacting electrons. This expression is the minimum for the correct density functional $\rho(r)$. This made it possible for Kohn and Sham [188] to further develop the concept and suggest that $G[\rho]$ is:

$$G(\rho) = T(\rho) + E_{xc}(\rho) \tag{2.4}$$

where $T(\rho)$ is the kinetic energy of the non-interacting electrons with density $\rho(r)$ and the functional $E_{xc}(\rho)$ incorporated in the many-body effects of the exchange and correlation. Since the extent of many-body and correlation interactions is unknown, there is an approximation that exchange-correlation is obtained from known results of interacting electron systems of constant density. It is assumed that the exchange and correlation effects are not strongly dependent on inhomogeneities of the electron density away from the reference point r. Therefore, it is necessary to determine the set of the wave function ψ_i that minimizes the Kohn-Sham energy function. Thus, the electron density is then written as follows where *N* is the number of electrons:

$$\rho(r) = \sum_{i=1}^{N} |\psi_i(r)|^2 \tag{2.5}$$

The Kohn-Sham energy is then given by the self-consistent solution of the equation:

$$\left[-\nabla^2 - \sum_I \frac{2Z_I}{|r-R_I|} + 2\int \frac{\left(\rho(r')\right)}{|r-r'|} dr' + V_{xc}\,(r)\right]\psi_i = \varepsilon_i \psi_i \tag{2.6}$$

where R_I is the position of the nucleus I of charge Z_I, ε_i is the Lagrange factors. The exchange-correlation potential, V_{xc} is given by the functional derivative:

$$V_{xc}(r) = \frac{\delta E_{xc}[\rho(r)]}{\delta \rho(r)} \tag{2.7}$$

Since DFT is only known by approximation, the significance of this theory to practical uses can hardly be overstressed. It reduces the many-body problem to a single-particle problem with the effective local potential:

$$V(r) = \sum_I \frac{2Z_I}{|r-R_I|} + \int \frac{2\rho(r)}{|r-r'|} dr' + V_{xc}(r) \tag{2.8}$$

The most essential concept in DFT applications is how the functional E_{xc} is defined. The energy functional $E_{xc}(\rho)$ for inhomogeneous electron gas can be expressed as Coulomb interaction between the electron and its surrounding exchange-correlation hole [189, 190]:

$$V_{xc}[\rho] = \frac{1}{2}\int dr \rho(r) \int dr' \frac{(r,r'-r)}{|r-r'|} \tag{2.9}$$

The main problem with DFT as already mentioned is that the exact functionals for exchange and correlation are not known except for the free electron gas. However, some approximations can allow us to perform this calculation. There exist two commonly used approximations, which are the local density approximation (LDA) and the generalized density approximation (GGA).

2.1.3. Approximations: LDA and GGA

2.1.3.1. Local density approximation (LDA)

The motivation of using approximate methods is to describe the exchange-correlation energy as a function of the energy density. Local density approximations are class of approximations to the exchange-correlation functional in DFT that determined by the electronic density at each point in space. The LDA state that for the region of a material where the charge density is slowly varied, the exchange-correlation energy at that point can be considered the same as that for a locally uniform electron gas of the same charge density. It is a widely used approximation, which locally substitutes the exchange-correlation energy density of an inhomogeneous system by that of an electron gas evaluated at local density. It is based on two assumptions: firstly, the exchange and correlation effects come predominantly from the immediate vicinity of point r and secondly, these exchange and correlation effects do not depend strongly on the variations of the electron density in the vicinity of r [191]. The achievement of these two conditions results in some contribution from the volume element dr as if the element was surrounded by a constant electron density $\rho(r)$ of the same value as within dr. The exchange-correlation energy of the homogeneous electron gas $E_{xc}^{homo}(\rho_o)$ dependent on the homogeneous density ρ_o and replaces this for inhomogeneous systems with density $\rho(r)$ by:

$$E_{xc}^{LDA}\big(\rho(r)\big) = E_{xc}^{hom}(\rho_o)|_{\rho_o} = \rho(r) \tag{2.10}$$

For spin-unpolarised system (where the functionals depend only on the density) a local density approximation for the exchange-correlation energy is written as:

$$E_{xc}^{LDA}[\rho] = \int p(r)\varepsilon_{xc}(\rho)dr \quad \text{and} \quad \frac{\delta E_{xc}(\rho(r))}{\delta\rho(r)} = \frac{\partial[\rho(r)\varepsilon_{xc}(r)]}{\partial\rho(r)} \tag{2.11}$$

where ρ is the electronic density and E_{xc} the exchange-correlation energy density. However, this approximation only works with systems with slowly varying densities, such as the weakly perturbed electron gas and also works well even for systems that have very inhomogeneous electron densities such as atoms and molecules. When considering the *xc*-hole and the pair correlation function, we get a more detailed look at LDA.

$$\rho_{xc}^{LDA}(r_1, r_2) = \rho(r_1)[g^{hom}([\rho]; |r_1 - r_2| \tag{2.12}$$

where $g^{hom}[\rho]$ is the coupling constant integrated pair-correlation function of the homogeneous electron gas [192]. The exchange-correlation part of the pair-correlation function which is unaffected by the coupling constant integration is given by:

$$g_{xc}^{LDA} = ([\rho];\ r_1, r_2) = 1 - \frac{9}{2}\left[\frac{\sin(k_F(r_1)|r_1 - r_2| - k_F(r_1)|r_1 - r_2|\cos(k_F(r_1)|r_1 - r_2|))}{(k_F(r_1)|r_1 - r_2|)^3}\right] \tag{2.13}$$

where the $k_F(r)$ is the local Fermi wave vector defined as: $k_F(r) = \left(\frac{3}{\pi}\right)^{\frac{1}{3}}\rho(r)^{\frac{1}{3}}$. The exchange-correlation energy is decomposed into exchange and correlation terms linearly as: $E_{xc} = E_x + E_c$, where E_x and E_c are the exchange energy and the correlation energy, respectively. The exchange term takes on an analytic form for the homogeneous electron gas (HEG). The exchange-energy density of a HEG is known analytically. The LDA for exchange employs this expression under the approximation that the exchange-energy in a system where the density is not homogeneous, is obtained by applying the HEG results pointwise, yielding the expression [193].

$$E_x^{LDA} = -\frac{3}{4}\left(\frac{3}{\pi}\right)^{\frac{1}{3}}\int \rho(r)^{\frac{4}{3}}dr \tag{2.14}$$

This equation satisfies the correct exchange scaling. There are corresponding equations for the correlation part of $g^{hom}[\rho]$ and $E_c^{LDA}[\rho]$. The LDA xc-hole is spherical around the reference electron and is given as:

$$\rho_{xc}^{LDA}(r_1, r_2) = \ \rho_{xc}(r_1, s) \tag{2.15}$$

where $s = |r_1 - r_2|$ and it also satisfies the sum rule:

$$\int \rho_{xc}^{LDA}(r_1, r_2)dr_2 = 4r\int_0^\infty \rho_{xc}^{LDA}(r_1, s)s^2 ds = -1 \tag{2.16}$$

Analytic expressions for the correlation energy of the HEG are not known except in the high-density and low-density limits corresponding to infinitely-weak and infinitely-strong correlation [194]. For a HEG with density ρ, the high-density limit of the correlation energy density is:

$$\varepsilon_c = AIn(r_s) + B + r_s(Cin(r_s) + D) \tag{2.17}$$

and the lower limit is given:

$$\varepsilon_c = \frac{1}{2}\left(\frac{g_o}{r_s} + \frac{g_1}{\frac{3}{r_s^2}} + \cdots\right) \tag{2.18}$$

where the Wigner-Seitz radius is related to the density as;

$$\frac{4}{3}\pi r_s^3 = \frac{1}{\rho} \tag{2.19}$$

LDA approximates the energy of the true density by the energy of a local constant density and fails in situations where the density undergoes rapid changes such as in molecules. The Local Spin Density (LSD) also is not accurate enough for most chemical applications, which require determination of energy differences with considerable precision. The LSD has been used to calculate the electronic structure of solid-state physics for many years [195, 196]. This approximation is given by:

$$E_{xc}^{LSD}[\rho_\uparrow, \rho_\downarrow] = \int d^3r \rho(r) \varepsilon_{xc}^{unif}\,[\rho_\uparrow(r), \rho_\downarrow(r)] \tag{2.20}$$

where $\varepsilon_{xc}^{unif}(\rho_\uparrow, \rho_\downarrow)$ is the exchange-correlation energy per particle of a uniform electron gas [197, 198, 199].

2.1.3.2. General gradient approximation (GGA)

The generalized gradient approximation (GGA) is an alternative approach since it improves the LDA by extending the exchange-correlation functional with terms containing a gradient of the electron density. The gradients measure the changes of the electron density and can be used to advance to the local density approximations. Most of the gradient developments are based on the weakly varying electron gas [192]. These approximations are called the gradient expansion approximations (GEA) and can be summarised as:

$$E_X^{GEA} = E_X^{LDA}[\rho] + \beta \int \frac{(\nabla\rho)^2}{\rho^{\frac{4}{3}}} dr + \cdots \quad (2.21)$$

$$E_C^{GEA} = E_C^{LDA}[\rho] + \int C(\rho) \frac{(\nabla\rho)^2}{\rho^{\frac{4}{3}}} dr + \cdots \quad (2.22)$$

where $C(\rho)$ is a functional determined by the response theory and β is a constant. But the GEA do no improvements to the LDA since the densities in molecule and atom don't very slowly over space. Upon the analysis of the xc-holes, thy show that the short-range is improved, however, the long-range is made worse [200]. The corresponding approximation for the GEA is the generalized gradient approximation (GGA), which can be written as:

$$E_{XC} = E_{XC}[\rho(r), \nabla\rho(r)] \quad (2.23)$$

This can make great improvements over LDA results with accuracy approaching that of the correlated wavefunction. Even though there is only one LDA, there are various parameterizations of the GGA which include the Perdew-Wang 86 (PW86), Lee-Yang-Parr (LYP), Perdew-Wang 91 (PW91), Perdew-Burke-Enzerhof (PBE), and Revised Perdew-Burke-Enzerhof (RPBE). Some of these are semi-empirical, in that experimental data (e.g. atomization energy) is used in their derivations and others are found entirely from the first principles. The most used functionals are PW19 due to Perdew and Yang [199, 200, 201]. However, the new generalized gradient approximation (GGA) has the generalized correlated functional in the form:

$$E_{XC}^{GGA} = \int d^3 r f(\rho_\uparrow(r), \rho_\downarrow(r), \nabla\rho_\uparrow, \nabla\rho_\downarrow) \quad (2.24)$$

The expression was found to reduce the LSD atomization errors by a factor 5 [202]. The mostly used GGA's are the Becke GGA for exchange energy [203], the exchange-correlation GGA's by Perdew [204], and the Perdew and Wang [205, 206, 207]. The GGA correlation to the LDA is of the form:

$$E_{XC}^{GGA}[\rho_\uparrow, \rho_\downarrow] = E_X^{LDA} - \beta \int \sum_\sigma \frac{\rho_{\sigma(r)}^{\frac{4}{3}} x_\sigma^2}{1+6\beta x_\sigma \sinh^{-1} x_\sigma} d^3 r \quad (2.25)$$

where $E_X^{LDA} = C_{X\sigma} \sum \rho_\sigma^{\frac{4}{3}}(r) d^3(r)$, $C_{X\sigma} = \frac{3}{2}\left(\frac{3}{4\pi}\right)$, $X\sigma = \frac{|\nabla\rho|}{\rho_\sigma^{\frac{4}{3}}}$, σ represents the $\uparrow or \downarrow$ electron spin. β is a constant parameter to obtain the correct exchange energy for a noble gas. The following correlation functional predicted by the Perdew and Wang [205] predicts the correlation energy of useful accuracy for electron gas with slowly varying density:

$$E_{XC}^{GGA} = \int (\rho_\uparrow(r), \rho_\downarrow(r), \nabla\rho_\uparrow, \nabla\rho_\downarrow) dr^3 + \int \frac{C_C(\rho)|\nabla\rho|^2}{de^\phi \rho(r)^{\frac{4}{3}}} d^3r \quad (2.26)$$

where $d = 2^{\frac{1}{2}}\left[\left(\frac{1+\zeta}{2}\right)^{\frac{5}{3}} + \left(\frac{1-\zeta}{2}\right)^{\frac{5}{3}}\right]$, $\phi = 0.1929\left[\frac{C_C(\infty)}{C_C(\rho)}\right]\frac{|\nabla\rho|}{\rho^{\frac{7}{6}}}$, $\zeta = (\rho_\uparrow, \rho_\downarrow)/\rho$ and $C_C(\rho)$ is a rotational polynomial of the density that contains the fitting parameters. The exchange functional written by Perdew-Burke-Ernzerhof is discussed in the form that contains an explicit enhancements factor over the local exchange factor, widely known as the GGA-PBE exchange-correlation

$$E_X^{PBE} = \int \rho(r) \varepsilon_X^{LDA}[\rho(r)] F_{XC}(\rho, \xi, s) dr \quad (2.27)$$

where ρ is the local density, ξ is the relative spin polarization, and $s = \frac{|\nabla\rho(r)|}{2k_F\rho}$ is the dimensionless density gradient. The factor is enhanced in the following way:

$$\left(sF_X = \left(\frac{1}{k+s^2\mu}(k + s^2\mu + s^2 k\mu)\right)\right) \quad (2.28)$$

where $\mu = \beta\left(\frac{\pi^2}{3}\right) = 0.21951$ with $\beta = 0.066725$. The correlation energy is;

$$E_C^{PBE}[\rho_\uparrow, \rho_\downarrow] = \int \rho(r) \left[\varepsilon_C^{LDA}(\rho, \zeta) + H(\rho, \zeta, t)\right] dr \quad (2.29)$$

with

$$H(\rho, \zeta, t) = \left(\frac{e^2}{a_0}\right)\gamma\phi^3 \times In\left\{1 + \frac{\beta}{\gamma}t^2\left[\frac{1+At^2}{1+At^2+A^2t^4}\right]\right\} \quad (2.30)$$

where $A = \frac{\beta}{\gamma}\left[e^{\varepsilon_C^{LDA}[\rho]/\gamma\phi^3} - 1\right]^{-1}$, $t = \left|\frac{\nabla\rho(r)}{2k_s\rho}\right|$ is the dimensionless density gradient, $ks = \left(\frac{4k_F}{\pi}\right)^{\frac{1}{2}}$ is the TF screening wave number and $\phi(\zeta) = \left[(1+\zeta)^{\frac{2}{3}} + (1-\zeta)^{\frac{2}{3}}\right]$ is the spin-scaling factor. Under uniform scaling to the high-density limits, $\mathrm{E_c^{GGA}}$ tends to

$$-\frac{e^2}{a_0}\int d^3r n\gamma\phi^3 \times In\left[1 + \frac{1}{\frac{\chi s^2}{\phi^2} + \left(\frac{\chi s^2}{\phi^2}\right)^2}\right] \tag{2.31}$$

where $s = \frac{|\nabla \mathrm{n}|}{2k_F n} = \left(\frac{r_s}{a_o}\right)^{\frac{1}{2}}\phi t/c$ is another dimensionless density gradient.

2.1.4. Plane-wave pseudopotential methods

The Plane-wave pseudopotential is a method that calculates the variation self-consistent solution with accuracy. Its advancements and perfections enable to predict the static and dynamic properties of the crystalline solids and the molecules [207]. The plane-wave pseudopotential method deals with the weak pseudopotential and calculates the geometry optimization, mainly the relaxation of internal parameters.it can also simulate the electronic ground states for metals, insulators, and the semiconductors.

2.1.4.1. Plane-wave basis set

The plane-wave method as outlined above is more reliable and powerful to calculate the properties for materials. It was designed for periodic solids and used for problems such as exploring the supercell approach for atoms and surfaces. The roots of this method are based on the Bloch's theorem that states that the eigenstates ψ of a one-electron Hamiltonian $H = -\frac{\hbar^2\nabla^2}{2m} + V(r)$, where $V(r+T) = V(r)$ for all Bavais lattice translation vectors T can be chosen to be a plane wave times a function with the periodicity of Bravias lattice. This theorem allows the electronic wave functions to be expanded in terms of a discrete set of plane waves as follows:

$$\psi_i = e^{ikr}\mathrm{F_i(r)} \tag{2.32}$$

$\mathrm{F_i(r)}$ is the cell periodic term, described as:

$$F_i(r) = \sum_{G\rightarrow} C_{i,G} e^{iGr} \tag{2.33}$$

where G is the reciprocal lattice vectors of the periodic cell. Each distinct electronic wavefunction $\psi_{k_i(r)}$ can be written as:

$$\psi_{k_i(r)} = \sum_{G\rightarrow} C_{i,K+G} e^{-[i(K+G).r]} \tag{2.34}$$

where $C_{i,K+G}$ are the coefficient of plane waves and they depend entirely on the specific kinetic energy, $\left(\frac{\hbar^2}{2m}\right)|K+G_c|^2$ and the plane-wave with high kinetic energy are less important than those with low kinetic energy. The cut-off energy can be calculated in order of finite basis set as:

$$E_{cut} > \frac{\hbar^2}{2m}|K+G_c|^2 \tag{2.35}$$

The cut-off is chosen by increasing its magnitude until its total energy converges to a required accuracy [208]. However, an increase in the number of a plane wave can describe more rapidly varying features of an infinitely large number of basis set achieved. In a nutshell, the finite basis set is obtained when the finite cut-off energy is introduced to the discrete plane-wave basis set. Although this might lead to computational errors, one should increase the cut-off energy until it fully converges. One should also use a denser set of *k*-points to reduce errors and ensure good convergence.

2.1.4.2. Pseudopotentials

The pseudopotential is the theory that aims to reduce the difficulty of calculating energy density. The theory is constructed such that the pseudo wavefunction has no radical nodes within the core regions and that the pseudo and potential agrees well with the true wavefunction and potential outside some cut-off radius E_{cut}. Furthermore, the pseudopotential should preserve the properties of the element, including the phase shifts on scattering across the core, and these phase shifts will generally depend upon the angular momentum. This theory replaces the Coulomb potential of the core electrons and nucleus with potential acting on the valence electrons, due to the low reactivity of the core

electrons. The core electrons localized around the nucleus, the wavefunctions barely overlap with the core electron's wavefunction of the neighbouring atoms. Hence, in the core region of an atom, the core wavefunctions oscillate rapidly due to the strong Coulomb potential. Irrespective of the chemical environment of the atom, the distribution of the core electrons is the same. This is a plus since the electrons have to be treated and fewer eigenstates of the Kohn-Sham have to be calculated. On the other hand, the total energy is largely reduced by the absence of the core electrons in the calculations which makes energy difference calculations between the atomic configurations much more numerically stable. An introduction of the pseudopotential approximation is an attempt to limit the unsolved complicated effects of the core electrons in motion and their nucleus with the effective potential [209, 210]. The properties of the pseudopotential are explained further in the schematic diagram shown in Figure 5. The valence wavefunctions oscillate rapidly in the region occupied by the core electrons, which is because of the strong ionic potential. Hence, the orthogonally between the valence and core electrons is maintained due to these oscillations. In general, the pseudopotential should be non-local, with no projectors for different angular momentum states. The general formulation of the pseudopotential is outlined as:

$$\mathrm{V}_{ions} = \sum |lm\rangle V_i \langle lm| \tag{2.36}$$

where $|lm\rangle$ are the spherical harmonics and V_i is the pseudopotential for angular momentum.

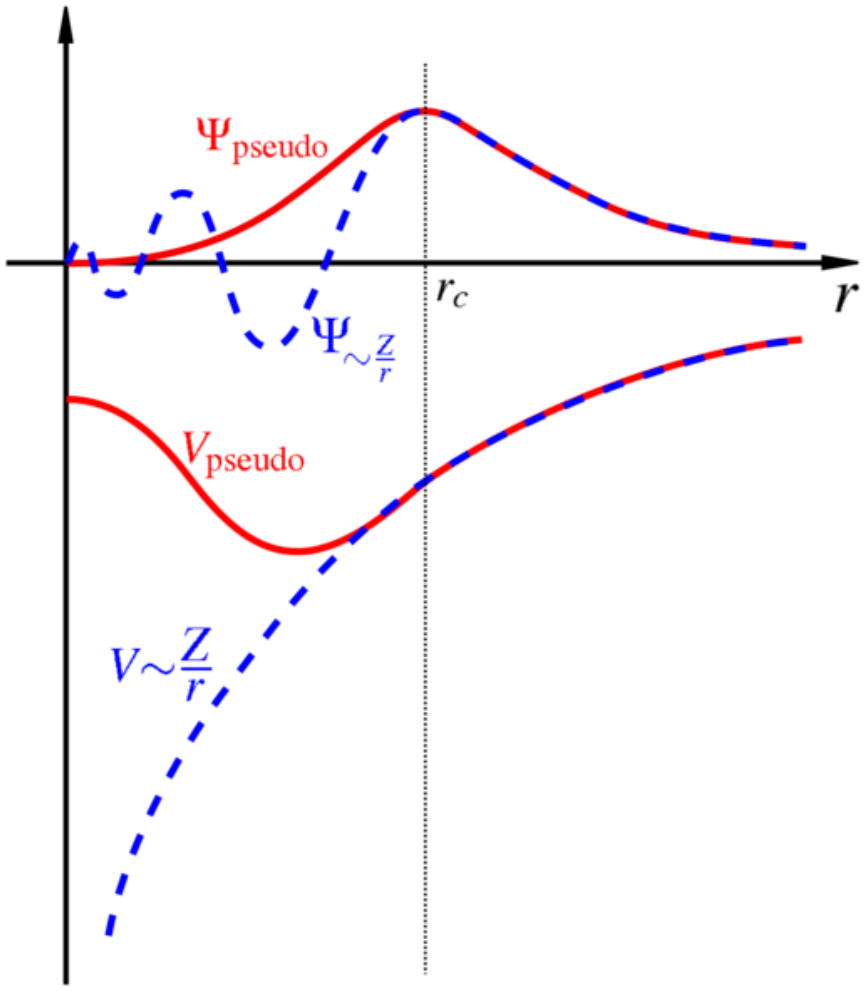

Figure 5: Schematic diagram for the illustration of an atomic all-electron wavefunction and the corresponding atomic pseudo wavefunction.

2.1.4.3. Projector augmented wave (PAW) method

The wavefunction of materials has quite different signatures in different regions of space. In the bonding region, the wavefunction is smooth while close to the nucleus it oscillates rapidly due to the large attractive potential of the nucleus. This is the drawbacks of the electronic structure method when describing the bonding region with a high degree of accuracy while accounting for the large variations in the atom centre. The augmented-wave method was formulated to divide the wavefunction into parts, which are the partial-wave expansions within atom-cantered spheres and the envelope function outside the

spheres. The partial-wave expansions and the envelope function are matched with a term and derivative at the sphere radius.

The projected augmented wave (PAW) is an approach that combines the linear augmented plane-wave (LAPW) method with the formal simplicity of the traditional plane-wave approach [211]. Its wavefunction can be expressed as:

$$\psi(r) = \tilde{\psi}(r) + \sum_{\Lambda}[\phi_{\Lambda}(r) - \tilde{\phi}_{\Lambda}(r)]\langle \tilde{p}_{\Lambda}|\tilde{\psi}\rangle \quad (2.37)$$

where $|\psi\rangle$ and $|\tilde{\psi}\rangle$ are the wavefunction and the pseudo-wavefunction respectively, $|\phi_{\Lambda}\rangle$ and $|\tilde{\phi}_{\Lambda}\rangle$ are the one-electron Schrodinger equations for the isolated atoms and the pseudo partial wave respectively and the $\tilde{p}_{\Lambda}$ are the projector functions. In this formulation (see equation 16), $|\psi\rangle$ behaves like an atom within an atom-cantered sphere (augmentation region) and outside envelope function (interstitial region). Within the augmented region, $|\tilde{\psi}\rangle$ is cancelled out by the expansion of $|\tilde{\phi}_{\Lambda}\rangle$ that is in such a way that it's equal to $|\phi_{\Lambda}\rangle$ interstitial regions. The full all-electron wavefunction is used while the core electrons are considered fixed at an atomic solution, and it depends on the full charge and spin density, such as the hyperfine [212].

2.1.5. Implications in VASP

The Vienna *ab-initio* simulation package (VASP) is an electronic program for solid materials. It performs *ab-initio* quantum mechanical molecular dynamics using the plane-wave basis set, pseudopotentials, and the projected augmented wave method. The program is based on the DFT method, however, it also allows the use of hybrid functional mixing DFT, Hortree-Fork exchange, many-body perturbation theorem, electronic corrections within random phase approximation [213]. VASP uses efficient matrix diagonalization schemes and efficient Pulay/Broyden charge density mixing. This technique is highly advanced that it also avoids all the problems possibly occurring in the original Car-Parrinello method, which is based on the simultaneous integration of electronic and ionic equations of motion. The interaction between ions and electrons is described by ultra-soft Vanderbilt pseudopotential (US-PP) [214] or by the PAW method. Ultra-soft pseudopotentials and projector-augmented wave allow for a considerable

reduction of the number of plane waves per atom for transition metals and first row elements. Forces and the full stress tensor can be calculated with VASP and used to relax atoms into their instantaneous ground state. The densities of states are also calculated using the VASP code. VASP is based on a program initially written by M. Payne [200] at the MIT. Hence, VASP has the same roots as the CASTEP/CETEP code but branched from this root at an early stage.

Spin-polarized density functional theory (DFT) calculations were performed as implemented in the Vienna *Ab-initio* Simulation Package (VASP) [215]. All calculations were carried out within the generalized gradient approximation (GGA) using the Perdew, Burke, and Ernzerhof (PBE) exchange-correlation functional [216]. The kinetic energy cut-off was fixed at 560 eV for the expansion of the Kohn-Sham (KS) valence states. A Γ-centred Monkhorst-Pack grid of 5x5x1 *k*-points was used for the integration of all surfaces in the reciprocal space. The core electrons and their interaction with the valence electrons were described using the projector augmented-wave (PAW) method [217] in the implementation of Kresse and Joubert [199]. The core electrons are comprised of 3*s* and 1*s* for manganese and oxygen, respectively. While all the electrons for lithium are treated as valence electrons. The semi-empirical method of Grimme with the Becke-Johnson damping [D3-(BJ)] [218] was also included in our calculations for modelling the long-range dispersion interactions, which is required to describe surfaces properly [219]. Gaussian smearing with a width of 0.05 eV was set to improve the convergence of the Brillion zone integrations during geometry optimizations [219]. The tetrahedron method with Blöchl corrections were used to obtain accurate electronic properties, magnetic properties, and total energies [220]. The Hubbard correction [221] in the formulation of Dudarev *et al.* [222] was applied to improve the description of the localized 3*d* Mn electrons. We used the effective parameter, U_{eff} = 4.0 eV which is within the range of values reported in the literature [223, 144, 148, 79].

2.2. BACKGROUND OF THE PROPERTIES STUDIED

2.2.1. Geometry optimization

Before any calculations, we performed geometry optimization, which is the relaxation of atomic positions and cell parameters. This procedure is not based only on finding the structural minimum, but also the inter-nuclear Coulomb energy. Figure 6 shows the profile representation of the local and global minima separated by the transitional state. One of the greatest challenges of condensed matter physics is the identification of the lowest energy path for the rearrangements of atoms from one stable configuration to the other. The energy maximum along the minimum energy path is point energy which gives the activation energy (E_a), which is calculated as the total energy difference between the initial state and the saddle point. The activation energy (ΔE) of the reaction can also be calculated as the energy difference between the final state and the initial state.

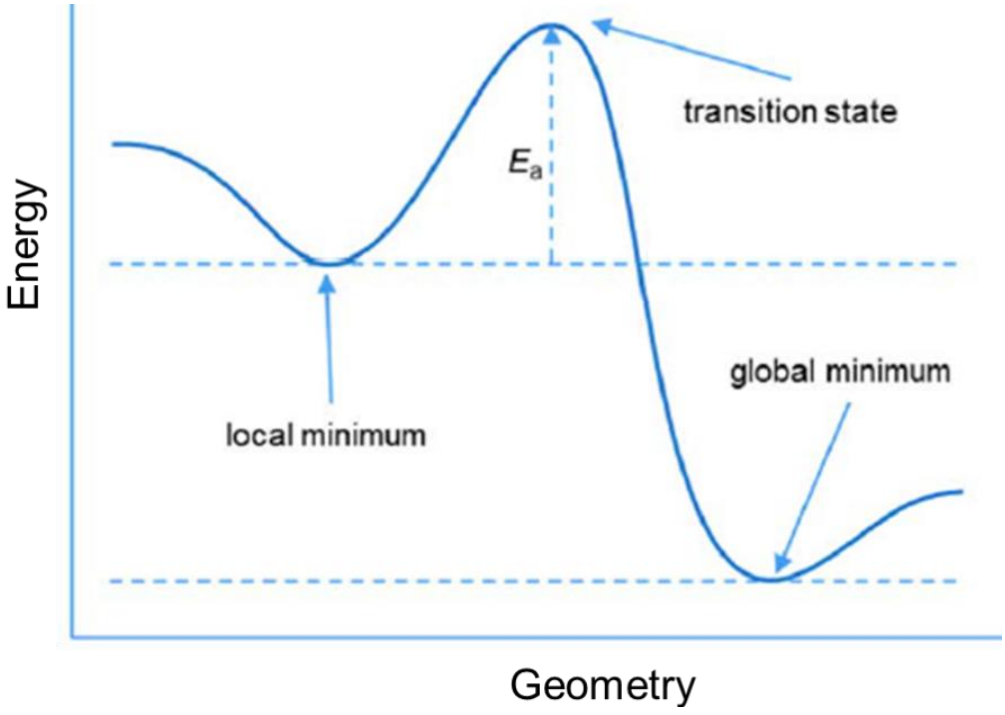

Figure 6: Representation of local and global minima with the transition state *[224]*.

2.2.2. Heats of formations

The standard heat of formation of a specific material is the change of enthalpy that accompanies the formation of 1 mole of a substance in its standard state. The calculation for the heats of formation is based on the application of Hess's law, which states that the standard enthalpy of an overall reaction is the sum of the standard enthalpies of individual reactions into which the reaction may be divided [225]. The heats of formation and associated entropies provide a fundamental understanding of stabilities and phase diagrams construction. The heat of formation (ΔH_f) is estimated by:

$$\Delta H_f = E_m - \sum_i N_i E_i \tag{2.38}$$

where E_m is the total energy of the molecule, E_i is the total energy of the element and i in the molecule and N_i is the number of atoms in the molecule.

2.2.3. Density of states

The density of states (DOS) is the representation of the number of states in specified energy. It gives a clear understanding of how chemical bonds are created and how the molecules interact with solid surfaces. Inside the Brillouin zone, each *k*-point defines energy levels that form energy bands which can be represented using a band diagram plot. The higher DOS at an energy level indicates that there are many states available for occupation and zero DOS indicates that no states can be occupied at that energy level. The energy level within the material's DOS that is extremely useful for characterizing the electrical behaviour of the material is known as the Fermi level (E_F). In an insulator, E_F lies within a large bandgap, far away from any states that can carry current. For doped semiconductor, E_F is close enough to a band edge that there are a dilute number of thermally excited carriers residing near that band edge. In a metal or semimetal, E_F lies within a delocalized band. The DOS can also be represented for each ion in each system using the volume that it occupies. Furthermore, it can be represented using the *s, p,* and *d* bands, which can enable interpretation of the relative energies of different bands and their interactions in bonds.

2.2.4. Phonon dispersions

Phonon dispersion is a phenomenon that describes the optical properties of a material. The optical properties of materials are defined as the interaction of the material with electromagnetic radiation in the visible region. The photon interactions with the crystal structure of a material result in a variety of optical phenomena. The transfer of photon energy to the material may undergo absorption, transmission, photons of identical energy may immediately be emitted by the material via reflection and the velocity of photons may change, during transmission causing refraction. Different materials have different band structures. Metals consist of partially filled high-energy conduction bands and non-metals consist of various energy band structures. All four optical phenomena (absorption, reflection, transmission, and refraction) are important for these materials. In this work, we calculated and plotted the phonon dispersions using the PHONON code [226] to describe the stability of the spinel bulk structure.

2.2.5. Elasticity

Elastic properties give an insight into the strength of the material against an externally applied strain and could be used as a stability criterion for structural transformation [227, 228]. It can also be related to various fundamental solid-state properties, such as the equation of states and the phonon dispersion spectra. The mechanical stability of homogeneous crystals has been widely studied in both theoretical and computational investigation [229]. Born started the systematic study of crystal stability under load. The well-known Born stability criteria are a set of conditions on the elastic constants (C_{ij}) which are related to the second-order change in the internal energy of a crystal under formation. But, Hill and Milstein suggested that the convexity of the internal energy in a crystal under stress is coordinate dependent and hence the ranges of Born stability are strongly sensitive to the choice of coordinates [230]. Wang *et al.* have suggested that the Born conditions are only valid for the mechanical stability of unstressed systems and not valid for the stressed systems [231, 232]. Barron and Klein also indicated that the normal definition of the elastic constants derived the Helmholtz free energy cannot be directly applied to the study of the stress-strain relationship of a stressed state [233]. Wang and

co-workers [231, 232] demonstrated, however, that elastic constants cannot be used as stability criteria for a stressed system. They suggested the use of elastic stiffness coefficients as stability criteria for isotropic stress. For anisotropic stress, they obtained a more general form from path-dependent finite displacements. The stability criteria have been strongly formulated in terms of elastic stiffness coefficients (C_{ij}) which govern the proper relations of stress and strain at finite strain by considering both the internal and the external work was done during the process of deformation [233]. This strongly suggests that the stability analysis depends mainly on a proper generalization of the zero-stress constants valid for arbitrary stress. Bulk modulus is also one of the most important parameters that characterize the physical property of a material system because it also measures the degree of stiffness or the energy required to produce a given volume deformation, while shear modulus describes the resistance to shape change caused by shearing force; Young's modulus reflects the resistance of materials against uniaxial tensions [234]. The Bulk modulus depicts the bonding characters in the material and it is usually used as an indicator for material strength and hardness and is the inverse of compressibility [235]. Pugh introduced the ratio of bulk to shear modulus of polycrystalline phases (B/G) by considering that shear modulus represents the resistance to plastic deformation, while the bulk modulus represents the resistance to fracture. A high B/G value is associated with ductility, while a low B/G value is related to brittleness. The critical value separating ductility and brittleness is 1.75 [236]. Elastic constants of a material describe its response to the externally applied strain or the stress required to maintain a given deformation and provides useful information of the strength of the material, as characterized by Bulk modulus (B), shear modulus (C), Young's modulus (E), Poisson's ratio (υ) and Shear anisotropy factor (A). The quadratic dependence of the crystal energy E on the strain is expected for small deformations.

The mechanical stability criteria are different depending on the kind of material. For each material, both stress and strain have three tensile and three shear components, giving six components in total. According to the theory of elasticity, a 6×6 symmetry matrix with 36 elements is needed to describe the relationship between stress and strain, such that $\sigma_1 = C_{ij}\varepsilon_j$ for small stresses (σ), and strain (ε) [237]. Elastic constants of a material describe its response to the externally applied strain, or the stress required to maintain. a given

deformation and provides useful information on the strength of the material, as characterized by Bulk modulus (*B*), shear modulus (*G*), Young's modulus (*E*), Poisson's ratio ($_{v}$) and Shear anisotropy factor (*A*). The quadratic dependence of the crystal energy *E* on the strain is expected for small deformations. The elastic moduli for the hexagonal crystal are given as follows

2.2.6. Surface calculations

Surfaces can be modelled from a bulk structure cleaving along different crystallographic planes known as Miller indices. The Miller indices are lattice planes determined by three integers commonly represented by h, k and l. Each index represents a plane orthogonal to the direction, based on the reciprocal lattice vectors and they indicated as (h, k, l). For example, the Miller indices (001) represents a plane orthogonal to the l direction, (011) represents a plane orthogonal to both k and l directions. Some index planes can be orthogonal to the negative $h, k,$ and l directions. For example, $(00\bar{1})$ represent a plane orthogonal to the negative l direction.

Atoms at the modelled surfaces commonly tend to have low coordination compare to those in the bulk. Because of the presence of the dangling bonds and the changes in coordination of the surface atoms, the surface geometry will relax or maybe reconstruct to let the atoms to find the equilibrium positions. In surface constructions, there two common models, namely, periodic and the cluster model. In the periodic slab model, two directions generate exposed surfaces with vacuum on either side of the slab, while the cluster model treats the surface as a small isolated cluster of atoms, and one of the resulting facets has the same symmetry and atomic arrangement as the crystal intended to study. Most importantly when using the periodic slabs, the vacuum thickness should be large enough to avoid surface consecutive slabs from interacting with each other, and also the thickness should be thick enough to avoid interactions of surfaces of one slab. In this study, the slabs were modelled from a fully optimized pristine bulk. The bottom atoms were frozen to mimic the bulk, and the uppermost atomic layers could relax as shown in Figure 7. We then named the slabs without fixed atomic layers as unrelaxed surfaces, and those with upper atomic layers which could relax as the relaxed surfaces.

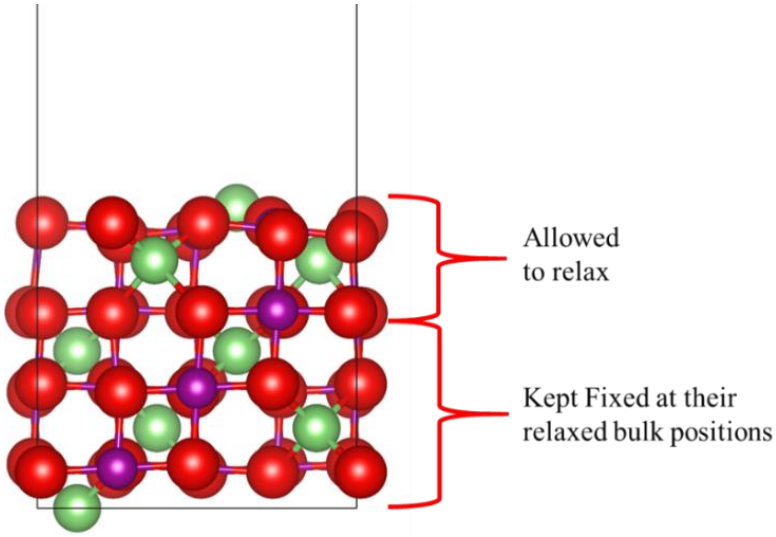

Figure 7: Representation of how the half-relaxed slab was calculated. The uppermost layers could relax while the lower surfaces were kept fixed at their relaxed bulk positions.

2.2.6.1. Surface stability

Surface stability influences the reactivity of the reactivity. The lesser the surface stability the more relativity towards adsorbing species. Surface energies of the modelled facets were calculated for the relaxed and unrelaxed slabs. The unrelaxed surface energies (γ_u) were evaluated from static calculations as

$$\gamma_u = \frac{E_{u,slab} - E_{bulk}}{2A} \tag{2.39}$$

where E_u is the total energy of an unrelaxed slab, E_{bulk} is the total energy of the bulk with the same number of formula units as the slab and A is the surface area of the slab. The relaxed surface energies (γ_r) were also calculated for the spinel following geometry optimization of half of the slab, where the two bottommost layers were kept fixed at their relaxed bulk positions while the top layers were allowed to relax as shown in Figure 7 below.

Since the slabs were comprised of both the relaxed and unrelaxed surfaces, the surface energies were calculated as

$$\gamma_u + \gamma_r = \frac{E_r - E_{bulk}}{A} \tag{2.40}$$

where E_r is the total energy of the half-relaxed surface. The degree of relaxation (R) was also calculated for all the surfaces as

$$R = \frac{\gamma_u - \gamma_r}{\gamma_u} \times 100 \quad (2.41)$$

The surface free energy of a given plane is a measure of the stability of that surface, where the surface with the lowest positive value is the most stable.

2.2.6.2. Adsorption energy

The adsorption of molecules on the surfaces of solids is an interesting and useful phenomenon when investigating surface reactivity of materials. Atoms and molecules interact with surfaces with forces originating either from the "physical" van der Waals interactions or from the "chemical" hybridization of their orbitals with those of the atoms of the substrate. Depending on which contribution dominates, we speak of physisorption or chemisorption. These are limiting cases since hybridization is always present at small enough adsorption distances, even for adsorbed rare gases. Physisorption is based on the van der Waals interactions between the adsorbate and the substrate and between the adsorbed molecules. The binding energy depends on the number of atoms involved and varies between few meV (light gases) and few eV (large organic molecules). The geometrical structure and electronic characteristics of the physisorbed molecule or atom, and of the surface are essentially preserved. A physisorbed molecule can spontaneously leave the surface after a certain time. Chemisorption, on the other hand, occurs when there is the formation of a chemical (often covalent) linkage between adsorbate and substrate. Binding energies are typical of several eV. Compared to physisorption, the geometrical structure and electronic characteristics of the chemisorbed molecule or atom are strongly perturbed.

When molecules or atoms adsorb on the surface, and the created bond with the surface will release energy. The total energy of this formation is called binding or adsorption energy (E_{ads}). E_{ads} is a function of coverage and distribution of the adsorbates at the surfaces. Considering the molecule, Z, adsorbed on a given surface, the adsorption energy is calculated as:

$$E_{\text{ads}} = E_{\text{Z+surface}} - (E_Z + E_{\text{surface}}) \quad (2.42)$$

where, $E_{\text{Z+surface}}$ is the total energy of the surface with the molecule Z adsorbed, E_{Z} is the total energy of the isolated molecule Z and E_{surface} is the total energy of the pristine surface. By definition, a positive value of E_{ads} indicates an endothermic and unfavourable adsorption process, whereas a negative value indicates an exothermic and favourable adsorption process.

2.2.7. Vibrational frequencies

Vibrational frequencies are related to the force constant, which are the second derivatives of the total energy concerning the displacements. The method comprises calculations of vibrational frequencies from the 2nd derivatives of the potential energies with respect of the atomic positions which were moved by small displacements to ensure they fall within the harmonic part of the potential well. They are necessary for reasons such as to locate the steady-state on the hypersurface and ensure that the stationary optimized point is minimum on the potenti9al energy surface. Can also be related to the infrared (IR) or Raman spectra and can be directly compared to experimental data. The vibrational frequencies (ω) are determined from the eigenvalues of the Hessian of the Born-Oppenheimer energy, which is scaled by nuclear masses:

$$det\left|\frac{1}{\sqrt{M_I M_J}} * \frac{\partial^2 E(R)}{\partial R_I \partial R_J} - \omega^2\right| = 0 \quad (2.43)$$

A stationary point can be confirmed as a local minimum if all the second derivatives are positive and if imaginary frequencies are found, then the stationary point can be assigned as a saddle point. The Hessian matrix is calculated using the finite difference and it is determined by the equation:

$$H(f) = \begin{bmatrix} \frac{\partial^2 f}{\partial r_1^2} & \frac{\partial^2 f}{\partial r_1 \partial r_2} \cdots & \frac{\partial^2 f}{\partial r_1 \partial r_n} \\ \frac{\partial^2 f}{\partial r_2 \partial r_1} & \frac{\partial^2 f}{\partial r_2^2} \cdots & \frac{\partial^2 f}{\partial r_2 \partial r_n} \\ \frac{\partial^2 f}{\partial r_n \partial r_1} & \frac{\partial^2 f}{\partial r_n \partial r_2} \cdots & \frac{\partial^2 f}{\partial r_n \partial r_n} \end{bmatrix} \quad (2.44)$$

2.2.8. Wulff crystal morphologies

The Wulff construction for particle morphologies was based on the famous paper on the Heterogeneous substances by J.W. Gibbs [238]. He concluded that a given quantity of matter will have a shape such that the total surface energy is minimal. This suggests that the shape of a crystalline solid will be a polyhedron that is composed of faces parallel to the hkl plane allowed. Thus, the surface morphologies will be dominated by the facets with low surface energy. Decades later, G Wulff [239] suggested that the polyhedral shape that corresponds to the lowest surface energy for a crystalline substance can be in the following way: One chooses a constant *c* and a Cartesian set of axes. Starting from the origin, O, one draws a plane that is normal to the $[hkl]$ vector and has a distance $d_{hkl} = c \cdot \gamma_{hkl}$ from O. The first prove of Wulff construction was proposed by vou Laue in 1943, furthermore, upgraded, and explained in details [240]. It was also discussed that the polyhedral constructed using the Wulff constructions: (i) depends only on the ratios between surface tensions not on their absolute values. (ii) Contains some facets with high Miller index as in most cases since they have high surface tension than the low Miller index surfaces. (iii) Does not consider the edge- and vertex-energies and (iv) has the same symmetry as the bulk structure.

2.2.9. Charge transfers analysis

The charge identification for a material can give an insight into the bonding of the contributing atoms. Based on the adsorbed systems, charge analysis can characterize the nature of the bond between the interacting atoms. Covalent bonds are identified when the charge transfer between the interacting atoms is small or negligible, and this interaction is known as physisorption. Several methods exist for charge transfer analysis which gives different results [241]. In this work, we use Bader charge analysis [242] as implemented in the VASP code using the Henkelman algorithm [243]. The Bader method determines the surface zero flux in the charge density around an atom. The volume enclosed by the surface is named Bader basin, and the electron densities inside are summed to find the Bader charge for that atom. Because of the delocalization of DFT, the

Bader analysis underestimates the ionic charges. Besides the delocalization of DFT, the Bader is reliable in identifying trends for similar systems.

CHAPTER THREE

STABILITY OF LITHIUM MANGANESE OXIDE $LiMn_2O_4$ SPINEL BULK STRUCTURE

CHAPTER SUMMARY

In this chapter, we use the density functional theory (DFT) to study the stability of the bulk spinel structure. We discuss the convergence test, structural, electronic, mechanical, and vibrational properties. The convergence test involves cut-off energies and k-points. Structural properties are discussed based on the lattice parameters and the heats of formation. Electronic properties are composed of the density of states and band structures, while the mechanical properties are the elastic constants and moduli. The vibrational properties are phonon dispersions, wherein we study the vibrational stability of the structure. This chapter mainly focuses on the stability of the bulk structure and gives insight into the properties of the spinel $LiMn_2O_4$ structure.

3.1. METHOD

The density functional theory (DFT) calculations as implemented in the Vienna *Ab-initio* Simulation Package (VASP) [215] was used to investigate the $LiMn_2O_4$ bulk properties. All calculations were carried out within the generalized gradient approximation (GGA) using the Perdew, Burke, and Ernzerhof (PBE) exchange-correlation functional [216]. We used the kinetic energy cut-off of 560 eV and the *k*-points of 5×5×5 were used for the integration of the reciprocal space. The projector augmented-wave (PAW) method [217] in the implementation of Kresse and Joubert [199] was used to describe the core electrons and their interactions with the valence electrons. The Hubbard correction [221] in the formulation of Dudarev *et al.* [222] was applied to improve the description of the localized 3d Mn electrons. We used the effective parameter, U_{eff} = 4.0 eV which is within the range of values reported in the literature [223, 144, 148, 79]. We also included the semi-empirical method to model the long-range interactions [218, 219]. Gaussian smearing with a width of 0.05 eV was set to improve the convergence of the Brillion zone

integrations during geometry optimizations [219]. Phonon code [244] as implemented in Materials design within MedeA software of VASP [244] as was used to evaluate the vibrational properties of the material.

3.2. $LiMn_2O_4$ spinel bulk

The spinel $LiMn_2O_4$ has a face-centered cubic crystal structure with a space group $Fd\bar{3}m$ (No. 227) [44] and a lattice constant of *a* = 8.24 Å [45, 46]. The structure consists of a cubic close-packed array of oxygen atoms occupying the 32*e* sites, where lithium and manganese atoms occupy one-eighth of the tetrahedral (8*a*) sites and one-half of the octahedral (16*d*) sites, respectively, [47].

We have used the direct $LiMn_2O_4$ spinel, rather than the partially inverse system, for the sake of simplicity. In the previous work [143], the authors simulated the bulk of $LiMn_2O_4$ using the primitive rhombohedral unit cell containing 14 atoms. Given the size of their supercell, they could model three inversion degrees, i.e. the normal, half-inverse and fully inverse spinels. The authors compared the predicted configurational energy using the 1x1x1 primitive unit cell with the ensemble average calculated for the 25% inversion degree in the 2x1x1 supercell and found them to be in good agreement.
We decided not to use the partial inversion degree found for Phy. Rev. B 2018 paper as that would involve generating and optimising all the 4222 inequivalent configurations (M) for the cubic unit cell of the spinel containing 56 atoms, followed by an analysis of the site-occupancy disorder (SOD) of the material. Finally, the calculated partial inversion degree is 30%, which suggests that approximately one in every three Li atoms have swapped their position in a tetrahedral holes with the Mn in the octahedral cavities. Our models show that the $LiMn_2O_4$ (001) and (111) surfaces containing 56 atoms, display only one exposed tetrahedral Li atom, which would make very difficult to account for the partial inversion degree at the surface level. Obviously, the partial inversion degree in the subsurface layers, if taken into account, would have had only a minor effect on the surface properties of this spinel material towards ethylene carbonate.

3.3. CUT-OFF AND *K*-POINT

The cut-off and k-point were performed with the plane-wave pseudopotential method using the VASP code. To calculate the appropriate cut-off energy of spinel $LiMn_2O_4$ (space group Fd-3m), the single point calculations were performed at different cut-off energies within the GGA-PBE [216]. The total energy for each cut-off energy was noted and the calculations were repeated until constant minimum energy was reached. The total energy against the kinetic cut-off energy was then plotted (see Figure 8 below). The graph shows almost a zero slope from the cut-off energy of 560 eV. Thus, the kinetic energy of 560 eV was chosen since we noticed that the graph shows a negligible variation of the total energy. Therefore, the cut-off energy of 560 eV corresponds to the minimum energy was used in all the bulk and surface calculations.

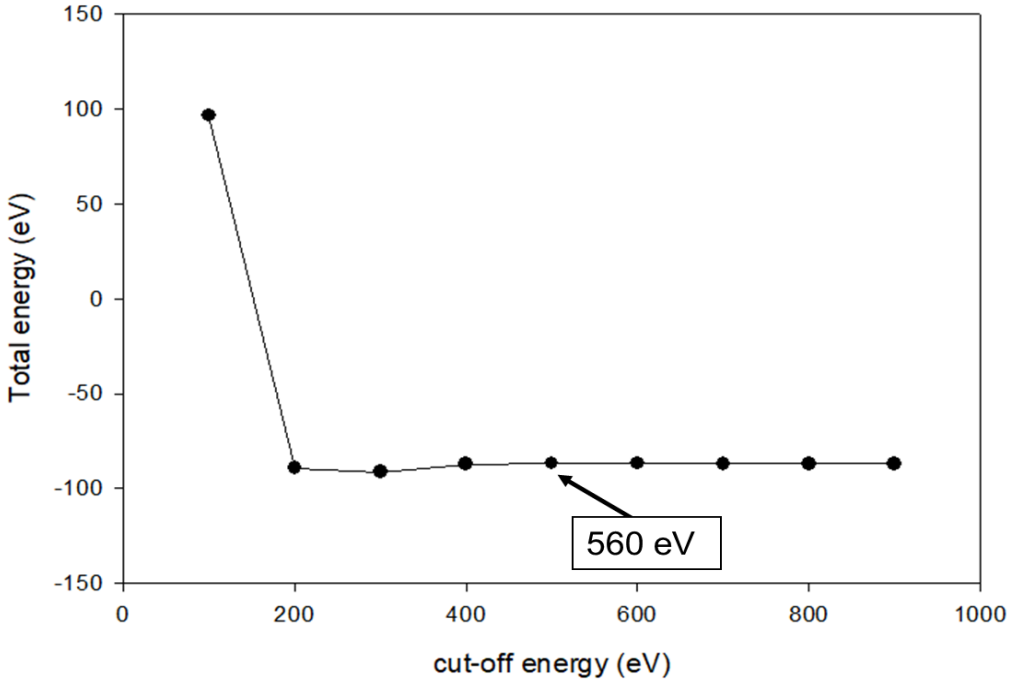

Figure 8: The plot of total energy against the kinetic cut-off for $LiMn_2O_4$ bulk structure.

The Monkhorst-Pack scheme of the *k*-points sampling was used to select an optimal set of special *k*-points of the Brillouin zone such that the greatest possible accuracy is achieved from the number of *k*-points used. Different values of *k*-points mesh parameters were varied from 1×1×1 to 9×9×9 until total energy change is negligible. The plot for

total energy against the *k*-points for the $LiMn_2O_4$ bulk structure was represented in Figure 9 below. We found the *k*-point mesh parameter to be the 5×5×5.

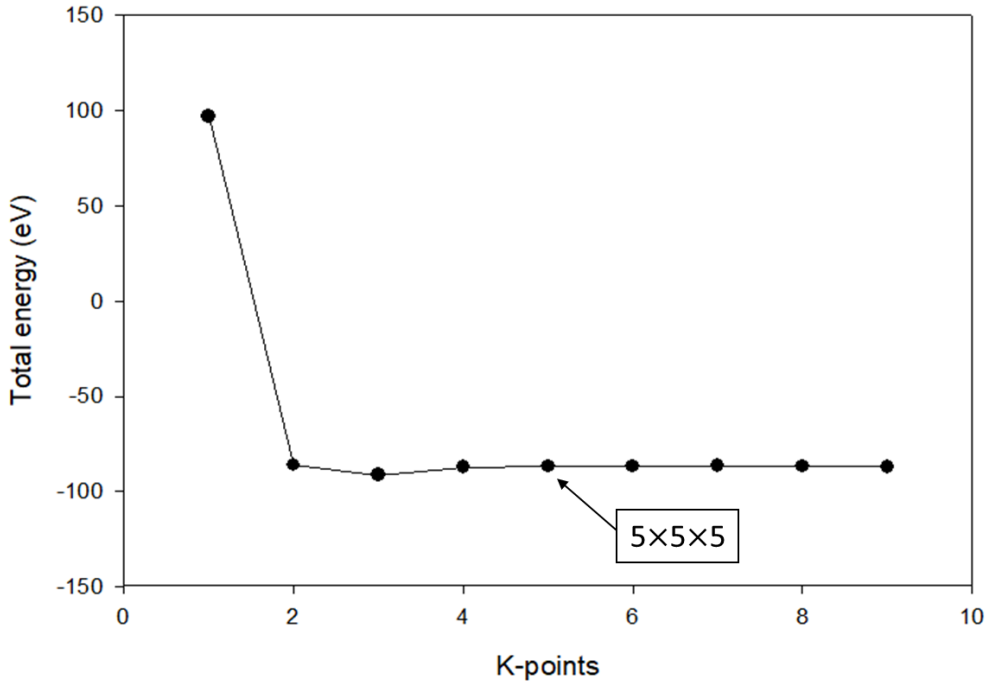

Figure 9: The plot of total energy against the *k*-points for $LiMn_2O_4$ bulk structure.

3.4. LATTICE PARAMETERS & HEATS OF FORMATION

To determine the equilibrium structural properties, we performed geometry optimization calculation within the generalized gradient approximation using cut-off energy of 560eV. Table II summarizes the lattice parameter, heats of formation, and the reference data. Lattice parameters describe the physical dimension of the unit cell in a crystal structure. Lattices in three-dimension have the lattice constants *a*, *b*, and *c*, while a full lattice parameter consists of the three lattice constants and the three angles between them. The lattice constants *a* = *b* = *c* for a cubic system. The lattice constant calculated was found to be *a* = 8.247Å, which agrees with the reported literature. Furthermore, we evaluated the heats of formation (ΔH_f) for lithium manganese oxide structure can be described by equation 3.1 below [245]:

$$\Delta H_f = \frac{1}{N}\left[\mathrm{E}_{LiMn_2O_4} - (\mathrm{E}_{Li} + 2\mathrm{E}_{Mn} + 4\mathrm{E}_{O})\right] \quad (3.1)$$

where $E_{LiMn_2O_4}$ is the total energy of the optimized pristine $LiMn_2O_4$ structures, *i*s the number of moles for each atom in the bulk, E_{Li}, E_{Mn} and E_O are the total energy of one Li, Mn, and O atoms in the body-centered cubic (*bcc*), respectively. The heat of formation calculated in this work agreed with the reported literature.

Table II: The lattice parameter, and their reported literature for the bulk $LiMn_2O_4$ structure. Heats of formation (ΔH_f) calculated by using equation 3.1.

Material	Lattice parameters *a* (Å)				Heats of formation (KJ/mol)		
	This work	Theoretical		Experimental	This work	Theoretical	
		Santos-Caballal *et al.* [143]	Karim *et al.* [148]	Ishizawa *et al*. [246]		Yamaguchi et al. [247]	Wang *et al.* [248]
$LiMn_2O_4$	8.24	8.350	8.43	8.25	-1258.56	-1404.2	-1380.9

3.5. BAND STRUCTURES AND THE DENSITY OF STATES

The band structures the density of states that were calculated to study electronic stability and arrangements of electrons within the $LiMn_2O_4$ molecule [249]. The band structures can be used to identify the band-gap and the conductivity of a material. Figure 10a indicates the band structure of the spinel bulk along with the W, L, Γ, X, and K Brillouin zone directions. From Figure 10a, around the Fermi-level a minor direct band-gap of around 0.041 eV was found to separate the conduction and the valence bands. This negligible band-gap show that the structure is a magnetic semiconductor. To further study the electronic stability and electronic arrangement, the density of states (DOS) was calculated, and the states were summarised in Figure 10b. It can be noted that there are no states observed at the Fermi (E_f), which indicates that the structure shows no metallic behavior, hence a semiconductor. Instead, a pseudo-gap was observed at the E_f which indicates that the structure electronically stable. “Pseudo” means “false, unreal or fake”, this *pseudogap* can indicate the stability of the material in density of states (DOS). Figure 10b also describes the electronic arrangement according to their respective orbitals. The lower peak of the valence band is dominated by the *s*-orbital of the Li atom, ranging

around -18 eV. The upper peaks ranging between -7.0 to -1.5 eV show hybridization between the Mn *d*-orbitals and the O *p*-orbital. At the conduction band, the peaks at around 1.0 and 3.2 eV are dominated by the *d*-orbitals of the Mn atom.

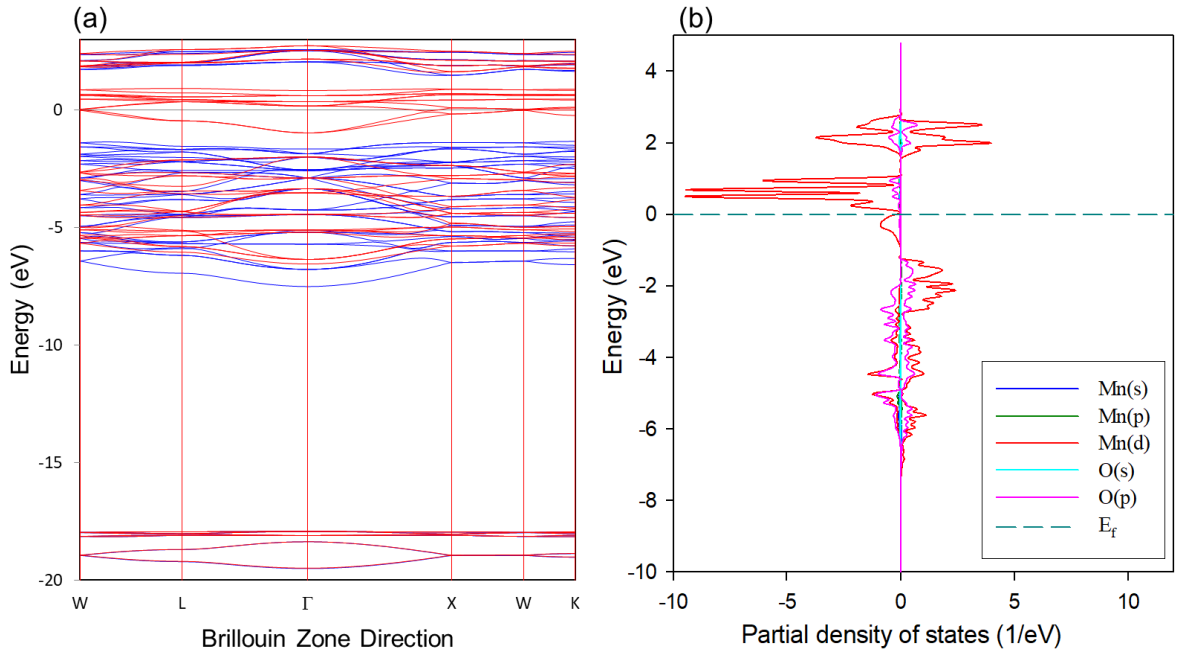

Figure 10: The calculated (a) electronic band structure and (b) the partial density of states for the $LiMn_2O_4$ spinel bulk structure.

3.6. ELASTICITY

As discussed in the method, the elasticity describes the strength of the material against external pressure. To study the elasticity of the $LiMn_2O_4$ spinel bulk, the elastic constants, moduli, anisotropy, and Pugh's ratio were calculated at the strain of 0.005 (see Table III). The elastic constants can be used to deduce the mechanical stability of the material and each structural orientation has its specific criteria. Mechanical stability criteria of a cubic system as outlined elsewhere [250] is given as follows:

$$C_{44} > 0,\ C_{11} > C_{44},\ \text{and}\ C_{11} + 2C_{12} > 0,\ C' = \tfrac{1}{2}(C_{11}-C_{12}) \qquad (3.2)$$

Where C_{11}, C_{12}, and C_{44} are the independent elastic constants. The calculated elastic constants are all positive and obey the mechanical stability criteria for cubic crystals

outline in equation 3.2, for example, $C_{11} + 2C_{12} = 263.98 > 0$. Also, the calculated tetragonal shear moduli (C') was found to be 77.06 GPa, which is positive and this indicates the stability of the material. Furthermore, we analyzed the Pugh's ratio, which is a ratio of the bulk to shear moduli which indicates the brittleness or the ductility of the material [251]. A higher value of B/G ratio indicates the ductility whereas a low value less than 1.75 indicates the brittleness of the material (If the ratio B/G > 1.75, then the material is ductile and otherwise brittle). The calculated B/G ratio was found to be 1.03, which is less than 1.75, thus the structure is brittle. Then, we calculated the anisotropy factor (A), which measures the degree of anisotropy in a solid. Anisotropic solid has a value of 1 and measures the degree of elastic anisotropy when the value is less or greater than unity [236]. The value is calculated using the following equation:

$$A = \frac{2C_{44}}{C_{11} - C_{12}} \tag{3.4}$$

The calculated anisotropy (A) shown in Table III, is greater than 1, which indicates that the bulk structures are elastically anisotropic materials.

Table III: Elastic constants (C_{ij}) bulk moduli (B), tetragonal shear moduli (C'), shear moduli (G), Young's moduli (Y), anisotropic ratio (A), and Pugh's ratio (K).

Material	Elastic Constants (GPa)		Moduli			
$LiMn_2O_4$ - normal spinel	C_{11}	190.75	*B*	88.00	*C'*	77.06
	C_{12}	36.63	*G*	85.09	*A*	2.34
	C_{44}	90.45	*Y*	193.06	*B/G*	1.03

3.7. PHONON DISPERSION

The phonon dispersion spectrum is used to draw an analogy between photon representing a quantum of electromagnetic radiation and quanta of lattice vibration [252]. To investigate the dynamic stability of the $LiMn_2O_4$ bulk structure, phonon dispersion curves were calculated in its ground state. Phonon calculations were performed based on the small displacement method within the harmonic approximation using the PHON code [226]. The Phonon dispersion curves were plotted along the W, L, Γ, X, and K

Brillouin zone directions (see Figure 11a). The curve shows no imaginary vibrations along with all directions, which suggests that the structure is dynamically stable. From the phonon dispersion curve, the acoustic band ranges between 0 and 13 eV while the optical band 15 and 18 eV. The partial phonon density states, PDOS (see Figure 11b.) indicate that the optical bands are dominated by the oxygen atoms while the acoustic band is dominated by the lithium atom and a small bandgap is observed around 14.0 and 14.5 THz.

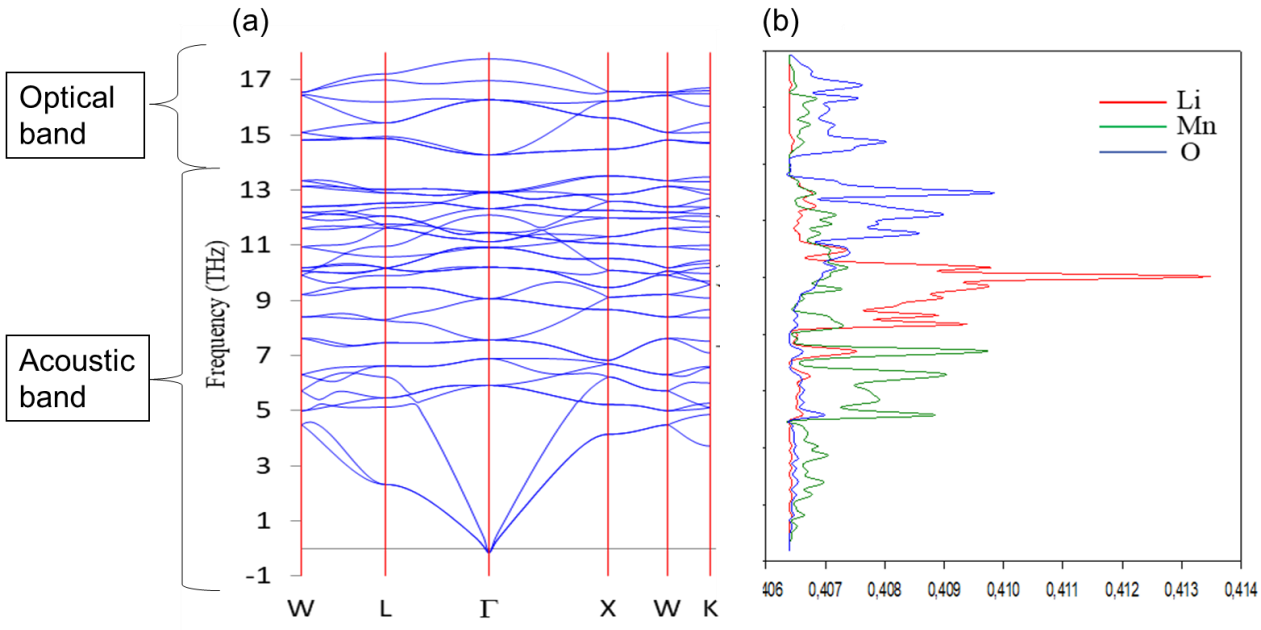

Figure 11: The plot of the (a) phonon dispersion curve and (b) partial phonon density of states (PDOS) for $LiMn_2O_4$ spinel structure.

CHAPTER SUMMARY

In this chapter, the DFT calculations were used to study the bulk properties of the normal $LiMn_2O_4$ spinel by investigating the structural properties, band structures, phonon dispersions, the density of states, and elastic constants. The $LiMn_2O_4$ spinel is a face-centered cubic structure with *a* = 8.175Å, which agrees with the reported literature. From the electronic band structures, around the Fermi-level a minor direct band-gap of around 0.041 eV was found to separate the conduction and the valence bands. This indicated that the material is a magnetic semiconductor. We also explored the density of states (DOS), which showed a psedo-gap at the Fermi-level, which indicates that the material is electronically stable. The calculated elastic constants are all positive and obey the mechanical stability criteria for cubic crystals outline. The calculated B/G ratio was found to be 1.03, which is less than 1.75, thus the structure is brittle. The calculated anisotropy (A) is greater than 1, which indicates that the bulk structures are elastically anisotropic. We finally plotted the phonon dispersion, which shows no imaginary vibrations along with all directions, which suggests that the structure is dynamically stable.

CHAPTER 4

ETHYLENE CARBONATE ADSORPTION ON THE MAJOR SURFACES OF LITHIUM MANGANESE OXIDE $LI_{1-X}MN_2O_4$ SPINEL (0.000 < X < 0.375)

The chapter has been published in the journal of physical chemistry chemical physics (PCCP).

CHAPTER SUMMARY

Understanding the surface reactivity of the commercial cathode material $LiMn_2O_4$ towards the electrolyte is important for improving the cycling performance of secondary lithium-ion batteries and preventing manganese dissolution. In this chapter, we discuss the surface stability and the surface reactivity of the three low Miller index surfaces, which are (001), (011), and (111) toward the electrolyte component ethylene carbonate (EC) during charge/discharge processes. The surface stabilities are discussed based on the effect of relaxation towards the stacking sequence, surface energies, and the effect of delithiation on the Wulff morphologies. Furthermore, a clear discussion is given based on the reactivity of the EC molecule onto the charged/discharged low Miller index surfaces. We explore its binding energies on both fully lithiated and partially delithiated surfaces, the effect of adsorption on the Wulff morphologies, and the reactivity of EC molecule looking at the charge transfers and the vibrational frequencies.

4.1. COMPUTATIONAL DETAILS

The surface spinel calculations were performed using spin-polarized density functional theory (DFT) as implemented in the Vienna *Ab-initio* Simulation Package (VASP) [215]. All calculations were carried out within the generalized gradient approximation (GGA) using the Perdew, Burke, and Ernzerhof (PBE) exchange-correlation functional [216]. The kinetic energy cut-off was fixed at 560 eV for the expansion of the Kohn-Sham (KS) valence states. A Γ-centred Monkhorst-Pack grid of 5×5×1 k-points was used for the integration in the reciprocal space of all surfaces. The core electrons and their interaction with the valence electrons were described using the projector augmented-wave (PAW)

method [217] in the implementation of Kresse and Joubert [199]. The core electrons are comprised of the levels up to the 3*s* for manganese and 1*s* for carbon and oxygen, while all the electrons are treated as valence electrons for lithium and hydrogen. The semi-empirical method of Grimme with the Becke-Johnson damping [D3-(BJ)] [218, 219] was also included in our calculations for modelling the long-range dispersion interactions, which are required to describe surfaces properly. Gaussian smearing with a width of 0.05 eV was set to improve the convergence of the Brillion zone integrations during geometry optimizations [219]. However, the tetrahedron method with Blöchl corrections were used to obtain accurate electronic and magnetic properties as well as total energies [220]. The Hubbard correction [221] in the formulation of Dudarev *et al.* [222] was applied to improve the description of the localized 3*d* Mn electrons. We used the effective parameter U_{eff} = 4.0 eV, which we developed in our study of the bulk properties of the fully lithiated $LiMn_2O_4$ [143] and is within the range of values reported in the literature [223, 144, 142, 79].

4.2. SURFACE MODELS

All the surfaces were modelled from a fully optimized bulk structure using the dipole method implemented in METADISE [253]. The resulting slabs were then represented by keeping fixed the bottom atoms at their relaxed bulk positions to simulate the bulk phase of $LiMn_2O_4$ and then relaxing the rest of the atoms. The slabs were modelled in such a way that they have the same 56 atoms as the bulk (8 formula units), with 8 lithium atoms, 16 manganese atoms, and 32 oxygen atoms. The $LiMn_2O_4$ (001), (011), and (111) surfaces were modelled from an optimized pristine bulk structure [143] and the slabs having surface areas of 64.7, 49.3 and 60.4 $Å^2$, respectively, with nine atomic layers as shown in Table IV. In every slab, the vacuum region of around 15 Å was added perpendicular to the surface to avoid interactions between the periodic slabs. The surface slabs were optimized until they reached the convergence within 1 meV per cell. We also applied dipole corrections perpendicular to the surface to perpendicular to all surfaces in the calculations to enhance the electronic convergence. All the geometry optimizations were conducted using the conjugate-gradient technique and were considered to converge when the Hellmann-Feynman forces were below 0.01eV/Å.

Table IV: Surface area ($A_{surface}$) and the number of layers (N_{layers}) for each cell composition of the fully lithiated and partially delithiated surfaces of $Li_{1-x}Mn_2O_4$.

Surface	$A_{surface}$ $(Å^2)$	N_{layers}	Cell composition		x	
			Lithiated	Delithiated	Lithiated	Delithiated
(001)	69.72	9	$Li_8Mn_{16}O_{32}$	$Li_5Mn_{16}O_{32}$	0	0.375
(011)	49.30	9	$Li_8Mn_{16}O_{32}$	$Li_5Mn_{16}O_{32}$	0	0.375
(111)	60.38	13	$Li_8Mn_{16}O_{32}$	$Li_6Mn_{16}O_{32}$	0	0.250

For each surface orientation, we modelled two terminations in such a way that they maintain the same number of formula units and several atoms as in the bulk structure (see Figure 12). The two surface terminations were constructed regarding the stacking sequences outlined in previous work [146, 150]. For the (001) and (111) surfaces, the slabs were symmetrical along the *z*-direction. The top species in the (001) were (½ ML) Li atom and two Mn and four O atoms for each termination A and B, respectively. The stacking sequence for both (001) terminations followed an alternation between the Li and Mn_4O_8. For the (111) facet, the terminations A and B were terminated by half of the Li-Mn and $(Mn)_2$ bulk layers, respectively. However, for the (011) surfaces were asymmetrical along the *z*-axis, for the top and bottom layers. The terminations A and B were terminated by half of the $LiMnO_2$ and MnO_2 bulk layers, respectively.

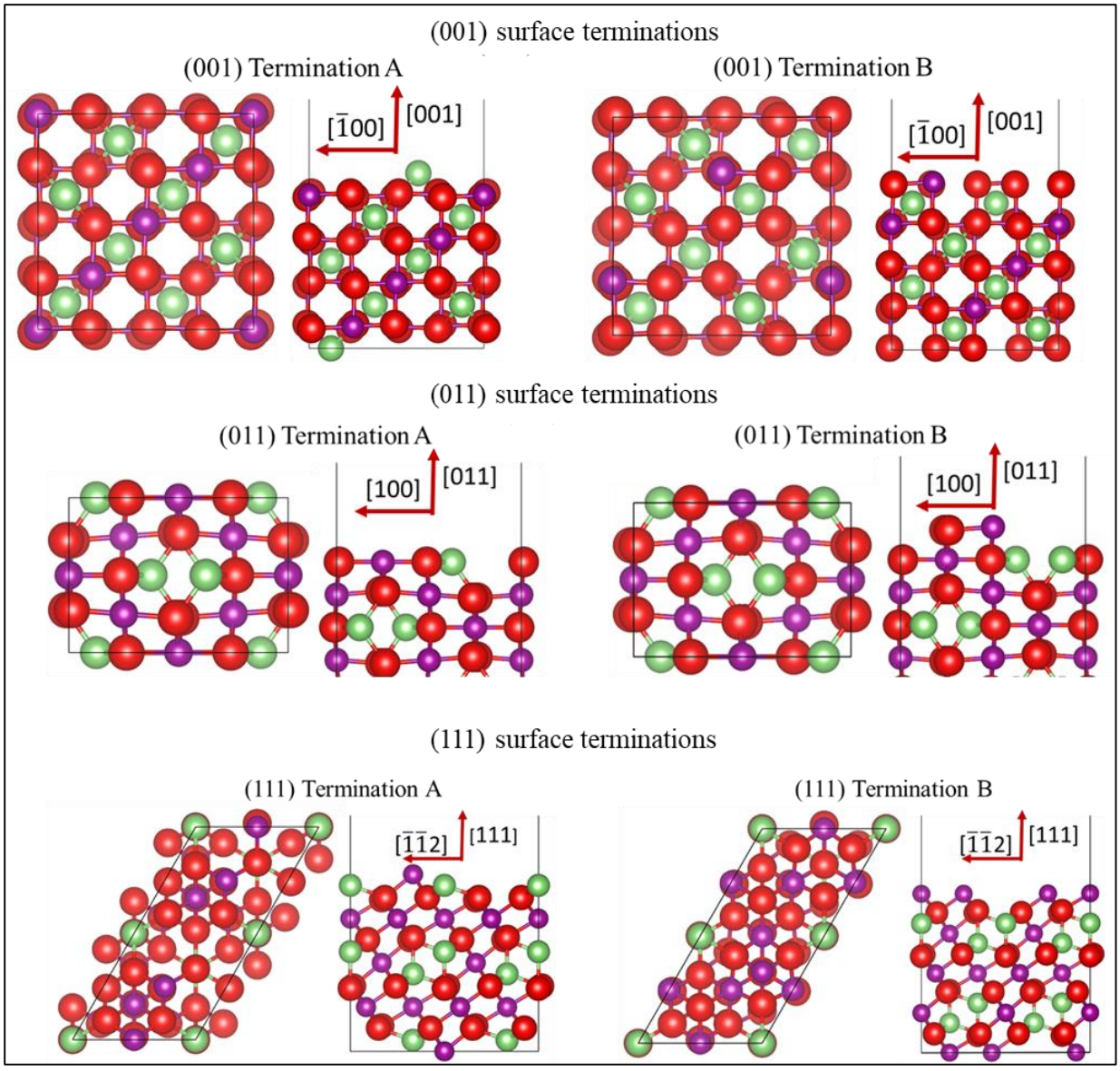

Figure 12: Top and side view of the simulation slabs for the fully lithiated $LiMn_2O_4$ spinel. Crystallographic directions for the top view of (001) surface terminations is [100] for the abscissae towards the right, for the (011) surface terminations it is [0$\bar{1}$1] for the abscissae towards the right, and the (111) surface terminations it is [0$\bar{1}$1] for the longest axis towards the top.

4.3. SURFACE ENERGIES

The surface terminations obtained from the fully optimized spinel bulk structure [143] were analyzed by calculating the surface energies for the unrelaxed and relaxed slabs, see Table V. Before and after relaxation, we observed a trend of increasing surface energies, which is (001) < (011) < (111), which is the same for the relaxed and unrelaxed facets, thus decreasing stability. The trend is established by considering the most stable surface terminations (with lowest γ). We also observe that the most stable surface is the (001) termination A with γ_r = 0.04 eV/Å^2, which is the Li-terminated $LiMn_2O_4$ surface. The lowest surface energy is in agreement with the reported literature [254, 142], and also compares well with the lowest surface energy of Mg-terminated $MgAl_2O_4$ surface [153]. Among all the surface terminations, (111) termination B had the highest geometry relaxation.

Table V: Calculated surface energies for unrelaxed (γ_u) and relaxed (γ_r) surface terminations of the (001), (011), and (111) surfaces of $LiMn_2O_4$.

Surfaces	Termination	$\boldsymbol{\gamma_u}$ (eV/Å^2)	$\boldsymbol{\gamma_r}$ (eV/Å^2)	Relaxation (%)
(001)	*A*	0.07	0.04	43.7
	B	0.15	0.11	28.7
(011)	*A*	0.10	0.05	50.0
	B	0.10	0.07	37.2
(111)	*A*	0.08	0.05	38.0
	B	0.21	0.09	57.9

4.4. ETHYLENE CARBONATE ADSORPTION ON $Li_{1-x}Mn_2O_4$

Here, we discuss the spinel surface interactions towards the ethylene carbonate electrolyte component. First, we explored the preferred adsorption geometries for different orientations of the EC molecule and various binding sites on the $Li_{1-x}Mn_2O_4$ (001), (011), and (111) surfaces. The adsorption sites investigated included the top, bottom, bridge, and hollow positions, as shown in Figure 13. The initial interaction configurations of the EC molecule included coordination to the surface via the carbonyl and ethereal oxygen, both in flat and perpendicular orientations. Before adsorption, we

measured the structural parameters of the relaxed EC molecule and compared them with the available literature data to ensure the accuracy of our results.

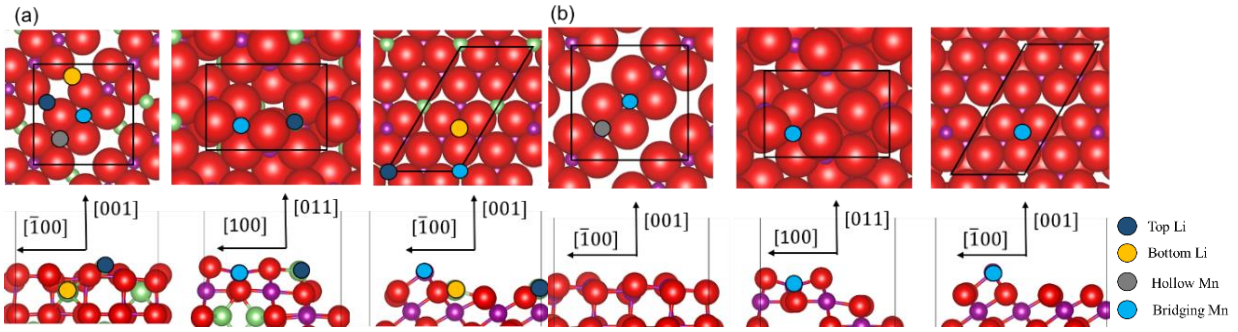

Figure 13: Top and side view for the adsorption sites of (a) lithiated $LiMn_2O_4$, (b) delithiated $Li_{1-x}Mn_2O_4$.

Table VI summarizes the equilibrium bond distances and angles, which are in good agreement with the available literature. In all our simulations, the EC molecule was placed initially at 2.5 Å from the surface to favor the attractive forces over the repulsive ones between the molecule and the surface. However, during geometry optimization, the adsorbate and the surface were free to move and allowed to change their adsorption geometry.

Table VI: Equilibrium bond distances and angles in the EC molecule calculated and compared with the literature.

Parameters	This work	Experimental **[255]**	B3PW91 **[256]**	Monte Carlo **[257]**
d(C=O)/ Å	1.20	1.20	1.15	1.20
d(C-O)/ Å	1.37	1.39	1.33	1.36
d(C-C)/ Å	1.50	1.54	1.52	1.43
d(C-H)/ Å	1.10	1.09	-	1..09
∠(O-C-O)/°	110.5	125.2	124.1	110.6
∠(C-O-C)/°	108.9	109.5	109.0	110.5

Figure 14 summarizes the most stable interactions between the spinel $Li_{1-x}Mn_2O_4$ surfaces and EC molecule, together with the relevant binding energies. First, we explored

the EC adsorption onto the fully lithiated spinel surface through the Mn atom, where our calculations indicate that the EC molecule prefers to bind to the surface through the carbonyl oxygen at a distance of 2.47 Å when placed parallel to the surface. This mode is in excellent agreement with previous work [258], where the EC molecule was found to bind strongly to the fully lithiated spinel (001) surface through the Mn atom. In our work, we also explored the EC adsorption on the (001), (011), and (111) surfaces where we found that the process releases the largest adsorption energy at the (111) facet due to the bidentate binding mode to the Li and Mn atoms. Next, we studied the EC adsorption onto the fully lithiated surfaces through the Li atom, where it strongly binds with the surfaces through the ethereal oxygen (O_e). However, upon geometry optimization, the molecule interacted with the exposed Mn and Li atoms on the (111) surface with very exothermic adsorption energy. The EC molecule preferred to interact with the (001) Li atom through the ethereal oxygen at 2.31 Å and by forming one hydrogen-bond of 2.16 Å with one surface oxygen. Moreover, the EC molecule was found to bind perpendicularly to the (011) surface at 2.00 Å via the ethereal oxygen. We also studied the EC adsorption onto the partially delithiated surfaces, where the only available adsorption sites are the exposed manganese atoms. Like the (001) lithiated surfaces, the EC molecule preferred to bind with the delithiated surfaces through the carbonyl oxygen where the strongest binding energy was calculated on the (111) facet.

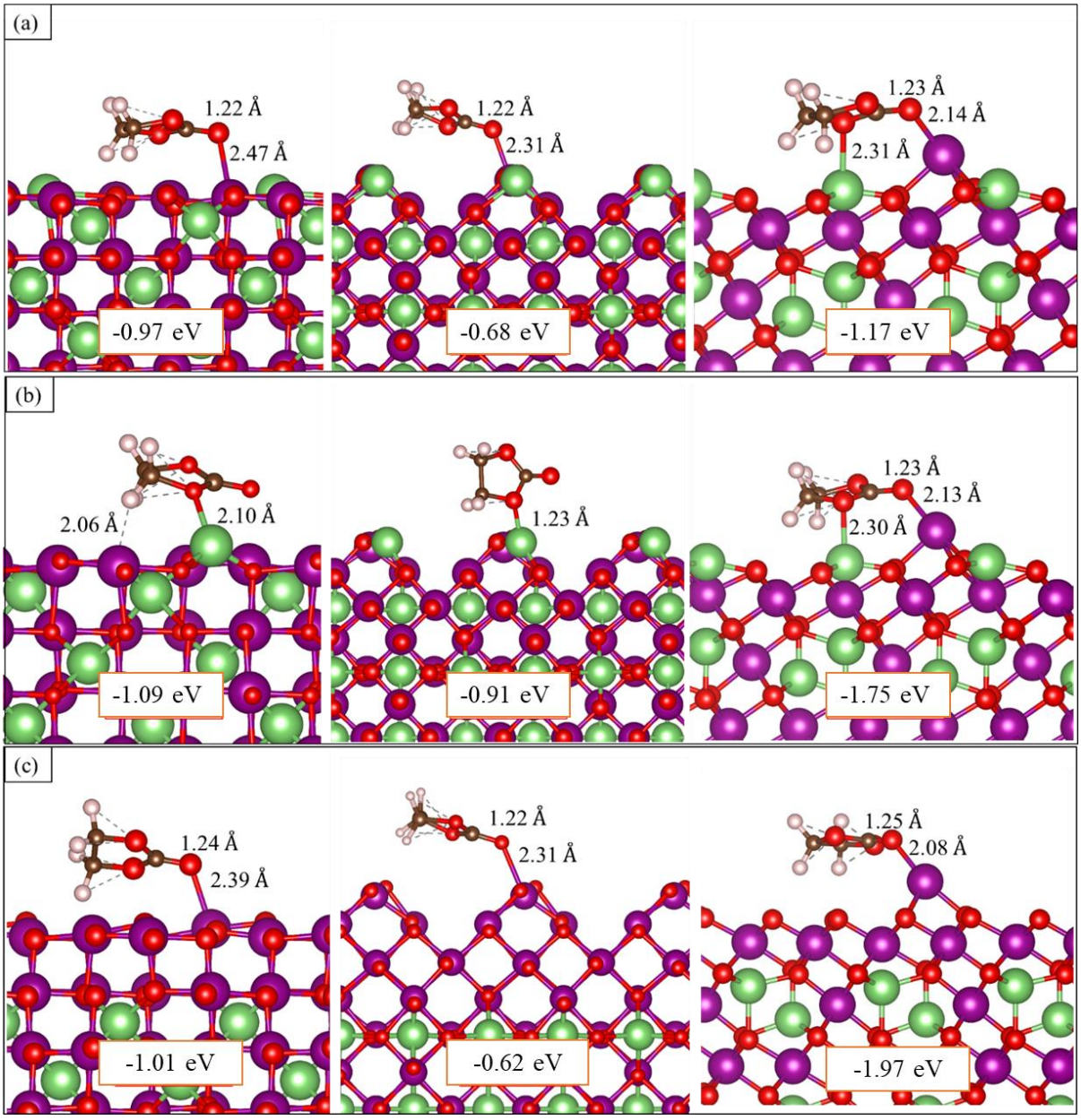

Figure 14: Most stable adsorption configurations for the EC molecule on the $Li_{1-x}Mn_2O_4$ surfaces. Adsorption sites in the fully lithiated spinel are (a) Mn atom, (b) Li atom; and in the partially delithiated surface, it is (c) Mn atom. Crystallographic directions for the top view of (001) surface terminations is [100] for the abscissae towards the right, for the (011) surface terminations it is $[0\bar{1}1]$ for the abscissae towards the right, and the (111) surface terminations it is $[0\bar{1}1]$ for the longest axis towards the top.

4.5. SURFACE FREE ENERGIES

To mimic the charge/discharge processes, we further calculated the surface free energies (σ) for the modified slabs, *i.e.* when it is partially delithiated or interacting with the EC molecule via the equation:

$$\sigma = \gamma_{\mathrm{r}} + \frac{E_M - E\mathrm{r} + (8 - N_{\mathrm{Li}})E_{\mathrm{Li}} - E_{\mathrm{EC}}}{A} \quad (4.1)$$

where E_{M} is the energy of the modified slab, $8-N_{\mathrm{Li}}$ is the number of lithium atoms removed from the slab, E_{Li} is the energy of one atom in the bulk of the body-centred cubic (*bcc*) lithium, E_{r} is the energy of the pristine slab and E_{EC} is the energy of the isolated ethylene carbonate molecule. Where there is no surface modification, the surface energies and the surface free energies have the same value, but a correction expression is added to account for surface modifications, such as adsorptions, doping, delithiation, and lithiation. Table 4 summarises the surface free energies of the fully lithiated surfaces interacting with the EC molecule, as well as the partially delithiated surfaces, both pristine and interacting with the adsorbate. The calculated surface free energies are higher as compared to the surface energies of the fully-lithiated facets. This increase in energy of the partly delithiated surfaces as compared to the fully lithiated surfaces indicates that upon delithiation, the surfaces become less stable, thus resulting in a destabilizing effect. However, the addition of the EC molecule can affect the stabilities of both the fully lithiated and partially delithiated systems. For example, when the EC molecule is adsorbed onto the (001) surface by coordinating one of the manganese atoms, an increase of 0.08 eV/$\mathrm{\AA}^2$ in the surface free energy is observed, indicating that the adsorbate has a destabilizing effect. On the other hand, we have also observed a decrease in the surface free energies for the other modified surfaces concerning the pristine planes, but it was proportionally smaller than in the (011) facet [156].

Table VII: Surface free energy (σ) for the fully lithiated and partially delithiated $Li_{1-x}Mn_2O_4$ surfaces interacting with the EC molecule.

Surface	*x*	Adsorption site	$\boldsymbol{\sigma}$ (eV/Å^2)
(001)	0	Mn	0.12
	0	Li	0.02
	0.375	−	0.13
	0.375	Mn	0.02
(011)	0	Mn	0.13
	0	Li	0.04
	0.375	−	0.13
	0.375	Mn	0.04
(111)	0	Mn	0.07
	0	Li	0.02
	0.250	−	0.11
	0.250	Mn	0.02

4.6. MORPHOLOGIES

Here, we discuss the Wulff crystal morphologies for the fully lithiated and partially delithiated $Li_{1-x}Mn_2O_4$ materials, which were obtained using the termination with the lowest surface free energy for each pristine and modified surface [259, 154]. As shown in Figure 15, the (001) plane dominates the morphologies for the fully lithiated material and the (111) surface is the major surface for the partially delithiated spinel. The (011) surface does not appear in the Wulff morphology after delithiation or adsorption of the EC

molecule, because of its higher surface free energy for the (001) and (111) planes. We have also carried out test calculations to determine the effect of different Li contents and we found similar Wulff crystal morphologies to the ones presented in Figure 17 using slabs containing the same stoichiometry. Our morphology for the delithiated material interacting with the electrolyte is in excellent agreement with the work of Kim *et al*. [156], who found that the octahedron-shaped $Li_{1-x}Mn_2O_4$ particles are dominated by the (111) surface.

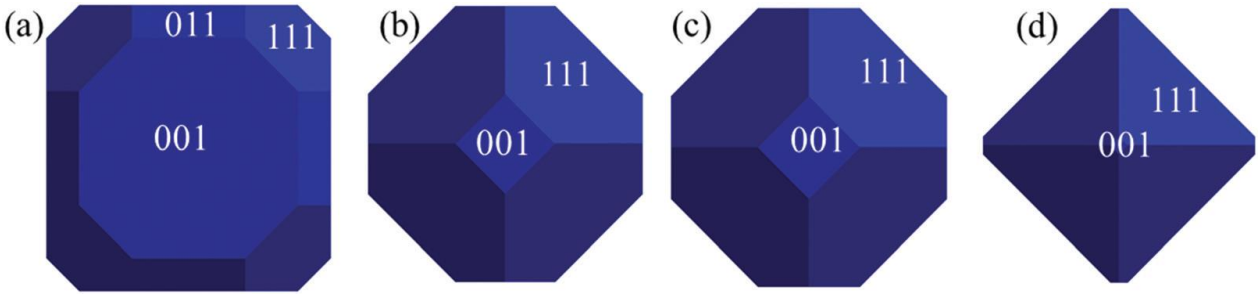

Figure 15: Surface morphologies for $Li_{1-x}Mn_2O_4$ before and after adsorption of EC on the (a) fully lithiated spinel and (b) partially delithiated material.

4.7. CHARGE TRANSFER ANALYSIS

We have carried out a Bader charge analysis to quantify the electron transfer upon adsorption of the electrolyte to the surfaces of the cathode (see Table VIII). For all the adsorbed systems, we generally observe a negligible charge transfer, which suggests that this process only plays a minor role in the adsorption mechanism. The largest charge transfer of Δq = -0.05 e^- was observed at the Li site of the (001) surface. We further explored the electronic structure by plotting the charge density difference for the adsorption configuration with the largest inter-phase charge transfer (see Figure 16). Despite the surface donating a minor charge to the electrolyte molecule, the electron flow is dominated by an internal charge rearrangement within the EC molecule. We have also compared the charge transfer between the carbonyl oxygen (O_c) and the directly bonded atoms following adsorption, by subtracting from the charge density of the total adsorbate-surface system the sum of the charge density of the isolated adsorbate and clean surface in the same geometry. We observe partial oxidation of carbon and reduction of oxygen,

owing to intramolecular electron rearrangement caused by the electron transfer from the C=O π-bond to an oxygen-surface σ-bond. In all cases, there is a transfer of ~1 electron from the carbon to the oxygen, which could lead to heterolytic cleavage of the C=O π-bond under working conditions.

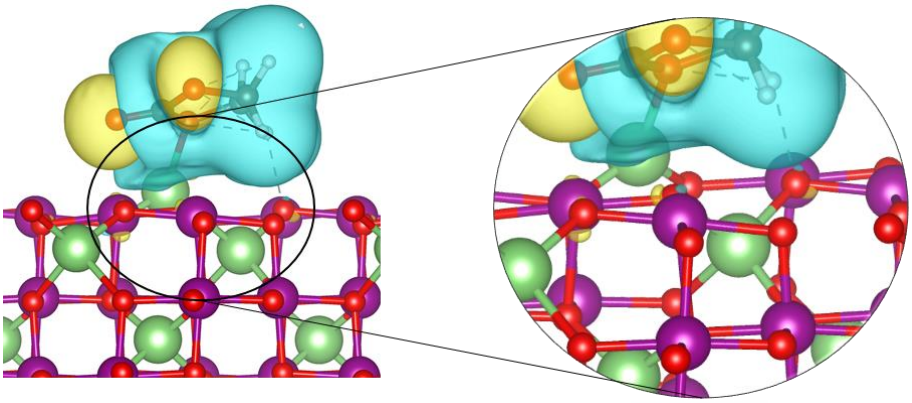

Figure 16: Charge density flow ($\Delta\rho$) for the EC molecule adsorbed on the $LiMn_2O_4$ (001) surface. The density gain and depletion are represented by yellow and blue, respectively. Isosurface display a value of 0.003 e $Å^{-3}$.

Next calculate the work function (F) for the modified surfaces, which measures the energy required to bring a surface electron to the vacuum [260]. Generally, we observe a decrease in the work function as we adsorbed the molecule, although, for the delithiated surfaces, the work function remains fairly constant. The lowest value of the work function is observed when the EC molecule is adsorbed on the pristine surfaces through the lithium (Li–O).

4.8. VIBRATIONAL FREQUENCIES

To characterize further the EC surface adsorption, we have computed the wavenumbers of the fundamental vibrational modes for the lowest-energy adsorption geometries on the (001), (011) and (111) spinel surfaces (Table VII). The quality of the vibrational modes calculated for the isolated EC molecule was assessed by comparing them with the experimental values. Our simulated vibrational modes for the isolated EC molecule compare closely with the experimental data, with the largest difference being 56 cm^{-1}. For

example, the asymmetric and symmetric υ(C-H) stretching modes for the free EC molecule were computed at 2952 and 2990 cm^{-1}, which compares well with the experimental values of 2928 and 2955 cm^{-1}, respectively. These hydrogen stretching modes are blue-shifted as a result of steric effects since the hydrogen atoms are less mobile. We also analyzed the C=O stretching modes for the adsorbed EC molecule, which were in the range of 1700 – 1900 cm^{-1} as reported by Fortunato *et al.* [261]. Although we observed a minimal charge transfer between the molecule and the surface, this does not prevent the stretching of the C=O bond. Our simulations indicate that the vibrational modes are red-shifted for the isolated EC molecule, suggesting that the internal bonds in the adsorbate weaken upon adsorption onto the spinel surfaces. This phenomenon was also observed in the charge transfers, where the carbonyl oxygen gains electron density from the carbon atom, which further weakens the C=O bond.

Table VIII. Charge transfer between the surface and EC molecule (Δq_{EC}) as well as within the carbonyl group, C=O($\Delta q_{C=O}$), and work function for the surfaces before (ϕ_p) and after (ϕ_a) adsorption. The vibrational wavenumbers are also included to describe the symmetric stretching (ν_{sym}), asymmetric stretching (ν_{asym}), and bending (δ) modes.

							CH_2 vibrations			C=O
Surface	Adsorption site	x	Δq_{EC} (e^-)	$\Delta q_{Oc/Oe}$ (e^-)	Φ_p (eV)	Φ_a (eV)	υ_{sym} (cm^{-1})	υ_{asy} (cm^{-1})	δ (cm^{-1})	υ (cm^{-1})
Isolated EC				0.00			2952	2990	1341	1829
EC (liquid films) **[178]**							2928	2955	1397	1803
(001)	Mn	0	-0.02	0.81(O_c)	4.53	3.45	2994	2917	1489	1733
	Li	0	-0.05	0.07 (O_e)	4.53	3.16	2968	3043	1456	1770
	Mn	0.375	0.02	0.83(O_c)	3.34	3.56	3028	3079	1465	1747
(011)	Mn	0	0.00	0.80(O_c)	4.74	4.45	3021	3048	1477	1740
	Li	0	-0.01	0.03 (O_e)	4.74	4.26	3024	3089	1479	1787
	Mn	0.375	0.02	0.81(O_c)	3.82	3.82	2998	3084	1479	1736
(111)	Li, Mn	0	0.00	0.78(O_c)	3.66	3.55	2978	3007	1476	1705
	Li, Mn	0	0.02	0.08 (O_e)	3.66	3.57	3012	3065	1473	1720
	Mn	0.250	0.04	0.78(O_c)	3.62	3.62	3001	3034	1443	1659

CHAPTER SUMMARY

DFT+U-D3 simulations have been performed to study the adsorption of the ethylene carbonate molecule on the fully lithiated and partially delithiated $Li_{1-x}Mn_2O_4$ spinel surfaces. The lithium-terminated (001) surface was found to be the most stable facet, which agrees with the reported literature. We further investigated the partially delithiated surfaces, where we observed a larger surface free energy with respect to the fully lithiated surface, indicating the destabilizing effect of delithiation. We observed the strongest adsorption of the EC on the (111) surface, which was attributed to the EC molecule interacting with both the manganese and lithium atoms in the surface. The surface free energy was found to decrease following interaction with the adsorbate, which thus stabilizes the material. The Wulff morphologies show that EC adsorption enhances the expression of the (111) facet. Negligible charge transfer was observed between the adsorbate and surfaces, and the charge density flow shows a strong electronic rearrangement within the EC molecule. The electron density on the carbonyl oxygen is increased, due to partial carbon oxidation and oxygen reduction, i.e. an intramolecular electron rearrangement from the C=O π-bond to an oxygen-surface σ-bond. The vibrational frequencies also showed a red-shift in the C=O stretching mode of the adsorbed EC with respect to the isolated molecule, which suggests the weakening of the C=O bond. Our simulations show the essential role of the EC molecule in reducing the surface free energy, but future work is required to understand the kinetics and thermodynamics of its decomposition.

CHAPTER FIVE

CONCLUSION AND RECOMMENDATIONS

5.1. CONCLUSION

The density functional theory (DFT) calculations were performed to study the reactivity of the three low Miller index surfaces which are (001), (011), and (111), towards the electrolyte component ethylene carbonate (EC).

We first calculated the bulk properties of the $LiMn_2O_4$ spinel by investigating the structural properties, band structures, phonon dispersions, the density of states, and elastic constants. The $LiMn_2O_4$ spinel is a face-centered cubic structure with a = 8.175Å, which agrees with the reported literature. From the electronic band structures, around the Fermi-level a minor direct band-gap of around 0.041 eV was found to separate the conduction and the valence bands. This indicated that the material is a magnetic semiconductor. We also explored the density of states (DOS), which showed a psedo-gap at the Fermi-level, which indicates that the material is electronically stable. The calculated elastic constants are all positive and obey the mechanical stability criteria for cubic crystals outline. The calculated B/G ratio was found to be 1.03, which is less than 1.75, thus the structure is brittle. The calculated anisotropy (A) is greater than 1, which indicates that the bulk structures are elastically anisotropic. We finally plotted the phonon dispersion, which shows no imaginary vibrations along with all directions, which suggests that the structure is dynamically stable.

We then investigated the surface properties and their interactions with the EC molecule. Li-terminated (001) surface was found to be the most stable facet, which agrees with the reported literature. We further investigated the surface free energies for delithiated and adsorbed surfaces, we observed an increase in energy as we removed the lithium atoms from the top atomic layers, which indicates that the surfaces destabilize upon delithiation. We observed stronger adsorption on the (111) surface, which was attributed by the EC molecule interacting with both the manganese and lithium atoms on the surface.

However, the adsorbed surfaces, the surface free energy turns to decrease for the naked surfaces, which suggests that the EC molecule also stabilizes the cathode material during the charge/discharge process. The Wulff morphologies show that EC adsorption enhances the expression of the (111) facet, which indicates the dominance of the (111) facet upon surface adsorption. The charge transfer found between the interacting atoms was negligible, and the charge density flow indicates a strong electronic rearrangement within the EC molecule. We also analyzed the charge transfer on the carbonyl group (C=O), and we found that there is re-hybridization which results in a minor charge transfer between the surface and the molecule. Lastly, we observed a red-shift on the C=O stretching mode of the adsorbed EC for the isolated molecule, which suggests the weakening of the internal bond.

5.2. RECOMMENDATIONS

Having studied the $LiMn_2O_4$ spinel bulk structure, surfaces, and the surface interaction with the electrolyte content ethylene carbonate. We propose to study the $LiMn_2O_4$ surface coating, mainly focusing on the oxides and fluorides. Since the Cho *et al.* [262] demonstrated that the Al_2O_3-coated $LiCoO_2$ improves the capacity retention of Li-ion batteries. Various subsequent studies [80, 138, 263] also shown that coating Al_2O_3 improves the electrochemical performance and capacity retention. Many other oxides were then investigated as a coating material for Li-ion batteries, which includes the ZnO_2, TiO_2, MgO, etc. [264, 265, 266]. However, Al_2O_3 attracted the most attention since they could scavenge the HF which is continuously produced by the degradation of the common $LiPF_6$ electrolyte. Myung *et al.* [267] later demonstrated that the Al_2O_3 coating reacts with the HF to form AlF_3 and water, via the reaction: $Al_2O_3 + 6HF \rightarrow 2AlF_3 + 3H_2O$. The additional fluoride layer further provides additional protection, forming a permanent physical barrier [104].

Tu *et al*. [268] also performed experimental work and investigated the stability of $LiMn_2O_4$ by surface modification with melting impregnation method. The x-ray diffraction, fine emission scanning electron microscope (FESEM) and transmission electron microscope (TEM) indicated the distribution of Al_2O_3 around the spinel, but the X-ray absorption fine

structure analyses (XAFS) further demonstrated that Al atoms were doped onto the surface of the spinel particles.

However, Chen *et al*. [269] later carried out a computational study to investigate the mechanism for Al_2O_3 atomic layer decomposition on $LiMn_2O_4$. They demonstrated that the Al_2O_3 coat the $LiMn_2O_4$ spinel and the Al heteroatom of the triethylaluminium (TMA) precursor also dope with to the interstitial sites on the spinel surface, thus reducing the oxidation state of near-surface Mn ions. However, Waller *et al*. [270] found that the Transmission Electron Microscopy (TEM) and the X-ray Photoelectron Spectroscopy (XPS) show the presence of Mn diffusion into the ALD coating after cycling. Thus, further understanding of the interaction between the Al_2O_3 coating and the spinel surfaces is still needed. After all the studies carried out on spinel surface coating with Al_2O_3, the understanding of the interactions between the surface and the Al_2O_3 coating material is still lacking.

REFERENCES

[1] P.A. Aparicio, J.A. Dawson, M.S. Islam and N.H. De Leeuw, *Journal of Physical Chemistry C,* vol. 122, no. 45, pp. 25829 - 25836, 2018.

[2] L. Wang, Y. Lu, J. Liu, M. Xu, J. Cheng, D. Zhang, and J.B. Goodenough, *Angewandte chemie international edition,* vol. 125, no. 7, pp. 2018 - 2021, 2013.

[3] L. Xu, H. Li, X. Wu, M. Shao, S. Liu, B. Wang, G. Zhao, P. Sheng, X. Chen, Y. Han and Y. Cao, *Electrochemistry Communications,* vol. 98, pp. 79 - 81, 2019.

[4] X. Tian, X. Zhao, Y.Q. Su, L. Wang, H. Wang, D. Dang, B. Chi, H. Liu, E.J. Hensen, X.W.D. Lou and B.Y. Xia, "Engineering bunched Pt-Ni alloy nanocages for efficient oxygen reduction in practical fuel cells," *Science,* vol. 366, no. 6467, pp. 850 - 856, 2019.

[5] P. Byeon, H.B. Bae, H.S. Chung, S.G. Lee, J.G. Kim, H.J. Lee, J.W. Choi and S.Y. Chung, *Advanced Functional Materials,* vol. 28, no. 45, p. 1804564, 2018.

[6] K. Ozawa, *Solid State Ionics,* vol. 69, no. 3 - 4, pp. 212 - 221, 1994.

[7] D.W. Han, S.J. Lim, Y.I Kim, S.H. Kang, Y.C. Lee and Y.M. Kang, *Chemistry of Materials,* vol. 26, no. 12, pp. 3644 - 3650, 2014.

[8] W. Tang, Y. Hou, F. Wang, L. Liu, Y. Wu and K. Zhu, *Nano letters,* vol. 13, no. 5, pp. 2036 - 2040, 2013.

[9] C.Y. Ouyang, S.Q. Shi, Z.X. Wang, H. Li, X.J Huang and L.Q. Chen, *Europhysics Letters,* vol. 67, no. 1, p. 28, 2004.

[10] R.S. Ledwaba, M.G. Matshaba and P.E. Ngoepe, *IOP Conference Series: Materials Science and Engineering,* vol. 80, no. 1, pp. 012024-1 - 012024-5, 2015.

[11] T. Mueller, G. Hautier, A. Jain and G. Ceder, *Chemistry of materials,* vol. 23, no. 17, pp. 3854 - 3862, 2011.

[12] D.A. Cogswell and M.Z. Bazant, "Size-dependent phase morphologies in LiFePO4 battery particles," *Electrochemistry Communications,* vol. 95, pp. 33 - 37, 2018.

[13] C. Gong, Z. Xue, S. Wen, Y. Ye and X. Xie, "Advanced carbon materials/olivine LiFePO4 composites cathode for lithium ion batteries," *Journal of Power Sources,* vol. 318, pp. 93 - 112, 2016.

[14] D. Wong, B. Shrestha, D.A. Wetz and J.M. Heinzel, “Impact of high rate discharge on the aging of lithium nickel cobalt aluminum oxide batteries,” *Journal of Power Sources,* vol. 280, pp. 363 - 372, 2015.

[15] C.H. Chen, J. Liu, M.E. Stoll, G. Henriksen, D.R. Vissers and K. Amine, “Aluminum-doped lithium nickel cobalt oxide electrodes for high-power lithium-ion batteries,” *Journal of Power Sources,* vol. 128, no. 2, pp. 278 - 285, 2004.

[16] S.U. Muzayanha, C.S. Yudha, A. Nur, H. Widiyandari, H. Haerudin, H. Nilasary, F. Fathoni and A. Purwanto, “A Fast Metals Recovery Method for the Synthesis of Lithium Nickel Cobalt Aluminum Oxide Material from Cathode Waste,” *Metals,* vol. 9, no. 5, p. 615, 2019.

[17] D. Andre, S.J. Kim, P. Lamp, S.F. Lux, F. Maglia, O. Paschos and B. Stiaszny, *Journal of Materials Chemistry A,* vol. 3, no. 13, pp. 6709 - 6732, 2015.

[18] J. Kim and A. Marnthiram, *Nature,* vol. 390, no. 6657, pp. 265 - 267, 1997.

[19] S.T. Lee, K. Raveendranath, R.M. Tomy, N.A. George, S. Jayalekshmi and J. Ravi, *Journal of Physics D: Applied Physics,* vol. 40, no. 12, pp. 3807 - 3810, 2007.

[20] N. Bensalah and H. Dawood, *Journal of Material Science & Engineering,* vol. 5, no. 4, pp. 1 - 21, 2016.

[21] Y.Y. Xia, T. Sakai, T. Fujieda, X.Q. Yang, X. Sun, Z.F. Ma, J. McBreen and M. Yoshio,, *Journal of The Electrochemical Society,* vol. 148, no. 7, pp. A723 - A729, 2001.

[22] M. Wohlfahrt-Mehrens, C. Vogler and J. Garche, *Journal of power sources,* vol. 127, no. 1 - 2, pp. 58 - 64, 2004.

[23] K.L. Bassett, R.E. Warburton, S. Deshpande, T.T. Fister, K. Ta, J.L. Esbenshade, A. Kinaci, M.K. Chan, K.M. Wiaderek, K.W. Chapman and J.P. Greeley, “Operando Observations and First-Principles Calculations of Reduced Lithium Insertion in Au-Coated LiMn2O4,” *Advanced Materials Interfaces,* vol. 6, no. 4, p. 1801923, 2019.

[24] M. Michalska, D.A. Ziółkowska, J.B. Jasiński, P.-H. Lee, P. Ławniczak, B. Andrzejewski, A. Ostrowski, W. Bednarski, S.H. Wu and J.Y. Lin, “Improved electrochemical performance of LiMn2O4 cathode material by Ce doping,” *Electrochimica Acta,* vol. 276, pp. 37 - 46, 2018.

[25] A. M. Kannan and A. Manthiram, “Surface/Chemically Modified LiMn2 O 4 Cathodes for Lithium-Ion Batteries,” *Electrochemical and Solid-State Letters,* vol. 5, no. 7, pp. 167 - 169, 2002.

[26] S. Brox, S. Röser, T. Husch, S. Hildebrand, O. Fromm, M. Korth, M. Winter and I. Cekic-Laskovic, "Alternative Single-Solvent Electrolytes Based on Cyanoesters for Safer Lithium-Ion Batteries," *ChemSusChem,* vol. 9, no. 13, pp. 1704 - 1711, 2016.

[27] H.Q. Gao, Z.A. Zhang, Y.Q. Lai, J. Li and Y.X. Liu, "Structure characterization and electrochemical properties of new lithium salt LiODFB for electrolyte of lithium ion batteries," *Journal of Central South University of Technology,* vol. 15, no. 6, pp. 830 - 834, 2008.

[28] S. Hwang, D.H. Kim, J.H. Shin, J.E. Jang, K.H. Ahn, C. Lee and H. Lee, "Ionic Conduction and Solution Structure in LiPF6 and LiBF4 Propylene Carbonate Electrolytes," *The Journal of Physical Chemistry C,* vol. 122, no. 34, pp. 19438 - 19446, 2018.

[29] D. Guan, J.A. Jeevarajan and Y. Wang, "Enhanced cycleability of LiMn2O4 cathodes by atomic layer deposition of nanosized-thin Al2O3 coatings," *Nanoscale,* vol. 3, no. 4, pp. 1465 - 1469, 2011.

[30] S. Hao and C. Wolverton, "Lithium transport in amorphous Al2O3 and AlF3 for discovery of battery coatings," *The Journal of Physical Chemistry C,* vol. 117, no. 16, pp. 8009 - 8013, 2013.

[31] S.C. Park, Y.M. Kim, Y.M. Kang, K.T. Kim, P.S. Lee and J.Y. Lee, "Improvement of the rate capability of LiMn2O4 by surface coating with LiCoO2," *Journal of power sources,* vol. 103, no. 1, pp. 86 - 92, 2001.

[32] S. L. a. J. Cho, "PVP-Assisted ZrO2 coating on LiMn2O4 spinel cathode nanoparticles prepared by MnO2 nanowire templates," *Electrochemistry Communications,* vol. 10, no. 10, pp. 1478 - 1481, 2008.

[33] M. Aykol, S. Kirklin and C. Wolverton, *Advanced Energy Materials,* vol. 4, no. 17, p. 1400690, 2014.

[34] D. Guyomard and J.M. Tarascon, *Journal of The Electrochemical Society,* vol. 139, no. 4, pp. 937 - 948, 1992.

[35] S.I. Tobishima and T. Okada, *Electrochimica acta,* vol. 30, no. 12, pp. 1715 - 1722, 1985.

[36] Y. Hu, W. Kong, H. Li, X. Huang and L. Chen, *Electrochemistry communications,* vol. 6, no. 2, pp. 126 - 131, 2004.

[37] M. Fujimoto, Y. Shouji, T. Nohma and K. Nishio, *Denki Kagaku,* vol. 65, pp. 949 - 953, 1997.

[38] J.T. Lee, Y.W. Lin and Y.S. Jan, *Journal of Power sources,* vol. 132, no. 1 - 2, pp. 244 - 248, 2004.

[39] L. Xing, W. Li, C. Wang, F. Gu, M. Xu, C. Tan and J. Yi, *Journal of Physical Chemistry B,* vol. 113, no. 52, pp. 16596 - 16602, 2009.

[40] J.C. Soetens, C. Millot and B. Maigret, *Journal of Physical Chemistry A,* vol. 102, no. 7, pp. 1055 - 1061, 1998.

[41] W. Van Schalkwijk and B. Scrosati, Advances in lithium ion batteries introduction, Boston, MA: Springer, 2002, pp. 1 - 5 .

[42] Chernyak, Y., *Journal of Chemical & Engineering Data,* vol. 51, no. 2, pp. 416 - 418, 2006.

[43] R. Payne and I.E. Theodorou, *Journal of Physical Chemistry,* vol. 76, no. 20, pp. 2892 - 2900, 1972.

[44] R.J. Hill, J.R. Craig and G.V. Gibbs, "Systematics of the spinel structure type," *Physics and chemistry of minerals,* vol. 4, no. 4, pp. 317 - 339, 1979.

[45] S. Chitra, P. Kalyani, T. Mohan, M. Massot, S. Ziolkiewicz, R. Gangandharan, M. Eddrief and C. Julien, "Physical Properties of LiMn204 Spinel Prepared at Moderate Temperature," *Ionics,* vol. 4, no. 1 - 2, pp. 8 - 15, 1998.

[46] P. Strobel, G. Rousse, A. Ibarra-Palos and C. Masquelier, "Disproportionation of stoichiometric LiMn2O4 on annealing in oxygen," *Journal of Solid State Chemistry,* vol. 177, no. 1, pp. 1 - 5, 2004.

[47] S. K. Mishra and G. Ceder, "Structural stability of lithium manganese oxides," *Physical Review B,* vol. 59, no. 9, pp. 6120 - 6130, 1999.

[48] H. Wang, L.F. Cui, Y. Yang, H.S. Casalongue, J.T. Robinson, Y. Liang, Y. Cui and H. Dai, "Mn3O4-graphene hybrid as a high-capacity anode material for lithium ion batteries," *Journal of the American Chemical Society,* vol. 132, no. 40, pp. 13978 - 13980, 2010.

[49] Y. Wang, Z. Feng, S.Z. Yang, C. Gagnon, V. Gariépy, D. Laul, W. Zhu, R. Veillette, M.L. Trudeau, A Guerfi and K. Zaghib, "Layered oxides-LiNi 1/3 Co 1/3 Mn 1/3 O 2 as anode electrode for symmetric rechargeable lithium-ion batteries," *Journal of Power Sources,* vol. 378, pp. 516 - 521, 2018.

[50] D. Wieboldt, I. Ruff and M. Hahn, "Techniques for Raman Analysis of Lithium-Ion Batteries," *Solutions For Materials Analysis,* vol. 30, no. 6, 2015.

[51] D. Deng, "Li-ion batteries: basics, progress, and challenges," *Energy Science \& Engineering,* vol. 3, no. 5, pp. 385 - 418, 2015.

[52] Thackeray, M.M., David, W.I.F., Bruce, P.G. and Goodenough, J.B. , "Lithium insertion into manganese spinels," *Materials Research Bulletin,* vol. 18, no. 4, pp. 461 - 472, 1983.

[53] R.M. Dell, “Batteries: fifty years of materials development,” *Solid State Ionics,* vol. 134, no. 1 - 2, pp. 139 - 158, 2000.

[54] H. Xia, H., Luo, Z. and Xie, J., “Nanostructured LiMn2O4 and their composites as high-performance cathodes for lithium-ion batteries,” *Progress in Natural Science: Materials International,* vol. 22, no. 6, pp. 572 - 584, 2012.

[55] D.G. Kellerman and V.S. Gorshkov, “Structure, Properties, and Application of Lithium–Manganese Spinels., 37(12), pp.1227-1236.,” *Russian journal of electrochemistry,* vol. 37, no. 12, pp. 1227 - 1236, 2001.

[56] D.H. Jang and S.M. Oh, “Electrolyte Effects on Spinel Dissolution and Cathodic Capacity Losses in 4 V Li/Li x Mn2 O 4 Rechargeable Cells,” *Journal of The Electrochemical Society,* vol. 144, no. 10, pp. 3342 - 3348, 1997.

[57] J.C. Hunter, “Preparation of a new crystal form of manganese dioxide: λ-MnO2,” *Journal of Solid State Chemistry,* vol. 39, no. 2, pp. 142 - 147, 1981.

[58] Y. Dai, L. Cai and R.E. White, “Capacity fade model for spinel LiMn2O4 electrode,” *Journal of The Electrochemical Society,* vol. 160, no. 1, p. A182, 2012.

[59] R.J. Gummow, A. De Kock and M.M. Thackeray, “Improved capacity retention in rechargeable 4 V lithium/lithium manganese oxide (spinel) cells,” *Solid State Ionics,* vol. 69, pp. 59 - 67, 1994.

[60] Thackeray, M.M., Shao-Horn, Y., Kahaian, A.J., Kepler, K.D., Skinner, E., Vaughey, J.T. and Hackney, S.A.,, “Structural Fatigue in Spinel Electrodes in High Voltage (4 V) Li/Li x Mn2 O 4 Cells,” *Electrochemical and Solid State Letters,* vol. 1, no. 1, pp. 7 - 9, 1998.

[61] S. L. a. J. Cho, “PVP-Assisted ZrO2 coating on LiMn2O4 spinel cathode nanoparticles prepared by MnO2 nanowire templates,” *Electrochemistry Communications,* vol. 10, no. 10, pp. 1478 - 1481, 2008.

[62] A. Tron, Y.D. Park and J. Mun, “AlF3-coated LiMn2O4 as cathode material for aqueous rechargeable lithium battery with improved cycling stability,” *Journal of Power Sources,* vol. 325, pp. 360 - 364, 2016.

[63] J.G. Li, X.M. He and R.S. Zhao, “Electrochemical performance of SrF2-coated LiMn2O4 cathode material for Li-ion batteries,” *Transactions of Nonferrous Metals Society of China,* vol. 17, no. 6, pp. 1324 - 1327, 2007.

[64] Q. Chena, Y. Wanga, T. Zhang, W. Yina, J. Yang and X. Wang, “Electrochemical performance of LaF3-coated LiMn2O4 cathode materials for lithium ion batteries,” *Electrochimica Acta,* vol. 83, pp. 65 - 72, 2012.

[65] C. Qing, Y. Bai, J. Yang and W. Zhang, “Enhanced cycling stability of LiMn2O4 cathode by amorphous FePO4 coating,” *Electrochimica Acta,* vol. 56, pp. 6612 - 6618, 2011.

[66] P. Mohan and G.P. Kalaignan, “Structure and electrochemical performance of surface modified LaPO4 coated LiMn2O4 cathode materials for reachargeable lithium batteries,” *Ceramics International,* vol. 40, pp. 1415 - 1421, 2014.

[67] S. Zhoa, Y. Bai, L. Ding, B. Wang and W. Zhang, “Enhanced cycling stability and thermal stability of YPO4 -coated LiMn2O4 cathode materials for lithium ion batteries,” *Solid state Ionics,* vol. 247, no. 248, pp. 22 - 29, 2013.

[68] J. Tu, X.B. Zhao, J. Xie, G.S. Cao, D.G. Zhuang, T.J. Zhu and J.P. Tu, “Enhanced low voltage cycling stability of LiMn2O4 cathode by ZnO coating for lithium ion batteries,” *Journal of Alloys and Compounds,* vol. 432, p. 313–317, 2007.

[69] X. Liu, J. Wang, J. Zhang, S. Yang, “Sol–gel-template synthesis of ZnO nanotubes and its coaxial nanocomposites of LiMn2O4/ZnO,” *Materials Science and Engineering A ,* vol. 430, p. 248–253, 2006.

[70] S. Aziz, J. Zhao, C. Cain and Y. Wang, “Nanoarchitectured LiMn2O4/Graphene/ZnO Composites as Electrodes for Lithium Ion Batteries,” *Journal of Materials Science & Technology,* vol. 30, no. 5, pp. 427- 433, 2014.

[71] J. Zhao and Y. Wang, “Atomic layer deposition of epitaxial ZrO2 coating on LiMn2O4 nanoparticles for high-rate lithium ion batteries at elevated temperature,” *Nano Energy,* vol. 2, no. 5, pp. 882 - 889, 2013.

[72] J.S. Gnanaraj, V.G. Pol, A. Gedanken and D. Aurbach, “Improving the high-temperature performance of LiMn2O4 spinel electrodes by coating the active mass with MgO via a sonochemical method,” *Electrochemistry Communications ,* vol. 5, p. 940–945, 2003.

[73] S. Lim and J. Cho, “PVP-functionalized nanometre scale metal oxide coatings for cathode materials: successful application to LiMn2O4 spinel nanoparticles,” *Chemical Communication,* pp. 4472 - 4474, 2008.

[74] S.T. Myung, K. Izumi, S. Komaba, Y.K. Sun, H. Yashiro and N. Kumagai, “Role of alumina coating on Li- Ni- Co- Mn- O particles as positive electrode material for lithium-ion batteries,” *Chemistry of Materials,* vol. 17, no. 14, pp. 3695 - 3704, 2005.

[75] J.L. Quan, B.T. Teng, X.D. Wen, Y. Zhao, R. Liu and M.F. Luo, "Hydrogen fluoride adsorption and reaction on the α-Al2O3(0001) surface: A density functional theory study," *The Journal of chemical physics,* vol. 136, no. 11, p. 114701, 012.

[76] M. Casarin, D. Falcomer, A. Glisenti and A. Vittadini, "Experimental and Theoretical Study of the Interaction of CO2 with α-Al2O3," *Inorganic chemistry,* vol. 42, no. 2, pp. 436 - 445, 2003.

[77] M.A. Barteau, "Site requirements of reactions on oxide surfaces," *Journal of Vacuum Science & Technology A: Vacuum, Surfaces, and Films,* vol. 11, no. 4, pp. 2162 - 2168, 1993.

[78] G.H. Waller, P.D. Brooke, B.H. Rainwater, S.Y. Lai, R. Hu, Y. Ding, F.M. Alamgir, K.H. Sandhage and M.L. Liu, "Structure and surface chemistry of Al2O3 coated LiMn2O4 nanostructured electrodes with improved lifetime," *Journal of Power Sources,* vol. 306, pp. 162 - 170, 2016.

[79] C.Y. Ouyang, X.M. Zeng, Z. Sljivancanin and A. Baldereschi, "Oxidation states of Mn atoms at clean and Al2O3-covered LiMn2O4 (001) surfaces," *The Journal of Physical Chemistry C,* vol. 114, no. 10, pp. 4756 - 4759, 2010.

[80] W.-K. Kim, D.-W. Han, W.-H. Ryu, S.-J. Lim and H.-S. Kwon, "Al2O3 coating on LiMn2O4 by electrostatic attraction forces and its effects on the high temperature cyclic performance," *Electrochimica Acta,* vol. 71, pp. 17-21, 2012.

[81] K.A. Walz, C.S. Johnson, J. Genthe, L.C. Stoiber, W.A. Zeltner, M.A. Anderson and M.M. Thackeray, "Elevated temperature cycling stability and electrochemical impedance of LiMn2O4 cathodes with nanoporous ZrO2 and TiO2 coatings," *Journal of Power Sources,* vol. 195, no. 15, pp. 4943 - 4951, 2010.

[82] J.S. Gnanaraj, V.G. Pol, A. Gedanken and D. Aurbach, "Improving the high-temperature performance of LiMn2O4 spinel electrodes by coating the active mass with MgO via a sonochemical method," *Electrochemistry Communications,* vol. 5, p. 940 – 945, 2003.

[83] J.S. Kim, K. Kim, W. Cho, W. H. Shin, R. Kanno and J. W.Choi, *Nano letters,* vol. 12, no. 12, pp. 6358 - 6365, 2012.

[84] S. Aziz, J. Zhao, C. Cain and Y. Wang, "Nanoarchitectured LiMn2O4/Graphene/ZnO Composites as Electrodes for Lithium Ion Batteries," *Journal of Materials Science & Technology,* vol. 30, pp. 427-433, 2014.

[85] D. Liu, X. Liu and Z. He, "Surface modification by ZnO coating for improving the elevated temperature performance of LiMn2O4," *Journal of alloys and compounds,* vol. 436, no. 1 - 2, pp. 387 - 391, 2007.

[86] R.J. Arsenault, S. Fishman and M. Taya, “Deformation and fracture behavior of metal-ceramic matrix composite materials,” *Progress in materials science,* vol. 38, pp. 1 - 157, 1994.

[87] R.H. French, “Electronic band structure of Al2O3, with comparison to Alon and AIN,” *Journal of the American Ceramic Society,* vol. 73, no. 3, pp. 477 - 489, 1990.

[88] G.V. Franks and Y. Gan, “Charging behavior at the alumina-water interface and implications for ceramic processing,” *Journal of the American Ceramic Society,* vol. 90, no. 11, pp. 3373 - 3388, 2007.

[89] B.A. Vázquez, P. Pena, A.H. De Aza, M.A. Sainz and A. Caballero, “Corrosion mechanism of polycrystalline corundum and calcium hexaluminate by calcium silicate slags,” *Journal of the European Ceramic Society,* vol. 29, no. 8, pp. 1347 - 1360, 2009.

[90] W.Y. Ching and Y.N. Xu, “First-Principles Calculation of Electronic, Optical, and Structural Properties of α-Al2O3,” *Journal of the American Ceramic Society,* vol. 77, no. 2, pp. 404 - 411, 1994.

[91] L. Salasco, R. Dovesi, R. Orlando, M. Causa and V.R. Saunders, “A Periodic ab initio extended basis set study of α-Al2O3,” *Molecular physics,* vol. 72, no. 2, pp. 267 - 277, 1991.

[92] J. Ahn and J.W. Rabalais, “Composition and structure of the Al2O3 {0001}-(1x1) surface,” *Surface Science,* vol. 388, no. 1 - 3, pp. 121 - 131, 1997.

[93] J. Guo, D.E. Ellis and D.J. Lam, “Electronic structure and energetics of sapphire (0001) and (11¯02) surfaces,” *Physical Review B,* vol. 45, no. 23, p. 13647, 1992.

[94] J. Toofan and P.R. Watson, “The termination of the α-Al2O3 (0001) surface: a LEED crystallography determination,” *Surface Science,* vol. 401, no. 2, pp. 162 - 172, 1998.

[95] I. Manassidis and M.J. Gillan, “Structure and energetics of alumina surfaces calculated from first principles,” *Journal of the American Ceramic Society,* vol. 77, no. 2, pp. 335 - 338, 1994.

[96] V.E. Puchin, J.D. Gale, A.L. Shluger, E.A. Kotomin, J. Günster, M. Brause and V. Kempter, “Atomic and electronic structure of the corundum (0001) surface: comparison with surface spectroscopies,” *Surface science,* vol. 370, no. 2 - 3, pp. 190 - 200, 1997.

[97] A.C. Thomas and H.H. Richardson, “Growth of Thin Film Water on α-Al2O3 (0001): An FTIR Study,” *The Journal of Physical Chemistry C,* vol. 112, no. 50, pp. 20033 - 20037, 2008.

[98] M. Gautier-Soyer, F. Jollet and C. Noguera, “Influence of surface relaxation on the electronic states of the α-Al2O3 (0001) surface: a self-consistent tight-binding approach,” *Surface science,* vol. 352, pp. 755 - 759, 1996.

[99] S. Alavi, D.C. Sorescu and D.L. Thompson, “Adsorption of HCl on single-crystal α-Al2O3 (0001) surface: a DFT study,” *The Journal of Physical Chemistry B,* vol. 107, no. 1, pp. 186 - 195, 2003.

[100] C.E. Nelson, J.W. Elam, M.A. Tolbert and S.M. George, “H2O and HCl adsorption on single crystal α-Al2O3 (0001) at stratospheric temperatures,” *Applied surface science,* vol. 171, no. 1 - 2, pp. 21 - 33, 2001.

[101] J.W. Elam, C.E. Nelson, M.A. Tolbert and S.M. George, “Adsorption and desorption of HCl on a single-crystal α-Al2O3 (0001) surface,” *Surface science,* vol. 450, no. 1 - 2, pp. 64 - 77, 2000.

[102] C. Rohmann, J.B. Metson and H. Idriss, “DFT study of carbon monoxide adsorption on α-Al2O3 (0001),” *Surface Science,* vol. 605, no. 17 - 18, pp. 1694 - 1703, 2011.

[103] Ø. Borck and E. Schröder, “First-principles study of the adsorption of methanol at the α-Al2O3 (0001) surface,” *Journal of Physics: Condensed Matter,* vol. 18, no. 1, p. 1, 2005.

[104] M. Aykol, S. Kirklin and C. Wolverton, “Thermodynamic Aspects of Cathode Coatings for Lithium-Ion Batteries,” *Advanced Energy Materials,* vol. 4, no. 17, p. 1400690, 2014.

[105] A.M Kannan and A. Manthiram, “Surface/Chemically Modified LiMn2O4 Cathodes for Lithium-Ion Batteries,” *Electrochemical and Solid-State Letters,* vol. 5, no. 7, pp. A167 - A169, 2002.

[106] A. Eftekhari, “Aluminum oxide as a multi-function agent for improving battery performance of LiMn2O4 cathode,” *Solid State Ionics,* vol. 167, no. 3 - 4, pp. 237 - 242, 2004.

[107] Y.Y. Xia, T. Sakai, T. Fujieda, X.Q. Yang, X. Sun, Z.F. Ma, J. McBreen and M. Yoshio,, “Correlating Capacity Fading and Structural Changes in Li1+ y Mn2- y O 4- δ Spinel Cathode Materials: A Systematic Study on the Effects of Li/Mn Ratio and Oxygen Deficiency,” *Journal of The Electrochemical Society,* vol. 148, no. 7, pp. A723 - A729, 2001.

[108] M. Wohlfahrt-Mehrens, C. Vogler and J. Garche, “Aging mechanisms of lithium cathode materials,” *Journal of power sources,* vol. 127, no. 1 - 2, pp. 58 - 64, 2004.

[109] N.S. Kondati and S.D. Elliott, “Modeling the Chemical Mechanism of the Thermal Atomic Layer Etch of Aluminum Oxide: A Density Functional Theory Study of Reactions during HF Exposure,” *Chemistry of Materials,* vol. 30, no. 17, pp. 5912 - 5922, 2018.

[110] K. Amine, J. Liu, S. Kang, I. Belharouak, Y. Hyung, D. Vissers and G. Henriksen, “Improved lithium manganese oxide spinel/graphite Li-ion cells for high-power applications,” *Journal of power sources,* vol. 129, no. 1, pp. 14 - 19, 2004.

[111] S.S. Zhang, K. Xu and T.R. Jow, “LiBOB-based gel electrolyte Li-ion battery for high temperature operation,” *Journal of power Sources,* vol. 154, no. 1, pp. 276 - 280, 2006.

[112] M.H. Fu, K.L. Huang, S.Q. Liu, J.S. Liu and Y.K. Li, “Lithium difluoro (oxalato) borate/ethylene carbonate+ propylene carbonate+ ethyl (methyl) carbonate electrolyte for LiMn2O4 cathode,” *Journal of Power Sources,* vol. 195, no. 3, pp. 862 - 866, 2010.

[113] J. Arai, A. Matsuo, T. Fujisaki and K. Ozawa, “A novel high temperature stable lithium salt (Li2B12F12) for lithium ion batteries,” *Journal of Power Sources,* vol. 193, no. 2, pp. 851 - 854, 2009.

[114] D. Aurbach, Y. Talyosef, B. Markovsky, E. Markevich, E. Zinigrad, L. Asraf, J.S. Gnanaraj and H.J. Kim, “Design of electrolyte solutions for Li and Li-ion batteries: a review,” *Electrochimica Acta,* vol. 50, no. 2 - 3, pp. 247 - 254, 2004.

[115] S.S. Zhang, “A review on electrolyte additives for lithium-ion batteries,” *Journal of Power Sources,* vol. 162, no. 2, pp. 1379 - 1394, 2006.

[116] S.S. Zhang, K. Xu and T.R. Jow, “A thermal stabilizer for LiPF6-based electrolytes of Li-ion cells,” *Electrochemical and solid-state letters,* vol. 5, no. 9, pp. A206 - A208, 2002.

[117] X. Sun, H.S. Lee, X.Q. Yang and J. McBreen , “Using a boron-based anion receptor additive to improve the thermal stability of LiPF6-based electrolyte for lithium batteries,” *Electrochemical and solid-state letters,* vol. 5, no. 11, pp. A248 - A251, 2002.

[118] H. Yamane, T. Inoue, M. Fujita and M. Sano, “A causal study of the capacity fading of Li1.01Mn1.99O4 cathode at 80° C, and the suppressing substances of its fading,” *Journal of power sources,* vol. 99, no. 1 - 2, pp. 60 - 65, 2001.

[119] X. Wu, X. Li, Z. Wang, H. Guo and L. Xiong, “Investigation on the storage performance of LiMn 2 O 4 at elevated temperature with the mixture of electrolyte stabilizer,” *Ionics,* vol. 18, no. 9, pp. 907 - 911, 2012.

[120] X. Wu, X. Li, Z. Wang, H. Guo, P. Yue and Y. Zhang, “Improvement on the storage performance of LiMn2O4 with the mixed additives of ethanolamine and heptamethyldisilazane,” *Applied Surface Science,* vol. 268, pp. 349 - 354, 2013.

[121] K. Abe, H. Yoshitake, T. Kitakura, T. Hattori, H. Wang and M. Yoshio, “Additives-containing functional electrolytes for suppressing electrolyte decomposition in lithium-ion batteries,” *Electrochimica acta,* vol. 49, no. 26, pp. 4613 - 4622, 2004.

[122] K. Xu, “Nonaqueous liquid electrolytes for lithium-based rechargeable batteries,” *Chemical review,* vol. 104, no. 10, pp. 4303 - 4418, 2004.

[123] I.H. Cho, S.S. Kim, S.C. Shin and N.S. Choi, “Effect of SEI on capacity losses of spinel lithium manganese oxide/graphite batteries stored at 60 C,” *Electrochemical and Solid-State Letters,* vol. 13, no. 11, pp. A168 - A172, 2010.

[124] D. Guyomard and J.M. Tarascon, “Li Metal-Free Rechargeable LiMn2O4/Carbon Cells: Their Understanding and Optimization,” *Journal of The Electrochemical Society,* vol. 139, no. 4, pp. 937 - 948, 1992.

[125] L. Xing, W. Li, C. Wang, F. Gu, M. Xu, C. Tan and J. Yi, “Theoretical investigations on oxidative stability of solvents and oxidative decomposition mechanism of ethylene carbonate for lithium ion battery use,” *The Journal of Physical Chemistry B,* vol. 113, no. 52, pp. 16596 - 16602, 2009.

[126] J.C. Soetens, C. Millot and B. Maigret, “Molecular dynamics simulation of Li+ BF4-in ethylene carbonate, propylene carbonate, and dimethyl carbonate solvents,” *The Journal of Physical Chemistry A,* vol. 102, no. 7, pp. 1055 - 1061, 1998.

[127] S.I. Tobishima and T. Okada, “Lithium cycling efficiency and conductivity for high dielectric solvent/low viscosity solvent mixed systems,” *Electrochimica acta,* vol. 30, no. 12, pp. 1715 - 1722, 1985.

[128] Y. Hu, W. Kong, H. Li, X. Huang and L. Chen, “Experimental and theoretical studies on reduction mechanism of vinyl ethylene carbonate on graphite anode for lithium ion batteries,” *Electrochemistry communications,* vol. 6, no. 2, pp. 126 - 131, 2004.

[129] M. Fujimoto, Y. Shouji, T. Nohma and K. Nishio, “Charge-Discharge Characteristics of Natural Graphite Electrode in Some Cyclic Carbonates,” *Denki Kagaku,* vol. 65, pp. 949 - 953, 1997.

[130] J.T. Lee, Y.W. Lin and Y.S. Jan, “Allyl ethyl carbonate as an additive for lithium-ion battery electrolytes,” *Journal of power sources,* vol. 132, no. 1 - 2, pp. 244 - 248, 2004.

[131] Y. Chernyak, “Dielectric Constant, Dipole Moment, and Solubility Parameters of Some Cyclic Acid Esters,” *Journal of Chemical & Engineering Data,* vol. 51, no. 2, pp. 416 - 418, 2006.

[132] R. Payne and I.E. Theodorou, “Dielectric properties and relaxation in ethylene carbonate and propylene carbonate,” *The Journal of Physical Chemistry,* vol. 76, no. 20, pp. 2892 - 2900, 1972.

[133] K. Leung, “First-principles modeling of the initial stages of organic solvent decomposition on Li x Mn2O4 (100) surfaces,” *The Journal of Physical Chemistry C,* vol. 116, no. 18, pp. 9852 - 9861, 2012.

[134] R. Fong, U. Von Sacken and J.R. Dahn, “Studies of lithium intercalation into carbons using nonaqueous electrochemical cells,” *Journal of The Electrochemical Society,* vol. 137, no. 7, pp. 2009 - 2013, 1990.

[135] L. Giordano, P. Karayaylali, Y. Yu, Y. Katayama, F. Maglia, S. Lux and Y. Shao-Horn, “Chemical Reactivity Descriptor for the Oxide-Electrolyte Interface in Li-Ion Batteries,” *Journal of Physical Chemitry Letters,* vol. 8, no. 16, pp. 3881 - 3887, 2017.

[136] N. Kumar, K. Leung and D.J. Siegela, “Crystal Surface and State of Charge Dependencies of Electrolyte Decomposition on LiMn2O4 Cathode,” *Journal of The Electrochemical Society,* vol. 161, no. 8, pp. E3059 - E3065 , 2014.

[137] T.M. Østergaard, L. Giordano, I.E. Castelli, F. Maglia, B.K. Antonopoulos,Y. Shao-Horn and J. Rossmeisl, “Oxidation of Ethylene Carbonate on Li Metal Oxide Surfaces,” *The Journal of Physical Chemistry C,* vol. 122, no. 19, pp. 10442 - 10449, 2018.

[138] A. M. Kannan and A. Manthiram, “Surface/Chemically Modified LiMn2 O 4 Cathodes for Lithium-Ion Batteries,” *Electrochem. Solid-State Lett.,* vol. 5, no. 7, pp. 167-169, 2002.

[139] I. Tomeno, Y. Kasuya and Y. Tsunoda, “Charge and spin ordering in LiMn2O4,” *Physical Review B,* vol. 64, no. 9, p. 094422, 2001.

[140] Y.G. Chukalkin, A.E. Teplykh, A.N. Pirogov and D.G. Kellerman, “Magnetism of LiMn2O4 manganite in structurally ordered and disordered states,” *Physics of the Solid State,* vol. 52, no. 12, pp. 2545 - 2551, 2010.

[141] A.S. Wills, N.P. Raju and J.E. Greedan, “Low-temperature structure and magnetic properties of the spinel LiMn2O4: A frustrated antiferromagnet and cathode material,” *Chemistry of materials,* vol. 11, no. 6, pp. 1510 - 1518, 1999.

[142] A. Karim, S. Fosse, and K. A. Persson, “Surface structure and equilibrium particle shape of the LiMn2O4 spinel from first-principles calculations,” *Physical Review B,* vol. 87, no. 7, pp. 075322-1 - 075322-6, 2013.

[143] D. Santos-Carballal, P.E. Ngoepe and N.H. de Leeuw, “Ab initio investigation of the thermodynamics of cation distribution and of the electronic and magnetic structures in the LiMn2O4 spinel,” *Physical Review B,* vol. 97, no. 8, pp. 085126-1 - 085126-11, 2018.

[144] J. Bhattacharya and C. Wolverton, “Relative stability of normal vs. inverse spinel for 3d transition metal oxides as lithium intercalation cathodes,” *Physical Chemistry Chemical Physics,* vol. 15, no. 17, pp. 6486 - 6498, 2013.

[145] C.Y. Ouyang, S.Q. Shi, Z.X. Wang, H. Li, X.J Huang and L.Q. Chen, “Ab initio molecular-dynamics studies on LixMn2O4 as cathode material for lithium secondary batteries,” *Europhysics Letters,* vol. 67, no. 1, p. 28, 2004.

[146] R. Benedek and M.M. Thackeray, “Simulation of the Surface Structure of Lithium Manganese Oxide Spinel,” *Physical Review B,* vol. 83, no. 19, pp. 195439-1 - 195439-8, 2011.

[147] R.E. Warburton, H. Iddir, L.A. Curtiss and J. Greeley, “Thermodynamic stability of low-and high-index spinel LiMn2O4 surface terminations,” *ACS applied materials & interfaces,* vol. 8, no. 17, pp. 11108 - 11121, 2016.

[148] A. Karim, S. Fosse and K.A. Persson, “Surface structure and equilibrium particle shape of the LiMn 2 O 4 spinel from first-principles calculations,” *Physical Review B,* vol. 87, no. 7, pp. 075322-1 - 075322-6, 2013.

[149] S. Kim, M. Aykol and C. Wolverton, “Surface phase diagram and stability of (001) and (111) LiMn2O4 spinel oxides.,” *Physical Review B,* vol. 92, no. 11, pp. 115411-1 - 115411-10, 2015.

[150] Y.K. Lee, J. Park and W. Lu, “Electronic and Bonding Properties of LiMn2O4 Spinel with Different Surface Orientations and Doping Elements and Their Effects on Manganese Dissolution,” *Journal of The Electrochemical Society,* vol. 163, no. 7, pp. A1359 - A1368, 2016.

[151] P. W. Tasker, “The stability of ionic crystal surfaces,” *Journal of Physics C: Solid State Physics,* vol. 12, pp. 4977 - 4984, 1979.

[152] R. Benedek and M.M. Thackeray, “Simulation of the surface structure of lithium manganese oxide spinel,” *Physical Review B,* vol. 83, no. 19, pp. 195439-1 - 195439-8, 2011.

[153] C.M. Fang, S.C. Parker and G. de With, “Atomistic simulation of the surface energy of spinel MgAl2O4,” *Journal of the American Ceramic Society,* vol. 83, no. 8, pp. 2082 - 2084, 2000.

[154] H. Huang, C.A. Vincent, P.G. Bruce, “Correlating capacity loss of stoichiometric and nonstoichiometric lithium manganese oxide spinel electrodes with their structural integrity,” *Journal of The Electrochemical Society,* vol. 146, no. 10, pp. 3649 - 3654, 1999.

[155] T. Takada, H. Hayakawa, H. Enoki, E. Akiba, H. Slegr, I. Davidson, J. Murray, “Journal of Power Sources,” *Structure and electrochemical characterization of Li1+xMn2−xO4 spinels for rechargeable lithium batteries,* Vols. 81 - 82, pp. 505 - 509 , 1999.

[156] J.S. Kim, K. Kim, W. Cho, W. H. Shin, R. Kanno and J. W.Choi, “A Truncated Manganese Spinel Cathode for Excellent Power and Lifetime in Lithium-Ion Batteries,” *Nano letters,* vol. 12, no. 12, pp. 6358 - 6365, 2012.

[157] F.P. Nkosi, C.J. Jafta, M. Kebede, L. Le Roux, M.K. Mathe and K.I. Ozoemena, "Microwave-assisted optimization of the manganese redox states for enhanced capacity and capacity retention of LiAl x Mn 2- x O 4 (x= 0 and 0.3) spinel materials," *RSC Advances,* vol. 5, no. 41, pp. 32256 - 32262, 2015.

[158] K. Raju, F.P. Nkosi, E. Viswanathan, M.K. Mathe, K. Damodaran and K.I. Ozoemena, "Microwave-enhanced electrochemical cycling performance of the LiNi 0.2 Mn 1.8 O 4 spinel cathode material at elevated temperature," *Physical Chemistry Chemical Physics,* vol. 18, no. 18, pp. 13074 - 13083, 2016.

[159] S. Shi, C. Ouyang, D.S. Wang, L. Chen and X. Huang, "The effect of cation doping on spinel LiMn2O4: a first-principles investigation," *Solid state communications,* vol. 126, no. 9, pp. 531 - 534, 2003.

[160] D. Capsoni, M. Bini, G. Chiodelli, V. Massarotti, C.B. Azzoni, M.C. Mozzati and A. Comin, "Inhibition of Jahn–Teller cooperative distortion in LiMn2O4 spinel by transition metal ion doping," *Physical Chemistry Chemical Physics,* vol. 3, no. 11, pp. 2162 - 2166, 2001.

[161] P. Strobel, A.I. Palos, M. Anne and F. Le Cras, "Structural, magnetic and lithium insertion properties of spinel-type Li2Mn3MO8 oxides (M= Mg, Co, Ni, Cu)," *Journal of Materials Chemistry,* vol. 10, no. 2, pp. 429 - 436, 200.

[162] S. Shi, C. Ouyang, D.S. Wang, L. Chen and X. Huang, "The effect of cation doping on spinel LiMn2O4: a first-principles investigation," *Solid state communications,* vol. 126, no. 9, pp. 531 - 534, 2003.

[163] L. Xiao, Y. Zhao, Y. Yang, Y. Cao, X. Ai and H. Yang, "Enhanced electrochemical stability of Al-doped LiMn2O4 synthesized by a polymer-pyrolysis method," *Electrochimica Acta,* vol. 54, no. 2, pp. 545 - 550, 2008.

[164] Y.L. Ding, J. Xie, G.S. Cao, T.J. Zhu, H.M. Yu and X.B. Zhao, "Enhanced elevated-temperature performance of Al-doped single-crystalline LiMn2O4 nanotubes as cathodes for lithium ion batteries.," *Journal of Physical Chemistry C,* vol. 115, no. 19, pp. 9821 - 9825, 2011.

[165] M.A. Kebede, M.J. Phasha, N. Kunjuzwa, L.J. Le Roux, D. Mkhonto, K.I. Ozoemena and M.K. Mathe, "Structural and electrochemical properties of aluminium doped LiMn2O4 cathode materials for Li battery: experimental and ab initio calculations," *Sustainable Energy Technologies and Assessments,* vol. 5, pp. 44 - 49, 2014.

[166] S. Mandal, R.M. Rojas, J.M. Amarilla, P. Calle, N.V. Kosova, V.F. Anufrienko and J.M. Rojo, "High temperature Co-doped LiMn2O4-based spinels. Structural, electrical, and electrochemical characterization," *Chemistry of materials,* vol. 14, no. 4, pp. 1598 - 1605, 2002.

[167] Z. Wang, J. Du, Z. Li and Z. Wu, “Sol–gel synthesis of Co-doped LiMn2O4 with improved high-rate properties for high-temperature lithium batteries,” *Ceramics International,* vol. 40, no. 2, pp. 3527 - 3531, 2014.

[168] Y. Yu, M. Xiang, J. Guo, C. Su, X. Liu, H. Bai, W. Bai and K. Duan, “Enhancing high-rate and elevated-temperature properties of Ni-Mg co-doped LiMn2O4 cathodes for Li-ion batteries.,” *Journal of colloid and interface science,* vol. 555, pp. 64 - 71, 2019.

[169] T.F. Yi, L.C. Yin, Y.Q. Ma, H.Y. Shen, Y.R. Zhu and R.S. Zhu, “Lithium-ion insertion kinetics of Nb-doped LiMn2O4 positive-electrode material,” *Ceramics International,* vol. 39, no. 4, pp. 4673 - 4678, 2013.

[170] Z. Zhang, R. Xun, Z. Shen, L. Wang, S. Wang and Z. Meng, “Synthesis of Nb-Doped Li2ZnTi3O8 Anode with Long Cycle Life and Applications in the LiMn2O4/Li2ZnTi3O8 Full Cell,” *ACS Sustainable Chemistry & Engineering,* vol. 8, no. 7, pp. 2763 - 2771, 2020.

[171] Y. Deng, J. Mou, H. Wu, L. Zhou, Q. Zheng, K.H. Lam, C. Xu and D. Lin, “Enhanced Electrochemical Performance in Ni-Doped LiMn2O4-Based Composite Cathodes for Lithium-Ion Batteries,” *ChemElectroChem,* vol. 4, no. 6, pp. 1362 - 1371, 2017.

[172] Yang, S., Schmidt, D.O., Khetan, A., Schrader, F., Jakobi, S., Homberger, M., Noyong, M., Paulus, A., Kungl, H., Eichel, R.A. and Pitsch, H., “Electrochemical and electronic charge transport properties of Ni-doped LiMn2O4 spinel obtained from polyol-mediated synthesis,” *Materials,* vol. 11, no. 5, p. 806, 2018.

[173] dos Santos Junior, G.A., Fortunato, V.D., Bastos, G.A., Silva, G.G., Ortega, P.F. and Lavall, R.L., “High-Performance Lithium-Ion Hybrid Supercapacitors Based on Lithium Salt/Imidazolium Ionic Liquid Electrolytes and Ni-Doped LiMn2O4 Cathode Materials,” *ACS Applied Energy Materials,* vol. 3, no. 9, pp. 9028-9039, 2020.

[174] Kasnatscheew, J., Röser, S., Börner, M. and Winter, M., 2019. Do Increased Ni Contents in LiNi x Mn y Co z O2 (NMC) Electrodes Decrease Structural and Thermal Stability of Li Ion Batteries? A Thorough Look by Consideration of the Li+ Extraction Ratio. A, “Do Increased Ni Contents in LiNi x Mn y Co z O2 (NMC) Electrodes Decrease Structural and Thermal Stability of Li Ion Batteries? A Thorough Look by Consideration of the Li+ Extraction Ratio.,” *ACS Applied Energy Materials,* vol. 2, no. 11, pp. 7733-7737, 2019.

[175] Li, J., Du, Z., Ruther, R.E., An, S.J., David, L.A., Hays, K., Wood, M., Phillip, N.D., Sheng, Y., Mao, C. and Kalnaus, S., “Toward low-cost, high-energy density, and high-power density lithium-ion batteries,” *JOM,* vol. 69, no. 9, pp. 1484 - 1496, 2017.

[176] Wu, F., Yan, Y., Wang, R., Cai, H., Tong, W. and Tang, H., "Synthesis of LiNi1/3Mn1/3Co1/3O2@ graphene for lithium-ion batteries via self-assembled polyelectrolyte layers," *Ceramics International,* vol. 43, no. 10, pp. 7668-7673, 2017.

[177] Lee, Y.G., Fujiki, S., Jung, C., Suzuki, N., Yashiro, N., Omoda, R., Ko, D.S., Shiratsuchi, T., Sugimoto, T., Ryu, S. and Ku, J.H., " High-energy long-cycling all-solid-state lithium metal batteries enabled by silver–carbon composite anodes," *Nature Energy,* vol. 5, no. 4, pp. 299-308, 2020.

[178] S. Matsuyama, S. Kinugasa, K. Tanabe and T. Tamura, "Spectral Database for Organic Compounds, SDBS," National Institute of Advanced Industrial Science and Technology (AIST), 31 03 1999. [Online]. Available: https://sdbs.db.aist.go.jp/sdbs/cgi-bin/landingpage?sdbsno=2392. [Accessed 30 11 2018].

[179] S.N. Altunata and R.W. Field, "Modeling LiH potential-energy curves: An approach based on integration in finite space," *Physical Review A,* vol. 67, no. 2, p. 022507, 2003.

[180] M. Mueller, Fundamentals of quantum chemistry: molecular spectroscopy and modern electronic structure computations, New York, Boston, Dordrecht, London, Moscow: Kluwer Academic , 2002.

[181] R. Martin, Electronic structure: basic theory and practical methods, Cambridge: Cambridge university press, 2004.

[182] N. Argaman and G. Makov, "Density functional theory: An introduction," *American Journal of Physics,* vol. 68, no. 1, pp. 69 - 79, 2000.

[183] W. Kohn, A.D. Becke and R.G. Parr, "Density functional theory of electronic structure," *The Journal of Physical Chemistry,* vol. 100, no. 31, pp. 12974 - 12980, 1996.

[184] L. Thomas, "The calculation of atomic fields," in *Mathematical Proceedings of the Cambridge Philosophical Society*, vol. 23, Cambridge, Cambridge University Press, 1927, pp. 542 - 548.

[185] P. Hohenberg and W. Kohn, "Inhomogeneous electron gas," *Physical review,* vol. 136, no. 3B, pp. B864 - B871, 1964.

[186] R.A Evarestov, Quantum chemistry of solids: the LCAO first principles treatment of crystals, Springer Science & Business Media, 2007.

[187] W. Kohn and L.J. Sham, "Self-consistent equations including exchange and correlation effects," *Physical review,* vol. 140, no. 4A, p. A1133, 1965.

[188] L.J. Sham and W. Kohn, "One-particle properties of an inhomogeneous interacting electron gas," *Physical Review,* vol. 145, no. 2, p. 561, 1966.

[189] D.C. Langreth and J.P. Perdew, “The exchange-correlation energy of a metallic surface,” *Solid State Communications,* vol. 17, no. 11, pp. 1425 - 1429, 1975.

[190] O. Gunnarsson and B.I. Lundqvist, “Exchange and correlation in atoms, molecules, and solids by the spin-density-functional formalism,” *Physical Review B,* vol. 13, no. 10, p. 4274, 1976.

[191] K. Horn and M. Scheffler, Electronic structure, vol. 2, Amsterdam, The Netherlands: Elsevier, 2000.

[192] D.J.W. Geldart and M. Rasolt, “Exchange and correlation energy of an inhomogeneous electron gas at metallic densities,” *Physical Review B,* vol. 13, no. 4, p. 1477, 1976.

[193] P.A. Dirac, “Note on exchange phenomena in the Thomas atom,” in *Mathematical Proceedings of the Cambridge Philosophical Society*, Cambridge, Cambridge University Press, 1930, pp. 376 - 385.

[194] G.P. Robert, and Y. Weitao, Density-Functional Theory of Atoms and Molecules., Oxford: Oxford University Press, 1994.

[195] E.K.U. Gross andR.M. Dreizler, Density functional theory: an approach to the quantum many-body problem, Berlin: Springer, 1990.

[196] R.G. Parr and W. Yang, Density Functional Theory of Atoms and Molecules, New York: Oxford Univ: Press, 1989.

[197] S.H. Vosko, L. Wilk and M. Nusair, “Accurate spin-dependent electron liquid correlation energies for local spin density calculations: a critical analysis,” *Canadian Journal of physics,* vol. 58, no. 8, pp. 1200 - 1211, 1980.

[198] J.P. Perdew and A. Zunger, “Self-interaction correction to density-functional approximations for many-electron systems,” *Physical Review B,* vol. 23, no. 10, pp. 5048 - 5079, 1981.

[199] G. Kresse and D. Joubert, “From ultrasoft pseudopotentials to the projector augmented-wave method,” *Physical Review B,* vol. 19, no. 3, pp. 1758 - 1775, 1999.

[200] J.P. Perdew, *Phys. Rev. B,* vol. 172, no. 6, 1991.

[201] A. St.-Amant, W.D. Cornell, P.A. Kollman and T.A. Halgren, “Calculation of molecular geometries, relative conformational energies, dipole moments, and molecular electrostatic potential fitted charges of small organic molecules of biochemical interest by density functional theory,” *Journal of computational chemistry,* vol. 16, no. 12, pp. 1483 - 1506, 1995.

[202] P. Politzer and J.M. Seminario, Modern density functional theory: a tool for chemistry, Lausanne-New York- Oxford- Shannon- Tokyo: Elsevier, 1995.

[203] A.D. Becke, “Density-functional exchange-energy approximation with correct asymptotic behavior,” *Physical review A,* vol. 38, no. 6, p. 3098, 1988.

[204] J.P. Perdew, “Density-functional approximation for the correlation energy of the inhomogeneous electron gas,” *Physical Review B,* vol. 33, no. 12, p. 8822, 1986.

[205] J.P. Perdew and Y. Wang, “Accurate and simple density functional for the electronic exchange energy: Generalized gradient approximation,” *Physical review B,* vol. 33, no. 12, p. 8800, 1986.

[206] P Ziesche, J.P. Perdew and H. Eschrig , Electronic structure of solids’ 91, Berlin: Akademie Verlag, 1991.

[207] M.C. Payne, M.P. Teter, D.C. Allan, T.A. Arias and A.J. Joannopoulos, “Iterative minimization techniques for ab initio total-energy calculations: molecular dynamics and conjugate gradients,” *Reviews of modern physics,* vol. 64, no. 4, pp. 1045 - 1097, 1992.

[208] J.P. Perdew, K. Burke and Y. Wang, “Generalized gradient approximation for the exchange-correlation hole of a many-electron system,” *Physical Review B,* vol. 54, no. 23, pp. 16533 - 16539, 1996.

[209] J.C. Phillips and L. Kleinman, “New method for calculating wave functions in crystals and molecules,” *Physical Review,* vol. 116, no. 2, pp. 287 - 294, 1959.

[210] V. Heine and D. Weaire, “Pseudopotential theory of cohesion and structure,” *Solid state physics,* vol. 24, pp. 249 - 463, 1970.

[211] P.E. Blöchl, “Projector augmented-wave method,” *Physical review B,* vol. 50, no. 24, pp. 17953 - 17979, 1994.

[212] T. Cottenier, A. Van Den Berg and T. Elrad, “Modeling aspect-oriented compositions,” in *International Conference on Model Driven Engineering Languages and Systems*, Berlin, Heidelberg, Springer, 2005, pp. 100 - 109.

[213] G. Kresse, M. Marsman and J. Furthmüller, “VASP the GUIDE, Computational Physics,” *Faculty of Physics, Universität Wien Sensengasse,* vol. 8, 2009.

[214] D. Vanderbilt, “Soft self-consistent pseudopotentials in a generalized eigenvalue formalism,” *Physical review B,* vol. 41, no. 11, pp. 7892 - 7895, 1990.

[215] G. Kresse and J. Furthmüller, “Efficient iterative schemes for ab initio total-energy calculations using a plane-wave basis set,” *Physical review B,* vol. 54, no. 16, p. 11169, 1996.

[216] J.P. Perdew, K. Burke and M. Ernzerhof, “Generalized gradient approximation made simple,” *Physical review letters,* vol. 77, no. 18, pp. 11169 - 11186, 1996.

[217] P. Blöchl, “Projector augmented-wave method,” *Physical review B,* vol. 50, no. 24, pp. 17953 - 17979, 1994.

[218] S. Grimme, S. Ehrlich and L. Goerigk, “Effect of the damping function in dispersion corrected density functional theory,” *Journal of computational chemistry,* vol. 32, no. 7, pp. 1456 - 1465, 2011.

[219] S. Grimme, J. Antony, S. Ehrlich and H. Krieg, “A consistent and accurate ab initio parametrization of density functional dispersion correction (DFT-D) for the 94 elements H-Pu,” *The Journal of chemical physics,* vol. 132, no. 15, p. 154104, 2010.

[220] P.E. Blöchl, O. Jepsen and O.K. Andersen, “Improved tetrahedron method for Brillouin-zone integrations,” *Physical Review B,* vol. 49, no. 23, pp. 16223 - 16233, 1994.

[221] V.I. Anisimov, M.A. Korotin, J. Zaanen and O.K. Andersen, “Spin bags, polarons, and impurity potentials in La2-xSrxCuO4 from first principles,” *Physical review letters,* vol. 68, no. 3, pp. 345 - 348, 1992.

[222] S.L. Dudarev, G.A Botton, S.Y. Savrasov, C.J. Humphreys and A.P. Sutton, “Electron-energy-loss spectra and the structural stability of nickel oxide: An LSDA+ U study,” *Physical Review B,* vol. 57, no. 3, pp. 1505 - 1509, 1998.

[223] C.Y. Ouyang, S.Q. Shi and M.S. Lei, “Jahn–Teller distortion and electronic structure of LiMn2O4,” *Journal of Alloys and Compounds,* vol. 474, no. 1 - 2, pp. 370 - 374, 2009.

[224] D. Santos Carballal, “Computational studies of magnetite Fe_3O_4 and related spinel-structured materials,” UCL (University College London), London, 2015.

[225] J.M. Seddon and J.D. Gale, Thermodynamics and statistical mechanics, Cambridge: Royal Society of Chemistry, 2001.

[226] D. Alfè, “PHON: A program to calculate phonons using the small displacement method,” *Computer Physics Communications,* vol. 180, no. 12, pp. 2622 - 2633, 2009.

[227] Z. Zhou and B. Joos, “Stability criteria for homogeneously stressed materials and the calculation of elastic constants,” *Physical Review B,* vol. 54, no. 6, pp. 3841 - 3850, 1996.

[228] O. Beckstein, J.E. Klepeis, G.L.W. Hart and O. Pankratov, “First-principles elastic constants and electronic structure of α- Pt 2 Si and PtSi,” *Physical Review B,* vol. 63, no. 13, pp. 134112-1 - 134112-12, 2001.

[229] B.B. Karki, G.J. Ackland and J. Crain, “Elastic instabilities in crystals from ab initio stress-strain relations,” *Journal of Physics: Condensed Matter,* vol. 9, no. 41, pp. 8579 - 8589, 1997.

[230] A.J.M Spencer, H.G. Hopkins and M.J. Sewell, “Mechanics of solids,” *The R. Hill 60th Anniversary Vol.(Ed. Hopkins and Sewell),* vol. 607, 1982.

[231] M. Tang and S. Yip, “Lattice instability in B-SiC and simulation of brittle fracture,” *Journal of applied physics,* vol. 76, no. 5, pp. 2719 - 2725, 1994.

[232] J. Wang, J. Li, S. Yip, S. Phillpot and D. Wolf, “Mechanical instabilities of homogeneous crystals,” *Physical Review B,* vol. 52, no. 17, p. 12627 12635, 1995.

[233] T.H.K. Barron and M.L. Klein, “Second-order elastic constants of a solid under stress,” *Proceedings of the Physical Society,* vol. 85, no. 3, pp. 523 - 532, 1965.

[234] C. Kittel, Introduction to solid state physics, New York: Wiley, 1976.

[235] M.L. Cohen, “Calculation of bulk moduli of diamond and zinc-blende solids,” *Physical Review B,* vol. 32, no. 12, pp. 7988 -, 1985.

[236] S. Pugh, “XCII. Relations between the elastic moduli and the plastic properties of polycrystalline pure metals,” *The London, Edinburgh, and Dublin Philosophical Magazine and Journal of Science,* vol. 45, no. 367, pp. 823 - 843, 1954.

[237] S.F. Pugh, “XCII. Relations between the elastic moduli and the plastic properties of polycrystalline pure metals,” *The London, Edinburgh, and Dublin Philosophical Magazine and Journal of Science,* vol. 45, no. 367, pp. 823 - 843, 1954.

[238] J. Gibbs, “On the equilibrium of heterogeneous substances,” *Transactions of the Connecticut Academy of Arts and Sciences,* vol. 3, pp. 108-248 , 1875.

[239] G. Wulff, “Xxv. zur frage der geschwindigkeit des wachsthums und der auflösung der krystallflächen,” *Zeitschrift für Kristallographie-Crystalline Materials,* vol. 34, no. 1 - 6, pp. 449 - 530, 1901.

[240] I. Fonseca, “The Wulff theorem revisited,” *Proceedings of the Royal Society of London. Series A: Mathematical and Physical Sciences,* vol. 432, no. 1884, pp. 125 - 145, 1991.

[241] C. Fonseca Guerra, J.W. Handgraaf, E.J. Baerends and F.M. Bickelhaupt, “Voronoi deformation density (VDD) charges: Assessment of the Mulliken, Bader, Hirshfeld, Weinhold, and VDD methods for charge analysis,” *Journal of computational chemistry,* vol. 25, no. 2, pp. 189 - 210, 2004.

[242] K.E. Laidig and R.F. Bader, “Properties of atoms in molecules: Atomic polarizabilities,” *The Journal of chemical physics,* vol. 93, no. 10, pp. 7213 - 7224, 1990.

[243] G. Henkelman, A. Arnaldsson and H. Jónsson, “A fast and robust algorithm for Bader decomposition of charge density,” *Computational Materials Science,* vol. 36, no. 3, pp. 354 - 360, 2006.

[244] K. Parlinski, Z.Q. Li, Y. Kawazoe, “First-principles determination of the soft mode in cubic ZrO2,” *Physical Review Letters,* vol. 78, no. 21, p. 4063, 1997.

[245] M.J. Phasha, P.E. Ngoepe, H.R. Chauke, D.G. Pettifor and D. Nguyen-Mann, “Link between structural and mechanical stability of fcc-and bcc-based ordered Mg–Li alloys,” *Intermetallics,* vol. 18, no. 11, pp. 2083 - 2089, 2010.

[246] N. Ishizawa, K. Tateishi, S. Oishi, and S. Kishimoto, “Bond-length fluctuation in the orthorhombic 3×3×1 superstructure of LiMn2O4 spinel,” *American Mineralogist,* vol. 99, no. 8 - 9, pp. 1528 - 1536, 2014.

[247] R. Yamaguchi, H. Ikuta and M. Wakihara, “Heat of Formation for LiMyMn2− yO4 (M= Co, Cr, Li, Mg, Ni) Spinel Solid Solution,” *Journal of thermal analysis and calorimetry,* vol. 57, no. 3, pp. 797 - 806, 1999.

[248] M. Wang and A. Navrotsky, “Thermochemistry of Li1+ xMn2− xO4 (0⩽ x⩽ 1/3) spinel,” *Journal of Solid State Chemistry,* vol. 178, no. 4, pp. 1182 - 1189, 2005.

[249] A. Piyadasa, S. Wang and P.-X. Gao, “Band structure engineering strategies of metal oxide semiconductor nanowires and related nanostructures: A review,” *Semiconductor Science and Technology,* vol. 32, pp. 1 - 17, 2017.

[250] R. Mahlangu, M.J. Phasha, H.R. Chauke and P.E. Ngoepe, “Structural, elastic and electronic properties of equiatomic PtTi as potential high-temperature shape memory alloy,” *Intermetallics,* vol. 33, pp. 27 - 32, 2013.

[251] Z.J. Wu, E.J. Zhao, H.P. Xiang, X.F. Hao, X.J. Liu and J. Meng, “Crystal structures and elastic properties of superhard IrN2 and IrNr3 from first principle,” *Physical Review B,* vol. 76, pp. 054115-1 - 054115-15, 2007.

[252] M. Mohr, J. Maultzsch, E. Dobardži, S. Reich, I. Miloševi, M. Damnjanovi, A. Bosak, M. Krisch and C. Thomsen, “Phonon dispersion of graphite by inelastic x-ray scattering,” *Physical Review B,* vol. 76, pp. 035439-1 - 035439-7, 2007.

[253] G.W. Watson, E.T. Kelsey, N.H. de Leeuw, D.J. Harris and S.C. Parker, “Atomistic simulation of dislocations, surfaces and interfaces in MgO,” *Journal of the Chemical Society, Faraday Transactions,* vol. 92, no. 3, pp. 433 - 438, 1996.

[254] C.Y. Ouyang, X.M. Zeng, Z. Šljivancanin and A. Baldereschi, “Oxidation States of Mn Atoms at Clean and Al2O3-Covered LiMn2O4(001) Surfaces,” *The Journal of Physical Chemistry C,* vol. 114, no. 10, pp. 4756 - 4759, 2010.

[255] M. Masia, M. Probst and R. Rey, “Ethylene carbonate- Li+: A theoretical study of structural and vibrational properties in gas and liquid phases,” *The Journal of Physical Chemistry B,* vol. 108, no. 6, pp. 2016 - 2027, 2004.

[256] Y. Wang, S. Nakamura, M. Ue and P.B. Balbuena, “Theoretical studies to understand surface chemistry on carbon anodes for lithium-ion batteries: reduction mechanisms of ethylene carbonate,” *Journal of the American Chemical Society,* vol. 123, no. 47, pp. 11708 - 11718, 2001.

[257] L.B. Silva and L.C.G. Freitas, “Structural and thermodynamic properties of liquid ethylene carbonate and propylene carbonate by Monte Carlo Simulations,” *Journal of Molecular Structure: THEOCHEM,* vol. 806, no. 1 - 3, pp. 23 - 34, 2007.

[258] E.G. Leggesse, k.H. Tsau, Y.T. Liu, S. Nachimuthu and J.C. Jiang, “Adsorption and Decomposition of Ethylene Carbonate on LiMn2O4 Cathode Surface,” *Electrochimica Acta,* vol. 210, pp. 61 - 70, 2016.

[259] T. Takada, H. Hayakawa, H. Enoki, E. Akiba, H. Slegr, I. Davidson, J. Murray, “Structure and electrochemical characterization of Li1+xMn2−xO4 spinels for rechargeable lithium batteries,” *Journal of Power Sources,* Vols. 81 - 82, pp. 505 - 509, 1999.

[260] D. Santos-Carballal, A. Roldan, N.Y. Dzade and N.H. de Leeuw, “Reactivity of CO2 on the surfaces of magnetite (Fe3O4), greigite (Fe3S4) and mackinawite (FeS),” *Philosophical Transactions of the Royal Society A: Mathematical, Physical and Engineering Sciences,* vol. 376, no. 2110, p. 20170065, 2017.

[261] B. Fortunato, P. Mirone and G. Fini, “Infrared and Raman spectra and vibrational assignment of ethylene carbonate,” *Spectrochimica Acta Part A: Molecular Spectroscopy,* vol. 27, no. 9, pp. 1917 - 1927, 1971.

[262] J. Cho, Y.J. Kim and B. Park, “Novel LiCoO2 cathode material with Al2O3 coating for a Li ion cell,” *Chemistry of Materials,* vol. 12, no. 12, pp. 3788 - 3791, 2000.

[263] S. Li, K. Zhu, D. Zhao, Q. Zhao and N. Zhang, “Porous LiMn2O4 with Al2O3 coating as high-performance positive materials,” *Ionics ,* pp. 1 - 8, 2018.

[264] S. Aziz, J. Zhao, C. Cain and Y. Wang, “Nanoarchitectured LiMn2O4/Graphene/ZnO composites as electrodes for Lithium ion batteries,” *Journal of Materials Science & Technology,* vol. 30, no. 5, pp. 427 - 433, 2014.

[265] A. Tron, Y.D. Park and J. Mun, “AlF3-coated LiMn2O4 as cathode material for aqueous rechargeable lithium battery with improved cycling stability,” *Journal of Power Sources,* vol. 325, pp. 360 - 364, 2016.

[266] L.I. Jian-gang, H.E. Xiang-Ming and Z. Ru-song, “Electrochemical performance of SrF2-coated LiMn2O4 cathode material for Li-ion batteries,” *Transactions of Nonferrous Metals Society of China,* vol. 17, pp. 1324 -1327, 2007.

[267] S.T. Myung, K. Izumi, S. Komaba, Y.K. Sun, H. Yashiro and N. Kumagai, “Role of alumina coating on Li- Ni- Co- Mn- O particles as positive electrode material for lithium-ion batteries,” *Chemistry of Materials,* vol. 17, no. 14, pp. 3695 - 3704, 2005.

[268] J. Tu, X.B. Zhao, G.S. Cao, D.G. Zhuang, T.J. Zhu and J.P. Tu, “Enhanced cycling stability of LiMn2O4 by surface modification with melting impregnation method,” *Electrochimica Acta,* vol. 51, pp. 6456 - 6462, 2006.

[269] L. Chen, R.E. Warburton, K.S. Chen, J.A. Libera, C. Johnson, Z. Yang, M.C. Hersam, J.P. Greeley and J.W. Elam, “Mechanism for Al2O3 Atomic Layer Deposition on LiMn2O4 from In Situ Measurements and Ab Initio Calculations,” *Chem,* vol. 4, no. 10, pp. 2418 - 2435, 2018.

[270] G.H. Waller, P.D. Brooke, B.H. Rainwater, S.Y. Lai, R. Hu, Y. Ding, F.M. Alamgir, K.H. Sandhage and M.L. Liu, “Structure and surface chemistry of Al2O3 coated LiMn2O4 nanostructured electrodes with improved lifetime,” *Journal of Power Sources,* vol. 306, pp. 162-170, 2016.

[271] S. K. Mishra and G. Ceder, “Structural stability of lithium manganese oxides,” *Physical Review B,* vol. 59, no. 9, pp. 6120 - 6130, 1999.

[272] P. Strobel, G. Rousse, A. Ibarra-Palos and C. Masquelier, “Disproportionation of stoichiometric LiMn2O4 on annealing in oxygen,” *Journal of Solid State Chemistry,* vol. 177, no. 1, pp. 1 - 5, 2004.

Ethylene carbonate adsorption on the major surfaces of lithium manganese oxide $Li_{1-x}Mn_2O_4$ spinel ($0.000 < x < 0.375$)

1. The effect of surface delithiation on the lattice parameter and volume.

Based on the crystal lattice changes that might occur because of surface delithiation when modelling the delthiated phases, we carried out benchmark calculations to check the changes that might occur to the volume due to this defect. The benchmark calculations were carried out through the following steps:

a) Taking both the representative lithiated and delithiated slab model.
b) Unfreeze the bottom two layers and add ISIF=3 to the INCAR.
c) Compare the resulting surface areas.

Table IX: The effect of surface delithiation on the lattice parameter and volume. The calculation was performed by allowing all the atoms to move and setting the ISIF = 3 in the INCAR.

		Lattice parameters						
	Composition	*a*	*b*	*c*	Surface area	%par	%area	
Bulk		8.35	8.35	22.35	69.72			
(001) surface	$Li_7Mn_{16}O_{32}$	8.35	8.35	22.35	69.72	0	0	
		8.35	8.35	22.35	69.72			ISIF=3
	$Li_6Mn_{16}O_{32}$	8.35	8.35	22.35	69.72	2.4	4.9	
		8.15	8.15	12.27	66.40			ISIF=3

The Table IX summarizes the lattice parameters and the surface area for the (001) surface at different Li concentration with respect to the bulk lattice parameters and surface area. We found that the slabs had minor changes with difference of ~0.02 Å, which is equivalent to 3% and an area difference of ~0.05 $Å^3$, which is equivalent to 5%. Indeed, only minor changes in the lattice parameter of the cathode material are expected since a major change in the structure of the cathode would mean loss of possible recharge ability leading to deterioration.

2. Surface delithiation and particle morphologies

For validation, we calculated the surface free energies of the $LiMn_2O_4$ spinel surfaces with the same stoichiometry, and constructed their morphologies for each Li concentration. Figure 17 summarises the effect of delithiation on surface stability and morphologies at different Li concentrations. We observe that upon delithiation the surface energies increase and eventually the (111) becomes the most stable surface. The particle morphologies were also constructed for different Li concentrations using their surface energies. Upon delithiation, we observe that the (001) facet destabilizes and reduce in-plane size, while the (111) surface increase and become the most stable facet.

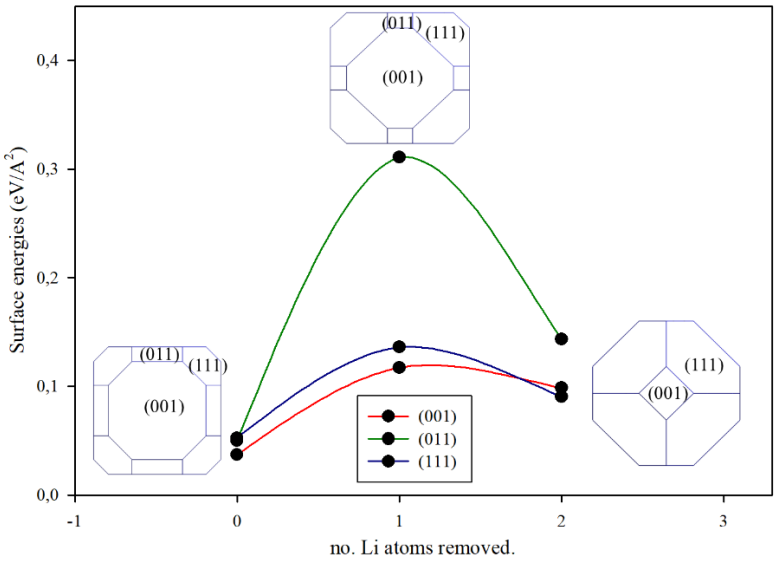

Figure 17: The effect of delithiation on surface stability and morphologies at different Li concentrations.

RESEARCH OUTPUT

PRESENTATIONS

- **Brian Ramogayana,** David Santos-Carballal, Pablo A. Aparicio, Matthew G. Quesne, Khomotso P. Maenetja, Phuti E. Ngoepe and Nora H. de Leeuw, ETHYLENE CARBONATE ADSORPTION ON LITHIUM MANGANESE OXIDE $LiMn_2O_4$ SPINEL SURFACE. Poster presentation. United Kingdom Catalysis Conference, Loughborough, UK, 9 – 11 January 2019.
- **Brian Ramogayana,** David Santos-Carballal, Pablo A. Aparicio, Matthew G. Quesne, Khomotso P. Maenetja, Phuti E. Ngoepe and Nora H. de Leeuw**,** ETHYLENE CARBONATE ADSORPTION ON LITHIUM MANGANESE OXIDE ($LiMn_2O_4$) SPINEL SURFACE.Oral Presentation. ESRC/NRF-funded Newton Project for UK-RSA PhD Exchanges, NWU Sports Village, Potchefstroom, South Africa, 23- 26 April 2019.
- **Brian Ramogayana,** David Santos-Carballal, Khomotso P. Maenetja, Nora H. de Leeuw and Phuti E. Ngoepe. *AB-INITIO* INVESTIGATION OF THE ELECTRONIC PROPERTIES OF LOW MILLER INDEX SURFACES IN $LiMn_2O_4$ SPINEL. Oral presentation. South African Institute of Physics (SAIP) Conference, Protea hotel Ranch Resort, Polokwane, South Africa, 8 – 12 July 2019.
- **Brian Ramogayana,** Khomotso P. Maenetja and Phuti E. Ngoepe**.** COMPUTATIONAL INVESTIGATION OF STRUCTURAL, ELECTRONIC, AND MECHANICAL PROPERTIES OF SPINEL $LiMn_2O_4$**.** Poster presentation. South African Institute of Physics (SAIP) Conference, Protea hotel Ranch Resort, Polokwane, South Africa, 8 – 12 July 2019.

PUBLICATIONS

- **Brian Ramogayana,** David Santos-Carballal, Pablo A. Aparicio, Matthew G. Quesne, Khomotso P. Maenetja, Phuti E. Ngoepe and Nora H. de Leeuw, ETHYLENE CARBONATE ADSORPTION ON THE MAJOR SURFACES OF LITHIUM MANGANESE OXIDE $Li_{1-x}Mn_2O_4$ SPINEL ($0.000 < x < 0.375$). Published

in the journal of physical chemistry chemical physics (PCCP). ***Phys. Chem. Chem. Phys.,*** 2020, **22**, 6763 – 6771. **https://doi.org/10.1039/C9CP05658K** (Appendix 1).

- **Brian Ramogayana,** David Santos-Carballal, Khomotso P. Maenetja, Nora H. de Leeuw and Phuti E. Ngoepe. *AB-INITIO* INVESTIGATION OF THE ELECTRONIC PROPERTIES OF LOW MILLER INDEX SURFACES IN $LiMn_2O_4$ SPINEL. Submitted as a review article for SAIP proceeding publication (Appendix 2).

PCCP

ROYAL SOCIETY OF CHEMISTRY

PAPER

View Article Online
View Journal | View Issue

Cite this: Phys. Chem. Chem. Phys., 2020, 22, 6763

Ethylene carbonate adsorption on the major surfaces of lithium manganese oxide $Li_{1-x}Mn_2O_4$ spinel ($0.000 < x < 0.375$): a DFT+U-D3 study†

Brian Ramogayana, [a] David Santos-Carballal, ‡*[ab] Pablo A. Aparicio, [b] Matthew G. Quesne, [b] Khomotso P. Maenetja, [a] Phuti E. Ngoepe [a] and Nora H. de Leeuw ‡*[b,c]

Understanding the surface reactivity of the commercial cathode material $LiMn_2O_4$ towards the electrolyte is important to improve the cycling performance of secondary lithium-ion batteries and to prevent manganese dissolution. In this work, we have employed spin-polarized density functional theory calculations with on-site Coulomb interactions and long-range dispersion corrections [DFT+U-D3-(BJ)] to investigate the adsorption of the electrolyte component ethylene carbonate (EC) onto the (001), (011) and (111) surfaces of the fully lithiated and partially delithiated $Li_{1-x}Mn_2O_4$ spinel ($0.000 < x < 0.375$). The surface interactions were investigated by evaluating the adsorption energies of the EC molecule and the surface free energies. Furthermore, we analyzed the impact of EC adsorption on the Wulff crystal morphologies, the molecular vibrational frequencies and the adsorbate/surface charge transfers. The adsorption energies indicate that the EC molecule strongly adsorbs on the (111) facet, which is attributed to a bidentate binding configuration. We found that EC adsorption enhances the stability of the (111) facet, as shown by the Wulff crystal morphologies. Although a negligible charge transfer was calculated between the spinel surfaces and the EC molecule, a large charge rearrangement takes place within the surfactant upon adsorption. The wavenumbers of the C=O stretching mode for the interacting EC molecule are red-shifted with respect to the isolated adsorbate, suggesting that this bond becomes weaker. The surface free energies show that both the fully lithiated and partially delithiated forms of the $LiMn_2O_4$ surfaces are stabilized by the EC molecule.

Received 17th October 2019,
Accepted 16th February 2020

DOI: 10.1039/c9cp05658k

rsc.li/pccp

1. Introduction

Over the last few decades, renewable energy storage has become of significant interest in the development of electric vehicles, which could facilitate a lesser reliance on fossil fuels and thus a lower impact on global warming. Although many studies have aimed at discovering or developing sustainable, earth-abundant and/or low-cost alternative materials,[1–3] there is still no viable replacement for the current lithium-based batteries. However, the development of more efficient and stable cathode materials would offer a major step forwards in the performance of lithium-ion batteries. Various cathode materials have been studied, including $LiCoO_2$,[4,5] $Li_3V_2(PO_4)_3$,[6] $LiMn_2O_4$,[7,8] $Li_4Mn_5O_{12}$,[9] $LiFePO_4$[10] and NMCs[11] in order to improve the electrochemical performance of lithium-ion batteries.

Among these materials, lithium manganese oxide ($LiMn_2O_4$) spinel has attracted the most attention as a potential cathode material because of its three-dimensional crystal structure that allows a reversible diffusion of Li^+ ions.[12,13] Moreover, $LiMn_2O_4$ is considered a safer substitute for the currently commercialized $LiCoO_2$ owing to its low environmental impact, the abundance of manganese and its high energy density.[14] However, the use of $LiMn_2O_4$ spinel as a cathode material is limited by the irreversible fading of the capacity, which is attributed to the dissolution of manganese, electrolyte oxidation at high voltages, and the Jahn–Teller distortion of the octahedral Mn^{3+} atoms.[15,16]

A number of methods have been attempted to mitigate the manganese dissolution, including (i) cation doping,[17,18] (ii) the replacement of the commercially used $LiPF_6$ as the electrolyte ionic conductor to limit the production of the scavenging hydrofluoric acid produced by its degradation,[19–21] and (iii) surface coating to create an artificial barrier that limits the direct electrode–electrolyte contact.[22–25] However, there is currently no substitute ionic conductor for the electrolyte that has better

[a] Materials Modelling Centre, School of Physical and Mineral Sciences, University of Limpopo, Private Bag x1106, Sovenga 0727, South Africa
[b] School of Chemistry, Cardiff University, Main Building, Park Place, Cardiff CF10 3AT, UK. E-mail: D.Santos-Carballal@leeds.ac.uk, N.H.deLeeuw@leeds.ac.uk
[c] Department of Earth Sciences, Utrecht University, Budapestlaan 4, 3584 CD Utrecht, The Netherlands

† Electronic supplementary information (ESI) available. See DOI: 10.1039/c9cp05658k

‡ Present address: School of Chemistry, University of Leeds, Leeds LS2 9JT, UK.

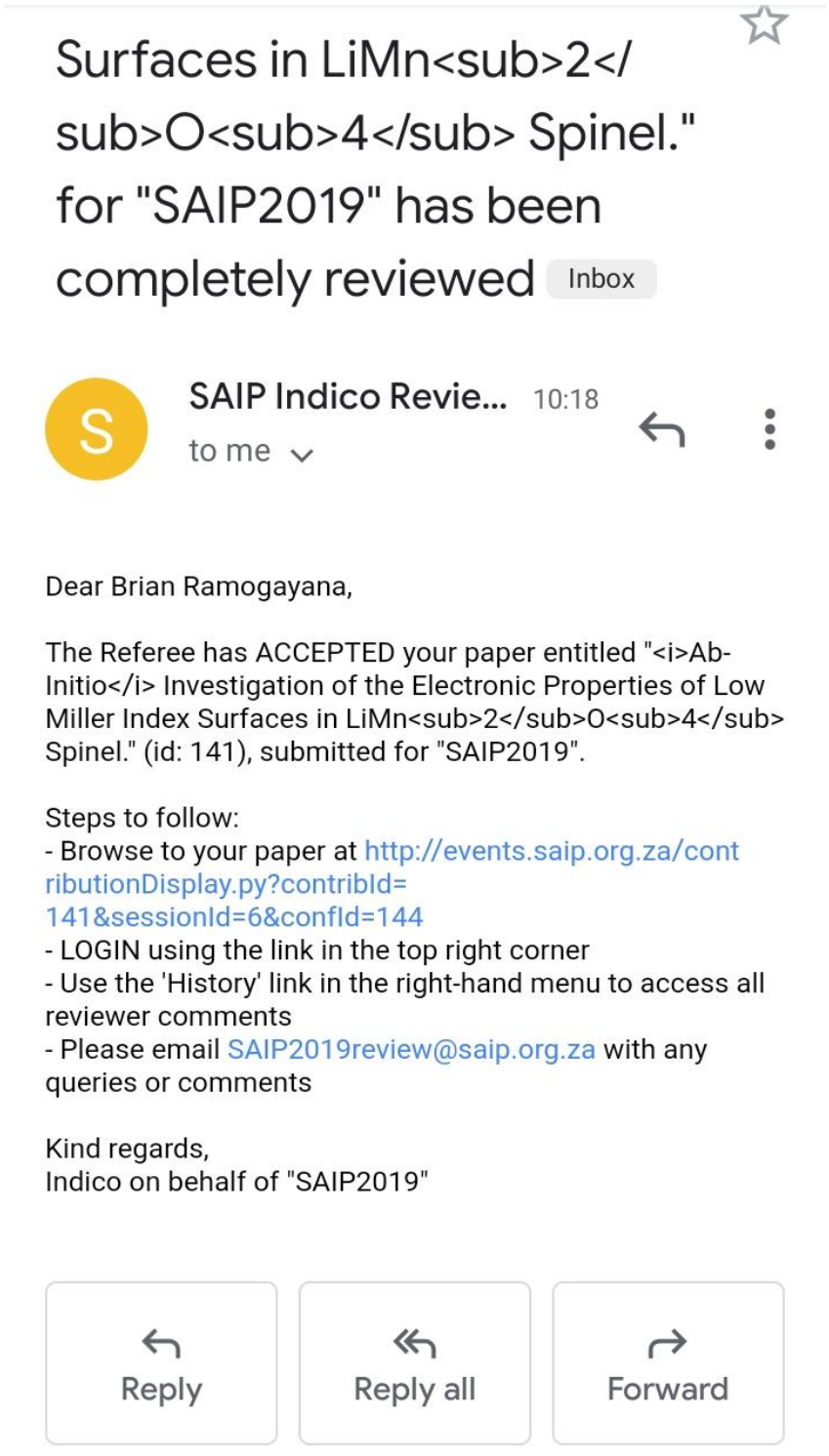

Surfaces in LiMn₂O₄ Spinel." for "SAIP2019" has been completely reviewed Inbox

SAIP Indico Revie... 10:18
to me

Dear Brian Ramogayana,

The Referee has ACCEPTED your paper entitled "Ab-Initio Investigation of the Electronic Properties of Low Miller Index Surfaces in LiMn₂O₄ Spinel." (id: 141), submitted for "SAIP2019".

Steps to follow:
- Browse to your paper at http://events.saip.org.za/contributionDisplay.py?contribId=141&sessionId=6&confId=144
- LOGIN using the link in the top right corner
- Use the 'History' link in the right-hand menu to access all reviewer comments
- Please email SAIP2019review@saip.org.za with any queries or comments

Kind regards,
Indico on behalf of "SAIP2019"

Reply Reply all Forward